Zero Waste Approaches for Cost-Effective Treatment of Industrial Waste 2021

Lead Guest Editor: Erol Yilmaz
Guest Editors: Shuai Cao and Babak Koohestani

Zero Waste Approaches for Cost-Effective Treatment of Industrial Waste 2021

Zero Waste Approaches for Cost-Effective Treatment of Industrial Waste 2021

Lead Guest Editor: Erol Yilmaz
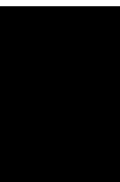Guest Editors: Shuai Cao and Babak Koohestani

Contents

Research Article

Recycling Dam Tailings as Cemented Mine Backfill: Mechanical and Geotechnical Properties

Tugrul Kasap [iD],[1,2] **Erol Yilmaz** [iD],[1,3] **Nihat Utku Guner** [iD],[1,2] **and Muhammet Sari** [iD][1,2,3]

[1]*Geotechnical, Waste Management and Backfill Laboratory, Recep Tayyip Erdogan University, Fener, Rize TR53100, Turkey*
[2]*Institute of Graduate Studies, Recep Tayyip Erdogan University, Fener, Rize TR53100, Turkey*
[3]*Department of Civil Engineering, Geotechnical Division, Recep Tayyip Erdogan University, Fener, Rize TR53100, Turkey*

Correspondence should be addressed to Erol Yilmaz; erol.yilmaz@erdogan.edu.tr

As a result of developing technology and scientific studies, employing dam tailings as critical raw material and vital economic reserve has become widespread recently. Employing dam tailings as a main ingredient of CPB (cemented paste backfill) can offer benefits to mining operations. This study deals with the use of dam tailings in CPB, considering the mechanical and geotechnical aspects. CPB was prepared at fixed solid and cement contents (72%, and 5%, respectively) and tested for different cure ages varying from 3 to 56 days. The results disclosed that the strength of filling increased over time, with the exception of 56-day cured CPB having high sulfur minerals where strength decreased sharply. The reasons behind these strength surges could be clarified by CPB's basicity, which quickens the hydration of cement. Voids between tailings grains are also occupied by hydration products, resulting in the high strengths. Due to the fact that higher sulfate contents can cause lower pH values within CPB, this is one of the factors that should be considered for the backfill's strength performance. The cement tends to increase the backfill's pH in short term, but pH of long-term cured backfills decreases because of dam tailings which is inclined to acid formations and erosions. This is a sign that the deformation properties of CPB are deteriorated. Depending on curing time, CPB's water content and void ratio decrease, but their surface areas increase. The resulting data will endow to better apprehend the effects of dam tailings on CPB quality integrating cost and quality.

1. Introduction

The major amounts of tailings are inevitably created on account of the processing of valuable minerals in the mining sector [1, 2]. They are mostly cumulated in surface tailings impoundments/dams and refilled into underground stopes where the ore is extracted [3, 4]. In particular, pyritic tailings stored on surface occupy and possibly contaminate large fertile lands or soils and surface-ground water, creating the development of acid mine drainage in prevalence of H_2O and O_2 [5, 6]. These risks continue during and after the mining operation by posing a serious threat to the environment [7, 8]. Although these problematic tailings are seen as economically worthless, nowadays they are used as raw material, such as in geopolymer [9], mine backfill [10], ceramics manufacture [11], and brick production [12] and to

reestablish plant fertility in polluted soils [13]. Valorization of the tailings appears to be not only a source of invaluable raw materials but also a capable substitute to cut their ecological impacts [14, 15]. In recent years, the effective reuse of the tailings produced after active mining operations in different sectors such as construction and civil engineering causes a major reduction in the amount of the generated tailings which need to be treated properly [16, 17]. However, the continuous storage of tailings into the dams might create capacity problems and hence pose a serious risk such as failure and leakage [18, 19].

In addition, when compared to low-grade ores, the tailings received from dams can contain many valuable elements and present a remarkable commercial value [20, 21]. Taking into account the elements in tailings accumulated in the dams, they can be used either for backfill

(acidified tailings) or for raw materials (nondamaged tailings) [22]. Nevertheless, the current study will consider acidified dam tailings for mine fill applications, especially for cemented paste backfill (CPB), while the nondamaged dam tailings are out of the scope of this study. Being an innovative tailings disposal system, CPB allows mine operators to send 65–80% of pyritic tailings back to underground stopes as backfill (it helps to build for ground support) or disposal purposes [23, 24]. Unlike concrete materials, CPB has unique properties such as finer (at least 15% under $20 \mu m$) grain size, higher (typically more than 5) water/cement ratio, and lower (typically less than 10%) cement content [25, 26]. As a result of these characteristics, CPB increases the neutralization potential of pyritic tailings and ensures secure storage in an alkaline environment with low permeability [27]. Consequently, CPB has been frequently preferred in the mining industry targeting both sustainable development and circular economy [28, 29].

Numerous researchers have so far focused on CPB's key components such as physical [30], chemical [31], rheological [32], and mechanical properties [33]. However, the mining-induced environmental problems have led rethinking mine operators to reduce or eliminate the presence of pyritic tailings accumulated in the dams [34–37]. Aldhafeeri and Fall [38] experimentally investigated the effect of cemented paste tailings (CPT) on the reactivity of the initial sulfate content by conducting O2 consumption tests on backfill samples and observed that CPT's reactivity augmented with growing sulfate concentration. Dong et al. [7] explored sulfate effect on CPB's long-term stability and found that high amounts of sulfur minerals like pyrite caused severe erosion between 90 and 360 days of curing times, decreasing the backfill strength by 11–32%. Li et al. [39] evaluated the short-term strength of CPB with variable sulfur content (6–25wt.%) and found that a significant loss of strength (~21%) occurred in 14-day cured samples. Liu et al. [40] examined the influence of sulfur content on CPB's strength characteristics and stated that sulfur content plays a vital role in these properties of backfilling. Zheng et al. [41] explored experimentally the potential of employing slag activated with reactive MgO as a binding agent within the backfill with sulfidic tailings and found that pH values (11.5) increased before 14 days by reason of acid/sulfate attacks while they decreased to 9.8–10.5 after 14 days (from 28 to 360 days).

The above-mentioned literature has mainly focused on short- and long-term effects of pyritic tailings generated from ore processing plant. However, the impact and potential use of already-deposited dam tailings which can have different pH values have not been totally investigated yet. In this study, the effect of dam tailings with different pH values (4.2, 5.9, 6.8, and 10.5–control sample) on quality and performance of CPB was investigated experimentally. Three tailings samples (pH: 4.2, 5.9, and 6.8) are collected from the different regions of a selected tailings dam site, while one tailings sample (pH: 10.5) is received from the filter of a flotation based ore processing plant. Mine fill specimens were manufactured by employing a fixed binder dosage of 5wt.% and solid content of 72wt.% and later exposed to several mechanical (e.g., uniaxial compressive strength,

stress-strain behavior, and elastic modulus) and geotechnical (e.g., water content, porosity, specific surface area, and degree of saturation) characteristics of mine fill specimens. In addition, how diverse pH tailings affect the overall performance and behavior of mine fills was thoroughly discussed in the current paper.

2. Materials and Methods

2.1. Properties of Ingredients

2.1.1. Tailings. Pyritic tailings experimented in this work were supplied from an active underground copper mine. Two types of concentrate are produced in the concentrator facility of the tested mine: Copper concentrate with 17–18wt.% Cu content and pyrite concentrate with 47–48% S content. In addition to these concentrates, the mine also generates processing tailings which are noneconomical and managed sustainably in different places. Nearly 80% of the generated tailings are deposited into tailings dams, while the rest (20wt.%) are used as cemented paste backfill (CPB). The primary target of the current work is to recycle dam tailings as CPB. Accordingly, three samples were collected from different points of the tailings dam (DTS1, DTS2, and DTS3), while one sample was collected from the filter (PTS, it will be also evaluated as control sample). The dam tailings were sampled from a close distance of 3 to 5 m and a depth of 15–25 cm with the help of auger and shovel-up. The sample collection points are clearly shown in Figure 1.

Physical characteristics of four tailings samples are listed in Table 1. Specific gravity (G_s) of tailings differs from 3.57 to 3.81, while their specific surface areas (S_s) vary in the range of 2.68–2.89 m^2/g. The highest maximum dry density value (2.55 kg/m^3) and moisture content value (13.4%) were obtained from DTS1 sample. Tailings' chemistry was also detected using PANalytical Epsilon 5 energy dispersion XRF (X-ray fluorescence) spectrometry, and the achieved outcomes are presented in Table 2. According to the oxide analysis results, it was determined that Fe_2O_3 was the most dominant compound, varying from 33.45% to 43.06%.

2.1.2. Binder and Mixing Water. Ordinary Portland cement (OPC) type I 42.5R was employed as a principal binder within diverse CPB mixtures. The G_S and S_S values of OPC were found as 3.11 and 0.39 m^2/g, respectively. The contents of CaO and SiO_2, which are OPC's main components, were found to be 63.76% and 17.76%, respectively. Only tap water was used in CPB mixtures. It is kept in mind that the influence of mixing water on CPB's chemistry was not definitely aimed at in the current work.

2.2. Experimental System

2.2.1. Backfill Manufacturing. A total of 36 CPB specimens were smoothly manufactured in the geotechnical, waste management, and backfill laboratory (Table 3). Since the goal of this work is to experimentally measure the influence of mechanical and geotechnical parameters on backfill's
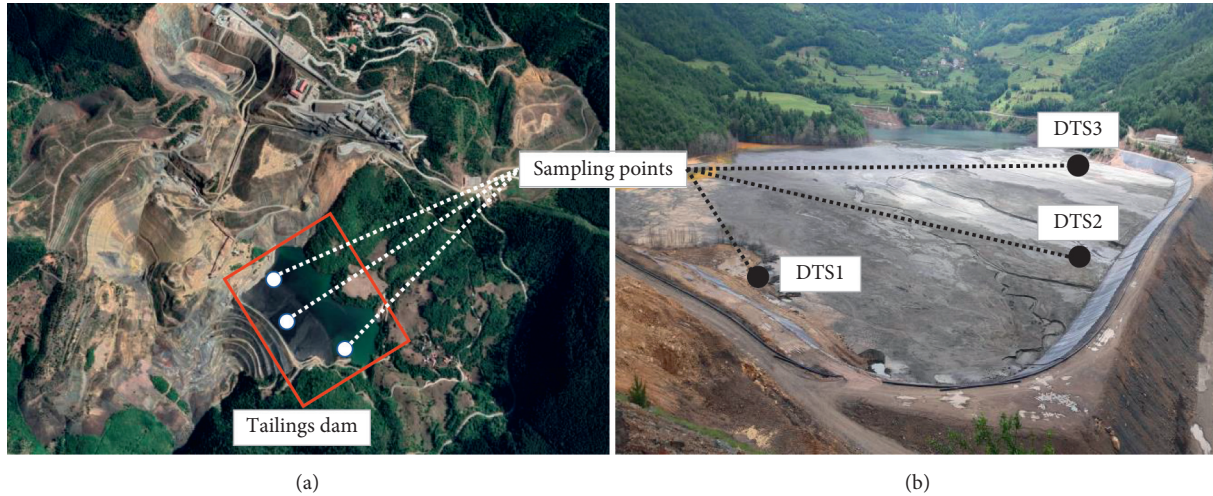
FIGURE 1: The sample collection points in the tailings dam: (a) satellite view and (b) dam view.

TABLE 1: Tailings' physical properties.

Samples	Specific gravity (GS)	Specific surface area (SS, m^2/g)	Maximum dry density (kg/m^3)	Optimum moisture content (%)
DTS1	3.81	2.89	2.55	13.4
DTS2	3.75	2.83	2.49	12.9
DTS3	3.67	2.77	2.42	12.4
PTS	3.57	2.68	2.37	12.3

TABLE 2: Tailings' chemical properties (oxide analyses).

Composition	DTS1 (%)	DTS2 (%)	DTS3 (%)	PTS (%)
Fe_2O_3	33.45	37.11	40.75	43.06
Mn_3O_4	0.13	0.14	0.13	0.07
BaO	0.01	0.01	0.01	0.01
TiO_2	0.20	0.19	0.25	0.31
CaO	4.81	4.01	3.99	2.60
K_2O	0.45	0.44	0.32	0.26
SO_3	0.38	0.33	0.34	0.34
P_2O_5	0.09	0.07	0.07	0.05
SrO	0.01	0.01	0.01	0.01
SiO_2	34.31	30.11	25.44	23.16
Al_2O_3	6.13	6.99	7.07	7.78
MgO	1.66	1.88	1.82	2.46
Na_2O	0.06	0.05	0.06	0.11
LOI	18.32	20.11	20.17	20.23

TABLE 3: Different mixture recipes of CPB materials manufactured with dam tailings.

CPB-ID	Tailings type	Binder content (%)	Solid content (wt. %)	Pyrite/sulfide content (%)	pH value	Slump (cm)	Curing time (days)
CPB-D1	DTS1	5	72	46/34	4.2	25	3, 14, 28, 56
CPB-D2	DTS2	5	72	39/25	5.9	25	3, 14, 28, 56
CPB-D3	DTS3	5	72	35/21	6.8	25	3, 14, 28, 56
CPB-P	PTS	5	72	32/16	10.5	25	3, 14, 28, 56

quality and behavior, solid (72wt.%) and cement (5wt.%) contents of CPB samples were kept constant. Firstly, the blending ratios were determined for each CPB sample, and samples were thoroughly mixed for 7–10 minutes with the help of the UTEST lab mixer until the mixture got homogeneous. To remove air within the backfill, a steel rod stick was used by tamping 25 times. The prepared backfill materials were cast in a cylindrical plastic mold ($D \times H$:

50×100 mm) in one-third length increments. The casting backfill molds were then closed by using plastic covers to prevent air and water from evaporating and oxidizing in the course of curing time. Finally, backfills were put in the cure room until target curing of 3, 14, 28, and 56 days. The curing box was adjusted to be at $20 \pm 3°$C temperature and $90 \pm 5\%$ humidity. Figure 2 shows some stages of the backfill sample preparation. Three CPB backfills were manufactured for a given mine backfill recipe and their mean value was considered as a main result in this paper.

2.2.2. Determination of Mechanical Parameters. The backfill's mechanical parameters (e.g., uniaxial compressive strength (UCS), stress-strain behavior, and elastic modulus E50) were experimentally investigated. A servo controlled UTEST Multiplex machine having 50 kN nominal capacity and 1 mm/min replacement rate was used for characterizing the backfill's mechanical parameters. Once CPB samples reached the target curing time, they were removed from the plastic molds placed within cure box and sample dimensions were measured by caliper and assay balance. The upper/lower sections of hardened fill samples to be placed between the platens were smoothed by a sharp instrument (cutter). The UCS tests of cylindrical backfill samples prepared in $D \times H$: 5×10 cm (a length/diameter ratio of 2) were performed by following the ASTM C39 standard.

2.2.3. Determination of Geotechnical Parameters. After mechanical testing, CPB's specific surface area S_s, specific gravity G_s, water content w, void ratio e, and saturation degree S_r parameters were measured by using different methods. The BET technique (using a Micromeritics Gemini 2375 volumetric analyzer) was employed to determine samples' S_s values. To measure the backfill's w values, sample pieces were oven-dried at nearly $50°$C for 2 days. The G_s value was explored with the aid of the Micromeritics AccuPyc 1330 helium pycnometer. CPB's pore structures were detected by employing a Micromeritics Autopore III 9420 Hg intrusion porosimeter. Accordingly, void ratio e was calculated by using equation (1). The degree of saturation S_r parameter was also estimated by employing already-known parameters w, G_s, and e (see equation (2));

$$e = \frac{n}{1-n}. \quad (1)$$

$$S_r = \frac{wG_s}{e}, \quad (2)$$

where G_s is the specific gravity; n is the porosity (%); e is the void ratio; w is the water content (wt. %); and S_r is saturation degree (%).

3. Results and Discussion

3.1. Influence of Dam Tailings on Mine Backfill Strength. Figure 3 displays the strength development of mine backfills being cured after 3, 14, 28, and 56 days. UCS values of all backfill samples (CPB-D1, CPB-D2, CPB-D3, and CPB-P)

increased during the first 28 days of curing. However, at 56-day curing time, a 3.9% decrease in the strength acquisition of CPB-D1 (compared to 28-day curing time) was observed. The 56-day cured backfills (CPB-D3, CPB-P, and CPB-D2) provided, respectively, 19.4%, 11.1%, and 4.9% higher strengths than the 28-day cured ones. CPB-P had the highest strength (0.582 MPa), while CPB-D1 had the lowest strength (0.221 MPa). CPB-D1 produced 55.0%, 60.1%, 56.1%, and 62.0% lower strengths than control sample (CPB-P) for curing times of 3, 14, 28, and 56 days, respectively. These values were 42.9%, 47.5%, 40.0%, and 43.3% for CPB-D2 and 18.9%, 27.0%, 19.7%, and 13.8% for CPB-D3, respectively. The key reason behind the strength changes in different CPB samples as a function of pH can be explained by cement hydration. At early curing ages (3–28 days), calcium oxide (CaO) being produced because of cement hydration increased due to the alkalinity of the medium. This led to an increase in alkalinity which caused increasing the strength of CPB samples.

In the long term (56 days), the decrease in pH values and the gradual increase in sulfate content slowed down the rate of cement hydration and decreased the alkalinity of the internal system by producing acid. The strength of CPB-P, CPB-D3, and CPB-D2 samples which reached high pH values was not affected greatly although pH of the medium decreased. However, the strength of 56-day cured CPB-D1 decreased mainly due to the pH value below 7, which indicates an acidic environment. In addition, the decrease in ambient alkalinity during long curing times caused slight erosions on samples. The decrease in the pH value of CPB not only created an unfavorable environment for cement hydration but also caused the deterioration of other backfills. The acidic property of tailings is a parameter that directly affects the strength of CPB. This issue was well discussed in every single aspect in the literature works [7, 39].

3.2. Influence of Dam Tailings on CPB's Stress-Strain Curves. Figure 4 displays the stress-strain relationship of 28- and 56-day cured CPB samples. Stress-strain curves can be assessed in four stages (i.e., pore compaction, elastic deformation, plastic flow, and rupture-fracture). Samples at the pore compaction stage had many voids due to the loose nature of tailings. After the first load is applied, the microcavities of CPB samples began to close and a bowl-shaped stress-strain curve formed. At second stage, as compressive stress increases, strain increases equivalently and CPB samples arrived at the stage of elastic deformation. Thus, the stress-strain curve goes to a straight line and the microcracks form within CPB. At the next stage (plastic flow stage), elastic deformation turned into plastic one. Then the internal cavities and cracks of CPB gradually expanded and the curve reached the maximum (peak) strengths. The highest strengths and slopes of the curve were observed in CPB-P samples, while the smallest ones were observed in CPB-D1. As the compressive stress continued to be applied, the stress gradually decreased and all CPB samples had certain residual strengths after failure. It was found that the CPB-P and CPB-D3 samples showed high brittleness after stress reached the
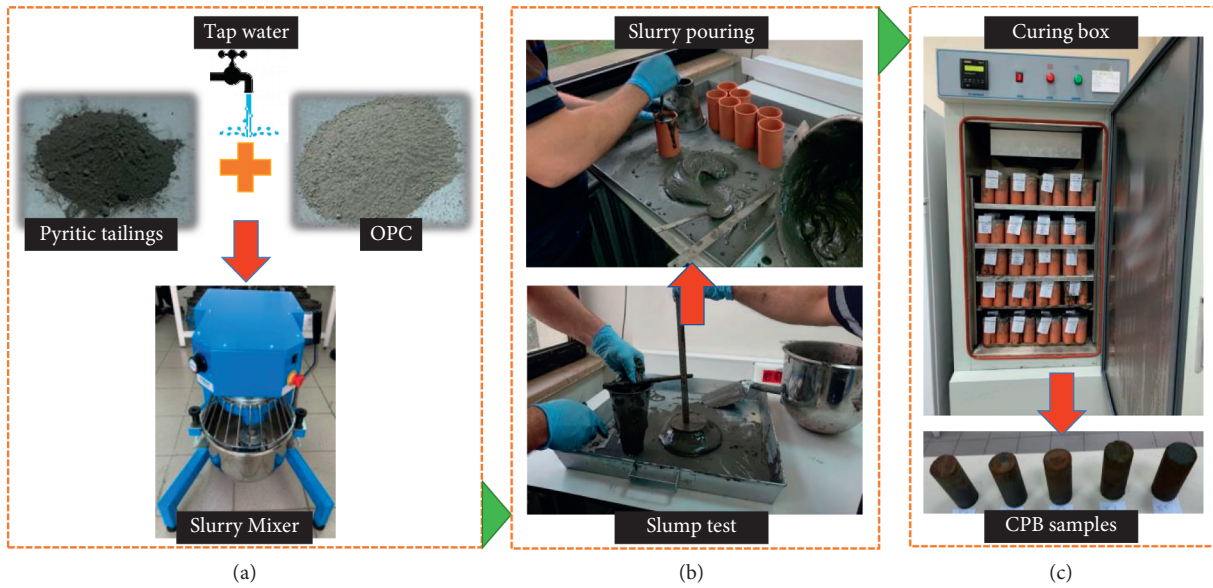
FIGURE 2: Manufacturing stages of backfill mixtures: (a) blending, (b) slump measurements, and (c) curing.
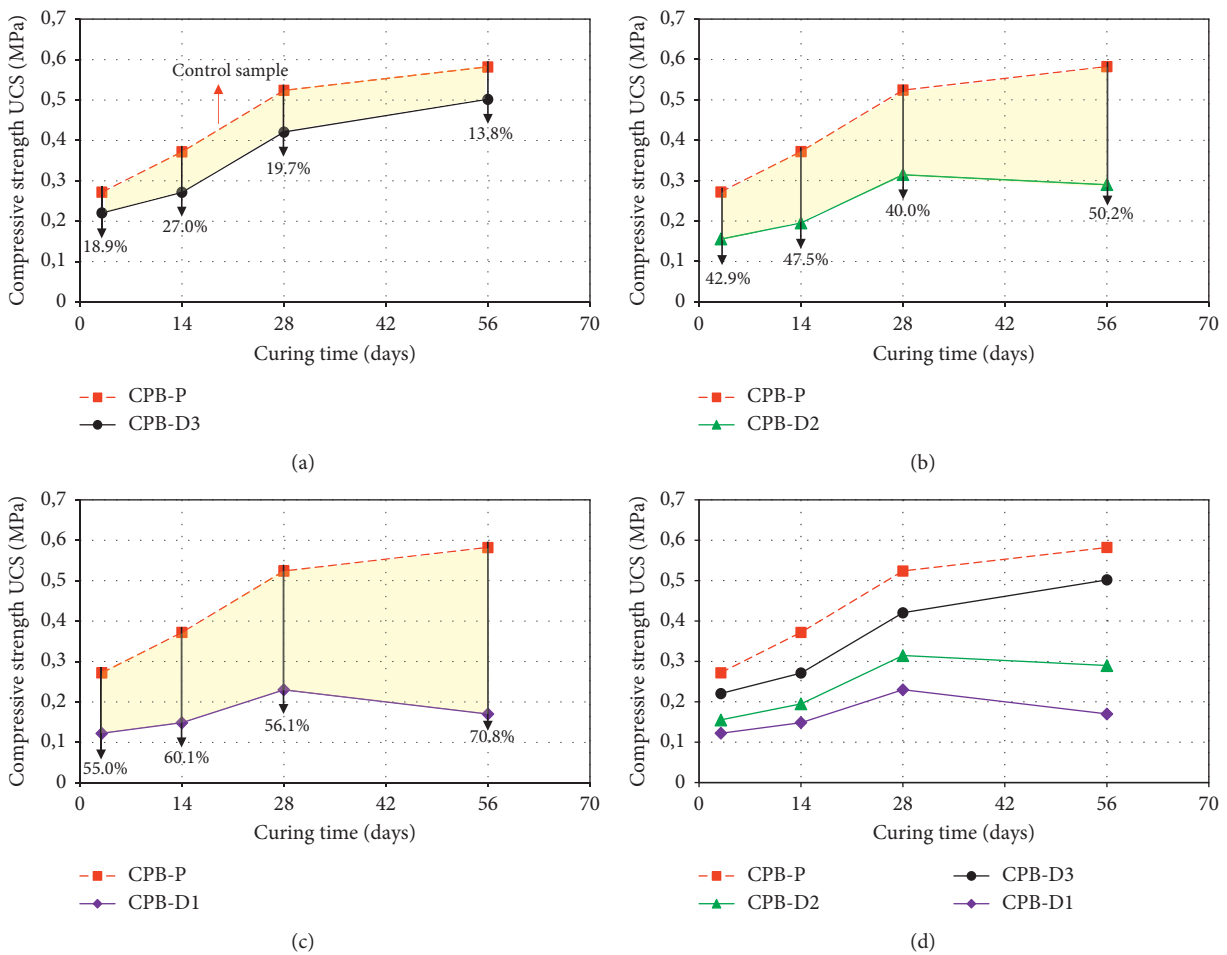
FIGURE 3: Change in UCS with time for diverse mine backfills.

peak values. However, CPB-D1 and CPB-D2 samples had larger strain values compared to other samples. Since the pH values of these samples are very low, an acidic medium (causing lower pH values) formed and CPB indicated ductile behavior. Similar stress-strain behavior was observed in the literature [32, 42]. One can also observe from Figure 4 that
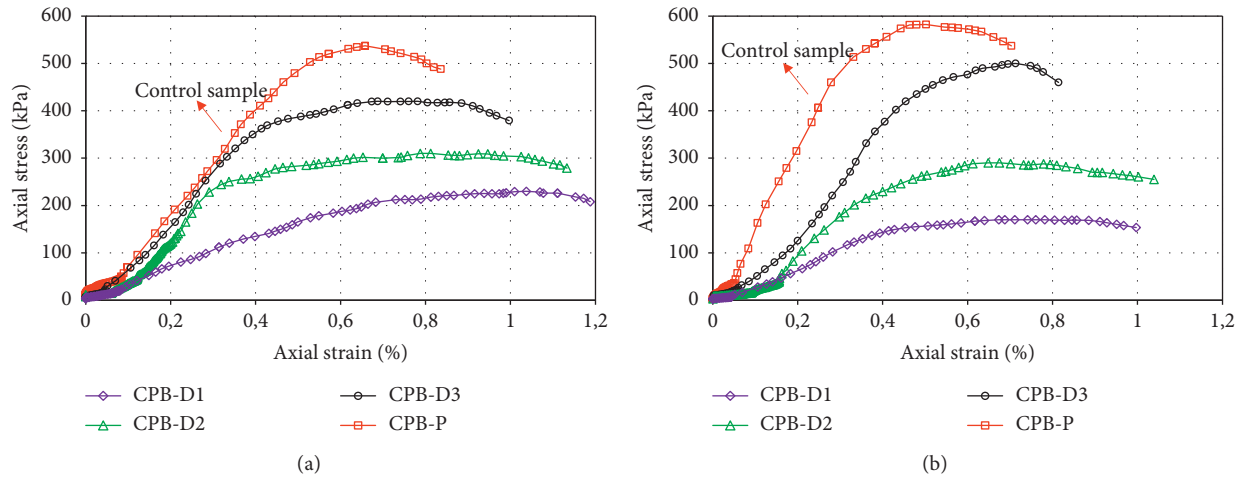
Figure 4: Change in axial stress with axial strain for diverse mine backfills: (a) 28 days and (b) 56 days.

56-day cured backfills had higher peak and residual strengths in comparison with 28-day cured ones.

3.3. Influence of Dam Tailings on CPB's Elastic Modulus.
Elastic modulus is a vital factor to better clarify the resistance of mine backfills to elastic deformation. While it reflects the compressive capacity of mine backfills, it is attentively connected to bearing capacity in upper layers of the backfills placed in subsurface voids. Three methods, tangent modulus (E_{max}), secant modulus (E_s), and mean modulus (E50), are mostly used to determine the elastic modulus values according to the ASTM D3148 standard. The E50 value which is equivalent to 50% of the failure stress is used to determine the service condition of geotechnical structures like CPB during their service life [43]. In this study, the E50 values obtained from stress-strain curves, based on UCS testing, were used. Figure 5 shows the relationship between E50 and cure time for diverse mine backfills. Overall, elastic modulus of CPB samples varies between 10 and 20 MPa at early ages and between 100 and 1200 MPa at later ages [42, 44]. The E50 values obtained for all backfill samples range from 14 to 115 MPa, which shows that the values found are in agreement with earlier studies.

E50 values of all mine backfills increase over time as a consequence of chemical reactions that take place inside CPB. The increase in the backfill's density due to the hydration products (C-S-H gels) which fill CPB's pores can trigger creating a harder material with a higher elastic modulus [45]. This is the reason why the control sample CPB-P in particular exhibits high E50 values. In comparison, the samples CPB-D1, CPB-D2, and CPB-D3 (acidic samples) prepared with dam tailings have lower E50 values by 22.1% to 78.7%. The main reason for this significant decrease is related to the corrosion effect that occurs in CPB samples after 28 days. The corrosion effect (lowering of the pH in CPB) in the backfill pointedly affects the resistance of backfilling to elastic deformation [46]. Moreover, this situation promotes the formation of corrosive ions in CPB, which prevents the reactions between hydrated gels and

affects CPB's rigidity. In addition, a large amount of expansion crystals is expected to form in CPB with low pH values (high sulfate concentration) after 56 days, causing the formation of cracks in mine backfills and thus a drop in the elastic modulus. As mentioned earlier, the long-term deterioration of the structural integrity of CPB prepared with dam tailings is directly related to acidity. Acidic tailings directly lead to sulfate attack and corrosion formation, which prevents CPB's pore structure and the cement's hydration formation. As a result, developing elastic modulus is directly influenced by acidic dam tailings.

3.4. Geotechnical Parameters

3.4.1. Assessment of Water Content.
Index properties like water content w (%), specific surface area S_s (m^2/g), saturation degree S_r (%), and void ratio e strongly govern CPB's stability. In cementitious materials like CPB, cement and water content directly affect the curing time [47]. Figure 6 displays the disparity in CPB's water content over time. Although the water content of all cured samples varies between 7% and 20.5%, the water content decreases with increasing cure time. The lowest water content (7%) was observed in reference sample (CPB-P), while the highest water content (20.5%) was observed in CPB-D1 sample. However, the water content of 56-day cured samples lessened in the range of 20.3–52.4% in comparison with 3-day curing time. The water contents of 56-day cured CPB-D1 and CPB-D2 samples only showed an increase (4.95% and 2.13%, respectively) when compared to 28 days. In general, the decrease in the water content increased CPB's performance. Basically, the free water required for CPB's cement hydration governs the amount of final water [48].

The water used within the mixture has two main functions on CPB, such as workability and initiating the hydration process. However, the drainage of CPB pore waters over time causes a serious decrease in total void ratio, increasing the strength [49]. In addition, the drainage of pore water contributes to the hydration process [50]. This leads to CPB with

(a)

(b)

(c)

(d)
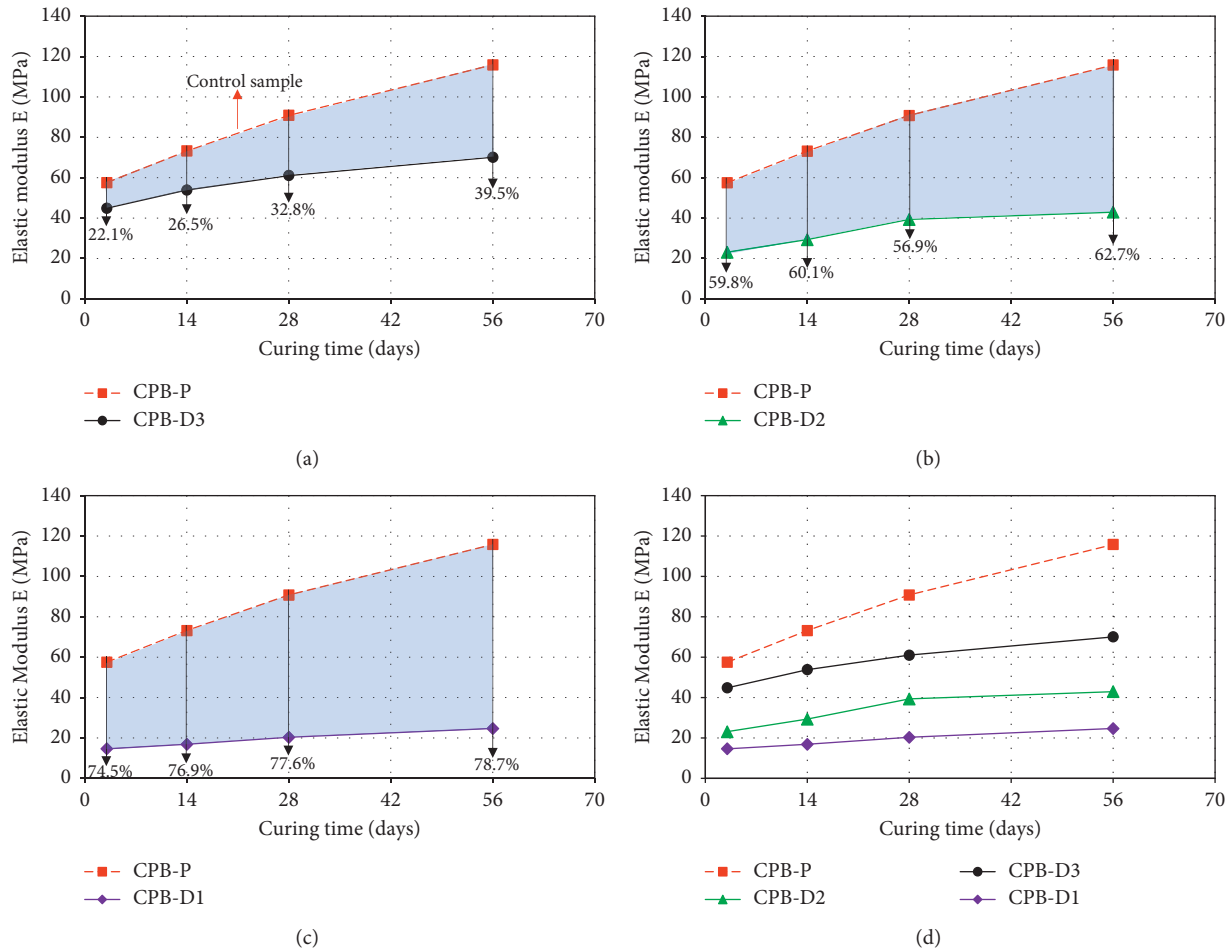
FIGURE 5: Change in elastic modulus with time for diverse mine backfills.

pores formed as a result of hydration (contributed to the hardening process in CPB samples) [51]. The main reason for the increase in water content in CPB-D1 and CPB-D2 samples during the 56-day curing period can be explained by the low ambient pH compared to other samples [49]. The decrease in pH provides acidic properties and stops the chemical reactions in CPB. This causes excess water to remain in sample. Therefore, excess water that does not participate in hydration can be considered as a reason for the strength reduction of CPB.

3.4.2. Assessment of Void Ratio. Figure 7 indicates that void ratio (*e*) of CPB samples significantly decreased over the entire curing time. Note that void ratios of all backfill samples differ from 0.49 to 0.87. However, the void ratios of 56-day cured samples decreased between 2.30% and 25.8% when compared to 3-day curing time. The lowest void ratio (0.49) was observed in the reference sample (CPB-P), while the highest void ratio (0.87) was observed in the CPB-D1 sample. The curing time is closely related to CPB's total void ratio. The drop in *e* value causes the water drainage and a sharp rise in the fill's density. This causes the continued hydration process to generate bigger quantities of hydration product that fills the spaces between particles,

thus significantly reducing the void ratio [52]. This is not the case for CPB-D1 and CPB-D2 samples, although the void ratios were noticeably reduced in all samples. In general, when compared to 3 days, the void ratio in 56-day cured CPB-D3 and CPB-P samples decreased by 20.3% and 25.8%, respectively, while these values were reduced by 2.30% and 5.88% for CPB-D1 and CPB-D2 samples, respectively.

Void ratio is greatly increased by evaporation of excess chemically unreacted water (low pH samples) [53]. As the curing times of CPB-D1 and CPB-D2 samples increase, the decrease in ambient pH causes an increase in the void ratio by preventing the chemical reaction (hydration) that fills the voids of the mixture [54]. In addition, void ratio is closely related to the grain size. When fine grains are undue (the grain size of acidic samples is small), coarse grains will be repelled by fine grains, significantly increasing the sum of water requested for filling the spaces between the particles. On account of this situation, the absence of sufficient water for hydration or the presence of acidic water will increase the void ratio in CPB [55, 56]. The 56-day cured CPB-D1 and CPB-D2 have the highest void ratios, increasing by 2.41% and 1.27%, respectively, when compared to 28 days. In addition, since CPB-D3 and CPB-P samples showed basic
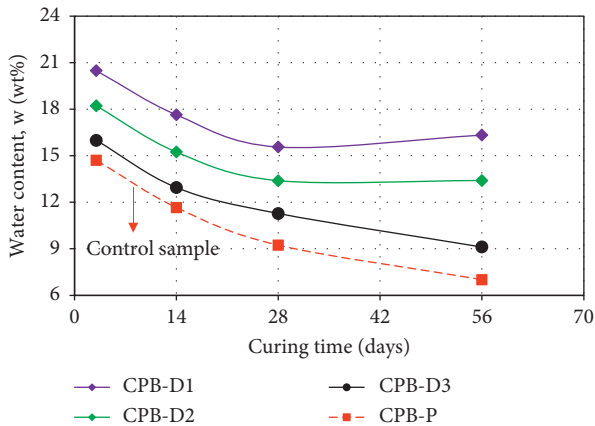
Figure 6: Change in water content with time for diverse mine backfills.
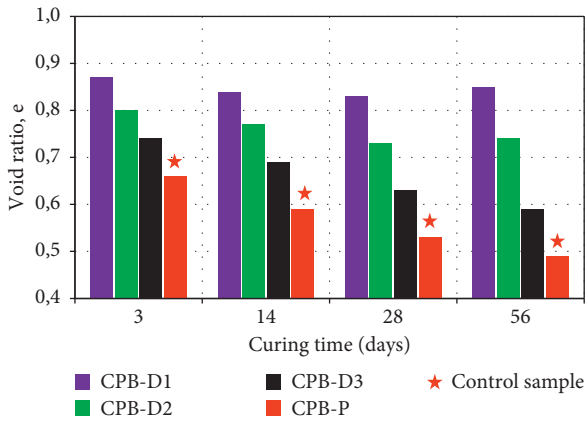
Figure 7: Change in void ratio with time for diverse mine backfills.

properties in the long term, hydration reactions were partially prevented and void ratios were low.

3.4.3. Assessment of Specific Surface Area.

SSA is interrelated by the setting development and final strength of CPB. As can be seen from Figure 8, fill's S_S performance increases with increasing cure time. The S_S values of all samples varied in the range of 4.11–12.0 m²/g, and the lowest S_S value was observed in CPB-D1 sample, while the highest S_S value was observed in reference sample (CPB-P). In addition, after 28-day curing time, S_S of samples increased, while S_S of CPB-D1 sample alone decreased by 1.26%. Although S_S is directly related to microstructure and grain size, it determines the reactivity of samples [53].

It is clear that fine-grained materials have larger S_S values than large-grained ones. As a result, a higher S_S means more surface to be cemented (escalated hydration products and decreased free water) [54]. This directly affects the performance of CPB positively. In addition, S_S changes in direct proportion to the packing density. Increasing the surface area increases the packing density, filling the spaces between the large particles in CPB and providing a more compact structure. As a result, the increase in packing density
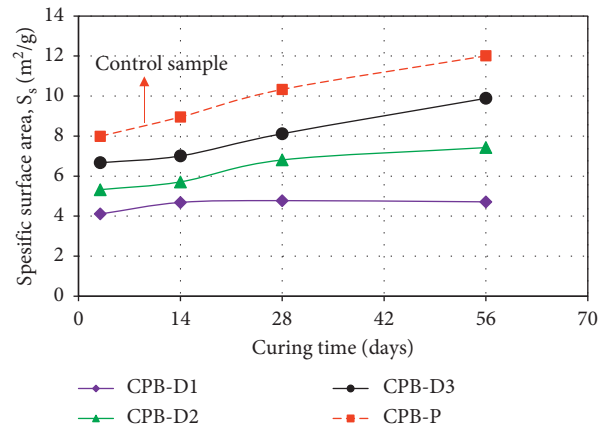
Figure 8: Change in S_s values with time for diverse mine backfills.

contributes to fill's strength increase [55]. However, S_S effect on CPB performance can be complex. In other words, although CPB grains with small surface areas are less reactive, grains with large surface areas show high reactivity due to high water retention [57]. As a result, oxygen diffusion and sulfide oxidation rate are affected. Increasing S_S (reducing grain size) increases the degree of liberation of harmful minerals such as sulfide and decreases pH of the environment [58]. Equally, a decrease in pH and the existence of harmful minerals such as sulfites cause an increase in S_S [59].

3.4.4. Assessment of Degree of Saturation.

Figure 9 displays variation in fill's saturation depending on cure time. S_r decreases with curing times of 3.14, 28, and 56 days. These reductions for 56-day cured CPB-D1, CPB-D2, CPB-D3, and CPB-P samples were 17.0%, 18.4%, 27.3%, and 33.1%, respectively, when compared to 3-day curing time. Fill's water consumption from completely saturated to incompletely saturated state can be clarified by cement hydration. S_r is greatly affected by fill's drainage ability. In particular, the bottom-perforated plastic containers increase the drainage ability of CPB and reduce its saturation over time. The smaller the degree of saturation, the larger the performance and stability of CPB [60]. The water consumption by cement hydration in CPB causes larger absorption (adsorption is directly related to CPB's pore structure) [61].

The increase in the suction force strengthens the bonds between CPB particles and contributes to the improvement of their strength and fracture resistance [62]. The saturation of all samples varied between 55.9% and 95.4%; the lowest S_r value was observed in CPB-P sample, while the highest S_r value was observed in CPB-D1 sample. Although the S_r values in samples continued to decrease after the 28-day curing period, the saturation degrees of 56-day cured CPB-D1 and CPB-D2 samples showed a small increase of 1.98% and 0.86%, respectively, when compared to 28-day curing time. Until the 28-day curing period, the amount of free water in samples is consumed due to the hydration process, but the saturation decreases.

However, after 28-day curing period, the oxidation of CPB-D1 and CPB-D2 samples damages the products created
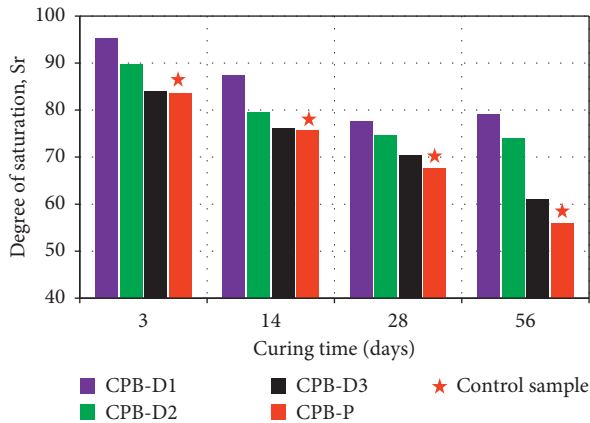
Figure 9: Change in the degree of saturation with time for diverse mine backfills.

by means of hydration. In particular, the mixing of sulfide minerals such as pyrite into pore waters breaks up C-S-H gels. The hydration's weakening causes water in the environment not to be consumed for the hydration process, which increases the saturation of CPB [63]. In addition, this high saturation or free water content allows the hydration products to crystallize [64]. Excess water remaining in sample cavities will evaporate over time, causing samples to have a hollow structure. This will cause strength losses in CPB as well as a decrease in toughness.

3.5. Interpretation on the Effect of Dam Tailings. When the variation of pH in the tested CPB samples is explored, it is apparent that there are serious differences between process tailings and the tailings collected from the dam. When the physical properties of CPB samples were examined, the increase in pH values supported the alkaline environment, causing an increase in hydration products and thus filling the voids in CPB with these products, thus reducing the porosity. The fill's water content decreased owing to void reduction and the consumption of pore water in hydration processes, as proven by Wang et al. [65]. Likewise, the degree of saturation decreased in parallel with the water content. The decrease in the amount of voids increases the strength of CPB [66]. The recent works done by Lopes et al. [67] clearly show the effect of pH on water content and void ratio. At the same time, acidification on the samples with the decrease of pH values caused direct erosion, reducing the grain size and causing structural deterioration. Considering the above-mentioned parameters, the effect of pH of samples on CPB performance was clearly observed. As a result, one can conclude that it is important to take into account the effects of acidic or basic while evaluating dam tailings as CPB.

4. Conclusions

The current work assesses the influence of pH of diverse tailings (e.g., dam and process) on quality and performance of CPB samples. Dam tailings are collected from three different locations of the dam while processing tailings are

collected from the discharge of filter. CPB samples were prepared by using these four tailings (three of them are in acidic condition, while one is basic condition). After curing for 3–56 days, all mine backfills were subjected to both UCS and geotechnical index tests. From the executed laboratory test works, some key assumptions can be made below:

(i) Regardless of the tailings type (dam or process tailings), the strengths of all CPB samples increased until 28 days. However, in comparison with 28-day cured backfills, the strength gains of 56-day cured CPB-D1 and CPB-D2 samples decreased by 6.5% and 26.1%, respectively.

(ii) According to stress-strain behaviors of 28-day and 56-day cured backfills, CPB-P had the highest stress value with brittle behavior, while CPB-D1 samples had higher strain and ductile behavior than others. The minimum E50 values of CPB-D1 were found to be 15 MPa, while the maximum E50 value of CPB-P samples was found to be 115 MPa for a given curing time.

(iii) The backfill's water contents reduced in the range of 20.3% to 52.4% during the 56-day curing time (compared to 3-day curing time). Similarly, after 56 days, fill's void ratios decreased between 2.30% and 25.8%, while their surface areas decreased by 14.6%–50.3%. Degree of saturation decreases between 16.6% and 33.1% after 56 days.

(iv) The geotechnical test results show that dam tailings should be treated with basic materials to reduce their harmful effects and, accordingly, to be refilled into underground mined-out stopes as a ground support element.

Finally, this study shows that tailings present in the dam can be very different from one to another because of climate and deposition conditions. Therefore, to prevent the negative effect of dam tailings, pH of the environment in the dam must be taken under control for sustainability. In the future works, the authors will consider CPB samples by adding different additives with various substitution ratios especially for problematic tailings such as acidic dam tailings.

Data Availability

No data were used to support this study.

Conflicts of Interest

The authors declare that they have no conflicts of interest.

References

[1] M. Bagheri, A. Bazvand, and M. Ehteshami, "Application of artificial intelligence for the management of landfill leachate penetration into groundwater, and assessment of its environmental impacts," *Journal of Cleaner Production*, vol. 149, pp. 784–796, 2017.

[2] A. Valentín-Vargas, J. W. Neilson, R. A. Root, J. Chorover, and R. M. Maier, "Treatment impacts on temporal microbial

community dynamics during phytostabilization of acid-generating mine tailings in semiarid regions," *The Science of the Total Environment*, vol. 618, pp. 357–368, 2018.

[3] S. Cao, D. Zheng, E. Yilmaz, Z. Y. Yin, G. L. Xue, and F. D. Yang, "Strength development and microstructure characteristics of artificial concrete pillar considering fiber type and content effects," *Construction and Building Materials*, vol. 256, Article ID 119408, 2020.

[4] E. I. Valenzuela, A. C. García-Figueroa, L. E. Amábilis-Sosa, F. E. Molina-Freaner, and A. M. Pat-Espadas, "Stabilization of potentially toxic elements contained in mine waste: A microbiological approach for the environmental management of mine tailings," *Journal of Environmental Management*, vol. 270, Article ID 110873, 2020.

[5] M. Sari, E. Yilmaz, T. Kasap, and N. U. Guner, "Strength and microstructure evolution in cemented mine backfill with low and high pH pyritic tailings: Effect of mineral admixtures," *Construction and Building Materials*, vol. 328, Article ID 127109, 2022.

[6] M. Jouini, C. M. Neculita, T. Genty, and M. Benzaazoua, "Environmental behavior of metal-rich residues from the passive treatment of acid mine drainage," *The Science of the Total Environment*, vol. 712, Article ID 136541, 2020.

[7] Q. Dong, B. Liang, L. Jia, and L. Jiang, "Effect of sulfide on the long-term strength of lead-zinc tailings cemented paste backfill," *Construction and Building Materials*, vol. 200, pp. 436–446, 2019.

[8] C. Mafra, H. Bouzahzah, L. Stamenov, and S. Gaydardzhiev, "Insights on the effect of pyrite liberation degree upon the acid mine drainage potential of sulfide flotation tailings," *Applied Geochemistry*, vol. 123, Article ID 104774, 2020.

[9] S. Mabroum, A. Aboulayt, Y. Taha, M. Benzaazoua, N. Semlal, and R. Hakkou, "Elaboration of geopolymers based on clays by-products from phosphate mines for construction applications," *Journal of Cleaner Production*, vol. 261, Article ID 121317, 2020.

[10] M. Benzaazoua, T. Belem, and E. Yilmaz, "Novel lab tool for paste backfill," *Canadian Mining Journal*, vol. 127, no. 3, pp. 31–33, 2006.

[11] H. Lu, C. C. Qi, C. Li, D. Gan, Y. Du, and S. Li, "A light barricade for tailings recycling as cemented paste backfill," *Journal of Cleaner Production*, vol. 247, Article ID 119388, 2020.

[12] M. Loutou, Y. Taha, M. Benzaazoua, Y. Daafi, and R. Hakkou, "Valorization of clay by-product from moroccan phosphate mines for the production of fired bricks," *Journal of Cleaner Production*, vol. 229, pp. 169–179, 2019.

[13] A. Raklami, A.-i. Tahiri, N. Bechtaoui et al., "Restoring the plant productivity of heavy metal-contaminated soil using phosphate sludge, marble waste, and beneficial microorganisms," *Journal of Environmental Sciences*, vol. 99, pp. 210–221, 2021.

[14] N. Araya, A. Kraslawski, and L. A. Cisternas, "Towards mine tailings valorization: Recovery of critical materials from Chilean mine tailings," *Journal of Cleaner Production*, vol. 263, Article ID 121555, 2020.

[15] E. Yilmaz, T. Belem, M. Benzaazoua, and B. Bussiere, "Assessment of the modified CUAPS apparatus to estimate in situ properties of cemented paste backfill," *Geotechnical Testing Journal*, vol. 33, no. 5, pp. 351–362, 2010.

[16] M. Ettoumi, M. Jouini, C. M. Neculita et al., "Characterization of phosphate processing sludge from Tunisian mining basin and its potential valorization in fired bricks making," *Journal of Cleaner Production*, vol. 284, Article ID 124750, 2021.

[17] B. Koohestani, A. K. Darban, P. Mokhtari, E. Darezereshki, E. Yilmaz, and E. Yilmaz, "Influence of hydrofluoric acid leaching and roasting on mineralogical phase transformation of pyrite in sulfidic mine tailings," *Minerals*, vol. 10, no. 6, 2020.

[18] F. Lessard, B. Bussière, J. Côté, M. Benzaazoua, V. Boulanger-Martel, and L. Marcoux, "Integrated environmental management of pyrrhotite tailings at Raglan Mine: Part 2 desulphurized tailings as cover material," *Journal of Cleaner Production*, vol. 186, pp. 883–893, 2018.

[19] J. R. Owen, D. Kemp, É. Lébre, K. Svobodova, and G. P. Murillo, "Catastrophic tailings dam failures and disaster risk disclosure," *International Journal of Disaster Risk Reduction*, vol. 42, Article ID 101361, 2020.

[20] C. Qi, A. Fourie, Q. Chen, and Q. Zhang, "A strength prediction model using artificial intelligence for recycling waste tailings as cemented paste backfill," *Journal of Cleaner Production*, vol. 183, pp. 566–578, 2018.

[21] P. Kinnunen, A. Ismailov, S. Solismaa et al., "Recycling mine tailings in chemically bonded ceramics - a review," *Journal of Cleaner Production*, vol. 174, pp. 634–649, 2018.

[22] I. Park, C. B. Tabelin, S. Jeon et al., "A review of recent strategies for acid mine drainage prevention and mine tailings recycling," *Chemosphere*, vol. 219, pp. 588–606, 2019.

[23] S. Cao, E. Yilmaz, Z. Y. Yin, G. L. Xue, W. D. Song, and L. J. Sun, "CT scanning of internal crack mechanism and strength behavior of cement-fiber-tailings matrix composites," *Cement and Concrete Composites*, vol. 116, Article ID 103865, 2021.

[24] Y. P. Kou, H. Q. Jiang, L. Ren, E. Yilmaz, and Y. H. Li, "Rheological properties of cemented paste backfill with alkali-activated slag," *Minerals*, vol. 10, no. 3, Article ID 288, 2020.

[25] S. Coussy, M. Benzaazoua, D. Blanc, P. Moszkowicz, and B. Bussière, "Assessment of arsenic immobilization in synthetically prepared cemented paste backfill specimens," *Journal of Environmental Management*, vol. 93, no. 1, pp. 10–21, 2012.

[26] S. Cao, G. L. Xue, E. Yilmaz, Z. Y. Yin, and F. D. Yang, "Utilizing concrete pillars as an environmental mining practice in underground mines," *Journal of Cleaner Production*, vol. 278, Article ID 123433, 2021.

[27] J. Zheng, L. Guo, X. Sun, W. Li, and Q. Jia, "Study on the strength development of cemented backfill body from lead-zinc mine tailings with sulphide," *Advances in Materials Science and Engineering*, vol. 2018, Article ID 7278014, 2018.

[28] S. Chen, W. Wang, R. Yan, A. Wu, Y. Wang, and E. Yilmaz, "A joint experiment and discussion for strength characteristics of cemented paste backfill considering curing conditions," *Minerals*, vol. 12, no. 2, Article ID 211, 2022.

[29] C. C. Qi and A. Fourie, "Cemented paste backfill for mineral tailings management: review and future perspectives," *Minerals Engineering*, vol. 144, Article ID 106025, 2019.

[30] B. Yan, H. Jia, E. Yilmaz, X. Lai, P. Shan, and C. Hou, "Numerical study on microscale and macroscale strength behaviors of hardening cemented paste backfill," *Construction and Building Materials*, vol. 321, Article ID 126327, 2022.

[31] I. Cavusoglu, E. Yilmaz, and A. O. Yilmaz, "Sodium silicate effect on setting properties, strength behavior and microstructure of cemented coal fly ash backfill," *Powder Technology*, vol. 384, pp. 17–28, 2021.

[32] G. Xue, E. Yilmaz, G. Feng, and S. Cao, "Analysis of tensile mechanical characteristics of fibre reinforced backfill through splitting tensile and three-point bending tests," *International*

Journal of Mining, Reclamation and Environment, vol. 36, no. 3, pp. 218–234, 2022.

[33] H. Jiang, J. Han, Y. Li, E. Yilmaz, Q. Sun, and J. Liu, "Relationship between ultrasonic pulse velocity and uniaxial compressive strength for cemented paste backfill with alkali-activated slag," *Nondestructive Testing and Evaluation*, vol. 35, no. 4, pp. 359–377, 2019.

[34] M. G. Sephton, J. A. Webb, and S. McKnight, "Applications of Portland cement blended with fly ash and acid mine drainage treatment sludge to control acid mine drainage generation from waste rocks," *Applied Geochemistry*, vol. 103, pp. 1–14, 2019.

[35] R. M. Kalombe, T. V. Ojumu, V. N. Katambwe et al., "Treatment of acid mine drainage with coal fly ash in a jet loop reactor pilot plant," *Minerals Engineering*, vol. 159, Article ID 106611, 2020.

[36] X. Dai, L. Ren, Z. Guo, E. Yilmaz, K. Fang, and H. Jiang, "Strength analysis and optimization of alkali activated slag backfills through response surface methodology," *Frontiers in Materials*, vol. 9, Article ID 844608, 2022.

[37] J. Helser, E. Vassilieva, and V. Cappuyns, "Environmental and human health risk assessment of sulfidic mine waste: bioaccessibility, leaching and mineralogy," *Journal of Hazardous Materials*, vol. 424, Article ID 127313, 2022.

[38] Z. Aldhafeeri and M. Fall, "Sulphate induced changes in the reactivity of cemented tailings backfill," *International Journal of Mineral Processing*, vol. 166, pp. 13–23, 2017.

[39] H. Li, A. Wu, and H. Wang, "Evaluation of short-term strength development of cemented backfill with varying sulphide contents and the use of additives," *Journal of Environmental Management*, vol. 239, pp. 279–286, 2019.

[40] L. Liu, J. Xin, C. Huan, C. C. Qi, W. Zhou, and K. I. Song, "Pore and strength characteristics of cemented paste backfill using sulphide tailings: effect of sulphur content," *Construction and Building Materials*, vol. 237, Article ID 117452, 2020.

[41] J. Zheng, X. Sun, L. Guo, S. Zhang, and J. Chen, "Strength and hydration products of cemented paste backfill from sulphide-rich tailings using reactive MgO-activated slag as a binder," *Construction and Building Materials*, vol. 203, pp. 111–119, 2019.

[42] B. Yan, W. Zhu, C. Hou, E. Yilmaz, and M. Saadat, "Characterization of early age behavior of cemented paste backfill through the magnitude and frequency spectrum of ultrasonic P-wave," *Construction and Building Materials*, vol. 249, Article ID 118733, 2020.

[43] A. Wu, Y. Wang, B. Zhou, and J. Shen, "Effect of initial backfill temperature on the deformation behavior of early age cemented paste backfill that contains sodium silicate," *Advances in Materials Science and Engineering*, vol. 2016, Article ID 8481090, 10 pages, 2016.

[44] S. G. Liu and M. Fall, "Fresh and hardened properties of cemented paste backfill: Links to mixing time," *Construction and Building Materials*, vol. 324, Article ID 126688, 2022.

[45] N. Zhou, C. Dong, J. Zhang, G. Meng, and Q. Cheng, "Influences of mine water on the properties of construction and demolition waste-based cemented paste backfill," *Construction and Building Materials*, vol. 313, Article ID 125492, 2021.

[46] Y. Wang, Y. Cao, L. Cui, Z. Si, and H. Wang, "Effect of external sulfate attack on the mechanical behavior of cemented paste backfill," *Construction and Building Materials*, vol. 263, Article ID 120968, 2020.

[47] K. Skrzypkowski, "3D numerical modelling of the application of cemented paste backfill on displacements around strip excavations," *Energies*, vol. 14, no. 22, Article ID 7750, 2021.

[48] A. Saedi, A. Jamshidi-Zanjani, and A. K. Darban, "A review of additives used in the cemented paste tailings: environmental aspects and application," *Journal of Environmental Management*, vol. 289, Article ID 112501, 2021.

[49] S. Cao, G. Xue, and E. Yilmaz, "Flexural behavior of fiber reinforced cemented tailings backfill under three-point bending," *IEEE Access*, vol. 7, no. 1, pp. 139317–139328, 2019.

[50] Y. Zhao, A. Taheri, M. Karakus, Z. Chen, and A. Deng, "Effects of water content, water type and temperature on the rheological behaviour of slag-cement and fly ash-cement paste backfill," *International Journal of Mining Science and Technology*, vol. 30, no. 3, pp. 271–278, 2020.

[51] U. G. Akkaya, K. Cinku, and E. Yilmaz, "Characterization of strength and quality of cemented mine backfill made up of lead-zinc processing tailings," *Frontiers in Materials*, vol. 8, Article ID 740116, 2021.

[52] B. Yan, X. Lai, H. Jia, E. Yilmaz, and C. Hou, "A solution to the time-dependent stress distribution in suborbicular backfilled stope interaction with creeping rock," *Advances in Civil Engineering*, vol. 2021, Article ID 5533980, 18 pages, 2021.

[53] X. Ke, X. Zhou, X. Wang, T. Wang, H. Hou, and M. Zhou, "Effect of tailings fineness on the pore structure development of cemented paste backfill," *Construction and Building Materials*, vol. 126, pp. 345–350, 2016.

[54] J. Qiu, Z. Guo, L. Yang, H. Jiang, and Y. Zhao, "Effect of tailings fineness on flow, strength, ultrasonic and microstructure characteristics of cemented paste backfill," *Construction and Building Materials*, vol. 263, Article ID 120645, 2020.

[55] Z. Huang, E. Yilmaz, and S. Cao, "Analysis of strength and microstructural characteristics of mine backfills containing fly ash and desulfurized gypsum," *Minerals*, vol. 11, no. 4, Article ID 409, 2021.

[56] J. Zheng, Y. Zhu, and Z. Zhao, "Utilization of limestone powder and water-reducing admixture in cemented paste backfill of coarse copper mine tailings," *Construction and Building Materials*, vol. 124, pp. 31–36, 2016.

[57] G. K. Erguler, Z. A. Erguler, H. Akcakoca, and A. Ucar, "The effect of column dimensions and particle size on the results of kinetic column test used for acid mine drainage (AMD) prediction," *Minerals Engineering*, vol. 55, pp. 8–29, 2014.

[58] B. Koohestani, A. K. Darban, E. Darezereshki, P. Mokhtari, E. Yilmaz, and E. Yilmaz, "The influence of sodium and sulfate ions on total solidification and encapsulation potential of iron-rich acid mine drainage in silica gel," *Journal of Environmental Chemical Engineering*, vol. 6, no. 2, pp. 3520–3527, 2018.

[59] A. Parbhakar-Fox, B. Lottermoser, and D. Bradshaw, "Evaluating waste rock mineralogy and microtexture during kinetic testing for improved acid rock drainage prediction," *Minerals Engineering*, vol. 52, pp. 111–124, 2013.

[60] I. L. S. Libos and L. Cui, "Effects of curing time, cement content, and saturation state on mode-I fracture toughness of cemented paste backfill," *Engineering Fracture Mechanics*, vol. 235, Article ID 107174, 2020.

[61] W. Xu and P. Cao, "Fracture behaviour of cemented tailing backfill with pre-existing crack and thermal treatment under three-point bending loading: Experimental studies and particle flow code simulation," *Engineering Fracture Mechanics*, vol. 195, pp. 129–141, 2018.

[62] J. Li, E. Yilmaz, and S. Cao, "Influence of solid content, cement/tailings ratio, and curing time on rheology and strength of cemented tailings backfill," *Minerals*, vol. 10, no. 10, Article ID 922, 2020.

[63] W. Li and M. Fall, "Sulphate effect on the early age strength and self-desiccation of cemented paste backfill," *Construction and Building Materials*, vol. 106, pp. 296–304, 2016.

[64] S. Yin, Y. Shao, A. Wu, H. Wang, X. Liu, and Y. Wang, "A systematic review of paste technology in metal mines for cleaner production in China," *Journal of Cleaner Production*, vol. 247, Article ID 119590, 2020.

[65] A. Wang, S. Cao, and E. Yilmaz, "Effect of height to diameter ratio on dynamic characteristics of cemented tailings backfills with fiber reinforcement through impact loading," *Construction and Building Materials*, vol. 322, Article ID 126448, 2022.

[66] A. B. Ghazi, A. Jamshidi-Zanjani, and H. Nejati, "Utilization of copper mine tailings as a partial substitute for cement in concrete construction," *Construction and Building Materials*, vol. 317, Article ID 125921, 2022.

[67] M. M. S. Lopes, L. G. Pedroti, A. F. de Oliveira et al., "Optimization of performance of sustainable paints using granite waste through the variation of particle size and pH," *Journal of Cleaner Production*, vol. 326, Article ID 129418, 2021.

Research Article

Utilization of Tea Industrial Waste for Low-Grade Energy Recovery: Optimization of Liquid Oil Production and Its Characterization

I. Kathir,[1] K. Haribabu,[2] Aditya Kumar,[3] S. Kaliappan , [4] Pravin P. Patil,[5] C. Sowmya Dhanalakshmi ,[6] P. Madhu ,[7] and Habtewolde Ababu Birhanu [8]

[1]Department of Electrical and Electronics Engineering, V.S.B.Engineering College, Karur, Tamilnadu 639111, India
[2]Department of Mechanical Engineering, SCAD College of Engineering and Technology, Cheranmahadevi 627414, Tamilnadu, India
[3]Department of Mechanical Engineering, Netaji Subhash University of Technology, New Delhi 110078, India
[4]Department of Mechanical Engineering, Velammal Institute of Technology, Chennai, Tamilnadu 601204, India
[5]Department of Mechanical Engineering, Graphic Era Deemed to Be University, Bell Road, Clement Town Dehradun, Uttarakhand 248002, India
[6]Department of Mechanical Engineering, SNS College of Technology, Coimbatore, Tamilnadu 641035, India
[7]Department of Mechanical Engineering, Karpagam College of Engineering, Coimbatore, Tamilnadu 641032, India
[8]Faculty of Mechanical Engineering, Arba Minch Institute of Technology, Arba Minch University, PO Box 21 Arba Minch, Ethiopia

Correspondence should be addressed to Habtewolde Ababu Birhanu; habtewold.ababu@amu.edu.et

Pyrolysis oil, produced from industrial as well as municipal solid wastes through pyrolysis, could be a viable renewable alternative fuel. In this study, abundantly available industrial tea wastes are used to produce liquid oil. Flash pyrolysis experiments on a fluidized bed reactor were performed to analyze pyrolysis characteristics. The study evaluated three important process parameters, that is, pyrolysis temperature (300–500°C), particle size (0.5–1.25 mm), and inert gas flow rate (1.5–2.25 m^3/hr). The thermogravimetric analysis of the tea wastes demonstrated that the thermal pyrolysis is possible to produce pyrolysis liquid and value added chemicals. The flash pyrolysis experiment produces maximum of 46.3 wt% liquid oil at the temperature of 400°C, particle size of 1.0 mm, and the sweep flow rate of 1.75 m^3/hr. The liquid products were analyzed for its physical and chemical characteristics using Fourier transform infrared spectroscopy (FTIR) and gas chromatography-mass spectroscopy (GC-MS). The heating value of the liquid products showed that it can be used as liquid fuels, and its elements can be used for various industrial applications.

1. Introduction

Biomass is the world's largest green energy source, accounting for 14% of global energy consumption. The expandable global population demand for energy ensures a need for continuous supply of energy in a sustainable manner. The unsustainable use of conventional fossil-based fuels escalating environmental repercussions motivates the researchers to find suitable alternative energy. As a renewable energy source, many industrial and agricultural wastes can be utilized directly to generate heat through combustion or indirectly through conversion to various forms of biofuel. The resurgence of energy from wastes collected through industrial and agricultural processing is generally known as waste to energy concept. It depicts a lot of attention towards economic development and environmental concern [1].

The industrial wastes are broadly classified into hazardous and nonhazardous wastes. The wastes emitted from

chemical processing, mining, and radioactivity are called hazardous wastes. On the other hand, the wastes from food processing units, construction, waste paper, sugar milling, and so on are all the examples for nonhazardous wastes. According to industrial regulations, the general waste treatment methods include intermediate treatment, landfill, and reuse, according to the regulation. When opposed to land filling technique, energy from industrial wastes is noteworthy since it not only provides fuels, it saves the environment from global warming [2], greenhouse gas emissions, and land utilization as well [3]. Production of liquid fuels from huge amount of industrial and bio based wastes is gaining popularity for the past three decades due to the benefits of using these resources as feedstock [4]. Biochemical and thermochemical processes are the major two types of conversion techniques for energy recovery from industrial based biomass materials [5]. There are numerous studies that have reported previously biomass conversion techniques in order to improve the yield quantity [6–8]. Compared to various biomass conversion processes, pyrolysis is an effective technique to produce biofuel from low-value, biomass, and biobased industrial wastes. Pyrolysis is the most efficient method for converting biomass to a liquid intermediate that can be refined into hydrocarbon biofuels and petrochemical substitutes. It is the process of heating an organic substance in the absence of air. The type and its composition play a major role in influencing pyrolysis process and its products. Fast and flash pyrolysis is gaining more interest among the researchers to transform biomass into fuel and chemicals at low cost [9]. Among liquid gas and char, pyrolysis liquid is being the most important product since it can be stored and transported easily. It is a complex mixture of chemical substances, predominantly oxygenates [10]. The general lignocellulosic composition of biomass materials varies from one type to another, which also affects the performance of the conversion system and characteristics of the end products [11]. Biomass with higher amount of cellulose and hemicellulose produces more number of liquid products, whereas the composition of lignin components produces liquid with higher viscosity. The presence of various lignocellulosic compositions in the biomass gives complexity during pyrolysis. This complexity poses numerous challenges when it is utilized in economic way. Therefore, a thorough understanding of them is essential for creating value-added products by pyrolysis [12].

The production of tea and its consumption depends on the population of the country. India is the second top country producing 1.2 million tons of tea every year and more than 70% of the total tea consumed within the country itself. The industrial tea wastes are disposed with sewage waste, which increases the acidity of the soil and soil fertility. Tea is the most frequently consumed beverage. On a daily basis, overall up to 20 billion cups are consumed around the world, which is equal to the total consumption of coffee, chocolate, and soft drinks. In India, the majority of tea manufacturers are not following the standards issued by the tea board authorities for tea waste disposal. For each batch processing, tea industries generate a considerable amount of tea wastes including their leaves, buds, and tender. The improper disposal of these wastes contaminates the environment, including soil, water, and air [13]. Tea industries and shops generate considerable amount of wastes, and India has a small number of tea waste purchasers. These wastes are occasionally used in the caffeine industry to extract caffeine and utilize a feed for poultry and pig. But these wastes contain a certain amount of tannic acid that limits the use for poultry and pigs feed [14]. According to Tamizselvan et al. [15], tea is grown over 5,66,660 hectares of land in India in 2020, producing up to 1250 million tones of dust per year. This huge amount of tea products generates 0.015 million tones of wastes. A minimum of 2 : 100 kg of tea wastes are produced during processing from the beginning to export, and the products are tested before export. The regulation board in India specified some standards in order to denature them by mixing with urea, cow manure, and other denaturants. Many researchers previously used many parts of the tea wastes for their study. Hussain et al. utilized tea leaves and transformed them as carbonaceous materials for adsorptive usage [16]. Soysa et al. used Ceylon refused tea waste for biocrude-oil production. The study compared the liquid products with Douglas fir and coffee ground oil. The study yielded oil with heating value of 15.6 MJ/kg with maximum yield of 57.2 wt% at 600°C reaction temperature. The authors suggested the produced oil to use as secondary fuel for furnace in tea industry process [17]. Recently, Tamizselvan et al. [15] utilized various parts of the tea plants for gasification to produce hydrogen rich gas products. The findings of the investigation showed that the produced gas contains considerable amounts of CO and H_2, and they suggested its use as low-grade fuel for burner.

This study focused on the use of collective industrial tea wastes for liquid oil generation via thermal pyrolysis, because the combustion pathway creates a huge amount of garbage, and it creates serious environmental issues, which is not feasible for Indian context. Pyrolysis is a potential alternative approach for extracting energy and value-added chemicals. The study focused on the effect of reactor temperature, feedstock size, and nitrogen flow rate to get optimum liquid oil though flash pyrolysis experiment.

2. Materials and Methods

2.1. Feedstock Collection and Preparation. The wastes are collected from local tea manufacturers and tea industries in Udhagamandalam, India. Before utilizing the collected wastes for pyrolysis process, they need to endure two preliminary steps like milling and screening. During initial examination, the moisture content in the samples is identified as more than 10 wt%. Subsequently, the materials were dried in the sunlight for minimum one week and furnace maintained at 100°C for nearly 2 hours. After drying, the feedstocks were crushed using ball mill and screened by sieve shaker to get four different sizes of 0.5, 0.75, 1.0, and 1.25 mm. Generally, the feedstock with minimum diameter is advised for thermochemical conversion processes in order to overcome the heat transfer restriction during process [18].

2.2. Characterization Study. The initial characterization study of tea wastes to find the suitability for pyrolysis process

was performed by proximate and ultimate analysis. The elemental analysis for the sample and liquid products was analyzed by Elementar Vario EL-III series. The heating value of the sample as well as liquid was measured using a bomb calorimeter (Parr-6772). The effect of applied heat on mass fraction of the material during pyrolysis process was investigated using TGA701 thermogravimetric analyzer heated at $10°C/min$ under N_2 environment.

2.3. Pyrolysis Setup and Procedure.

A series of pyrolysis experiments were performed in a lab-scale fluidized bed reactor consisting a reactor, biomass feeding system, sweep gas flow system, temperature control system, condenser with cooling circuit, and char separation system. Normal sand with average diameter of 0.5 mm is used within the reactor for fluidization purposes. The reactor is fully insulted with mineral wool and Chromel–Alumel to resist unnecessary heat loss from the reactor. The reactor is in cylindrical shape of 150 mm long and 50 mm diameter. The cyclone separators are attached with the outlet of the reactor to collect escaped char and dust from the reactor. The feedstock supplied to the reactor is allowed through screw feeder and hopper arrangement connected with a variable speed motor. The biomass particles were retained in the hopper and fed into the reactor with specific flow rate. A small rotameter is attached with nitrogen flow unit to measure and control the flow rate. The temperature of the reactor is measured using five K type thermocouple located at five different points inside the reactor, and the heat input is controlled by the autotransformer. After heating the sand particles to fixed temperature, the air was cut off, and N_2 was delivered. The velocity of the gas is maintained two times greater than minimum fluidization velocity of 0.11 m/s. The minimum fluidization velocity for this study is measured using a 1m long glass tube with a diameter of 50 mm [19]. For this analysis, 500 g of sand particles is used. Air was employed as the fluidizing gas, and its flow rate was monitored with a rotameter. The decrement of pressure in the glass column was measured with a Mercury manometer. The position of the bed material did not change when air was entered at first, and the pressure drop increases with increased flow rate and reaching a maximum value at the point of initial fluidization. Increment in velocity over that limit does not result in an increase in bed pressure drop, but the elements reorganize themselves to allow more space around them to accommodate further gas flow. Finally, the velocity is found by using formula $Q = AV$. The pyrolyzed gas was condensed for liquefaction using a condenser unit maintained with adequate cooing water.

The collected and screened tea wastes were successfully transformed into pyrolysis oil, noncondensable gas, and char by optimizing process parameters. The experimental aim is to collect large quantity of pyrolysis liquid. For this, the biomass material is fed into the reactor and is heated to the desired temperature. The evolved gases were then transferred through a condenser. The condensable volatiles are successfully converted into liquid and collected with the aid of water-cooling condensers. In order to get maximum condensation, the condensed water is maintained at $0°C$. The liquid products are measured directly in order to find the effective conversion rate. The char products are collected directly and weighed using weighing balance machine. The yield of noncondensable gases is calculated by simple material balance method. For the production of quantitative liquids, several experimental parameters, such as pyrolysis temperature (300 to $500°C$), particle size (0.5 to 1.25 mm), and fluidizing gas flow rate (1.5 to 2.25 m^3/hr), were optimized. Table 1 represents the experimental condition in each stage.

2.4. Liquid Phase Analysis.

The collected samples obtained at optimized experimental conditions were preserved and tested for their physical and chemical characteristics. FTIR and GC-MS were used to determine the organic and inorganic composition of pyrolysis liquid. The functional group present in the liquid was analyzed by BRUKER TENSOR 27 FTIR spectrometer. The FTIR spectra were collected in the range of 400–4000 cm^{-1} with 4 cm^{-1} resolution. The GC-MS analysis was performed using Thermo Scientific GC of capillary column (length: 30 m, diameter: 0.25 mm, film thickness: 0.25 μm), and a DSQ-II MS was utilized. The analysis is performed to acquire a better understanding of the aging process and the compositional changes in the liquid products. Table 2 illustrates the program utilized for GC-MS analysis. NIST MS library identifies the chromatographic peaks listed based on their retention time. The peak percentages were identified using total ion chromatogram peak area.

3. Results and Discussion

3.1. Feedstock Characterization.

Tables 3 and 4 portray proximate and ultimate analysis of the tea wastes. The analysis was done by following ASTM standards. The data showed higher percentage of volatile contents of 70.42 wt%, 19.52 wt% fixed carbon, 6.31 wt% moisture content, 3.75 wt % ash content with 46.3 wt% carbon, 6.1 wt% hydrogen, 3.7 wt% nitrogen, and 1.1 wt% sulphur. The presence of higher volatile matter in the tea wastes can yield maximum liquid products during pyrolysis reaction [20]. The nitrogen and sulphur contents were quite low, making it more environmentally-friendly when burning in the furnace. In addition to that, it has lower amount of moisture and medium level of ash content. The higher heating value of the material was recorded as 18.2 MJ/kg. The low heating value is primarily due to the high oxygen level of the sample.

3.2. Thermal Analysis.

Figures 1 and 2 show TGA and DTG results obtained under inert atmosphere. The analysis is done from atmospheric temperature to $600°C$. The initial mass fraction started at $75°C$ and reached maximum after $200°C$. In between $250°C$ and $450°C$, the maximum mass loss appeared. The volatiles present in the tea wastes were released more at this temperature range. The major source of the maximum mass loss at this range is due to higher degradation with high cellulose and hemicellulose content.

TABLE 1: Experimental condition.

Experimental aim	Ranges	Fixed parameters
Optimizing pyrolysis temperature ($^\circ$C)	300, 350, 400, 450 and 500	Particle size: 0.75 mm N_2 flow rate: 1.5 m^3/hr
Optimizing particle size (mm)	0.5, 0.75, 1.0 and 1.25	Temperature: 400°C N_2 flow rate: 1.5 m^3/hr
Optimizing sweep gas flow rate (m^3/h)	1.5, 1.75, 2.0 and 2.25	Temperature: 400°C Particle size: 1.0 mm

TABLE 2: GC-MS condition.

Instrumentation	Set parameter
GC conditions	
Column temperature	70°C
Injection type	Spit
Injection temperature	200°C
Split ratio	10
Carrier gas	Helium
Column length	30 m
Diameter	0.25 mm
Film thickness	0.25 μm
MS conditions	
Source temperature	200°C
Interface temperature	250°C
Range	50–650 m/z

TABLE 3: Proximate analysis in wt%.

Volatile matter	Fixed carbon	Moisture content	Ash content
70.42	19.52	6.31	3.75

TABLE 4: Ultimate analysis (ash free basis) in wt%.

Carbon	Hydrogen	Nitrogen	Sulphur	Oxygen[a]
46.3	6.1	3.7	1.1	42.8

[a]By difference.
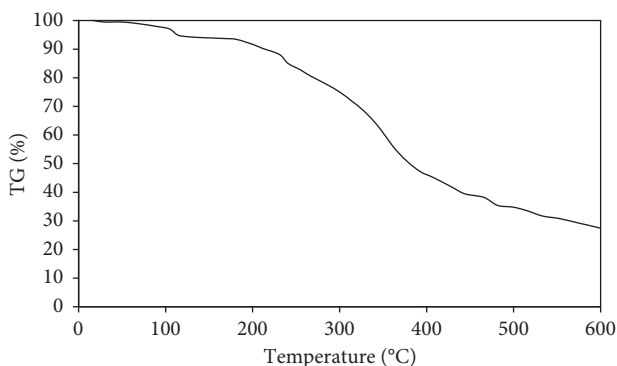
FIGURE 1: Thermogravimetric curve.

After reaching 500°C, no mass loss appeared. Cellulose, hemicellulose, and lignin are the common basic elements of all biomass material. The breakdown of these components has a significant impact on the yields of pyrolysis products. Previously, many researches have shown that hemicellulose begins to breakdown around 150–350°C, whereas cellulose
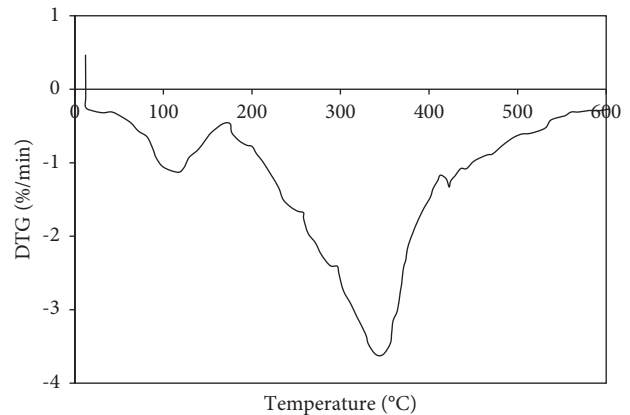
FIGURE 2: Derivative thermogravimetric curve.

degradation takes place between 275 and 350°C. However, breakdown of lignin occurs from 200 to 600°C [21]. According to these findings, the majority of weight loss occurs due to hydrocarbon volatilization at temperatures lower than 600°C. Hence, setting reaction temperature from 300 to 500°C is appropriate to produce liquid products [22].

3.3. Pyrolysis Yields

3.3.1. Influence of Temperature. The influence of reactor temperature on product distributions of industrial tea wastes is shown in Figure 3. As shown in the figure, the fraction of liquid products increases from 32.2 wt% to 39.2 wt% as the temperature rises from 300 to 400°C. The liquid yield is then decreased to 33.5 wt% as with the increase of temperature to 500°C. The reason behind the increased and decreased pattern of liquid yield is the multiple types of reactions in the reactor. The primary and secondary reactions inside the reactor are producing condensable vapors and gaseous products, which are then condensed to generate pyrolysis liquid [23]. The secondary reactions of the char particles produce more amount of noncondensable molecules and aid in increasing gas products. Generally, primary reactions reign at lower temperatures, and as reaction temperatures increases, the formation of vapor gets increased, resulting in increased vapor condensation and high liquid yield. However, further increase in temperature gives the way for secondary reactions, leading to more gaseous products [24]. When the temperature is increased above 400°C, the yield of char decreased, and the higher temperature boosts the conversion of carbon into gaseous products. Hence, the yield
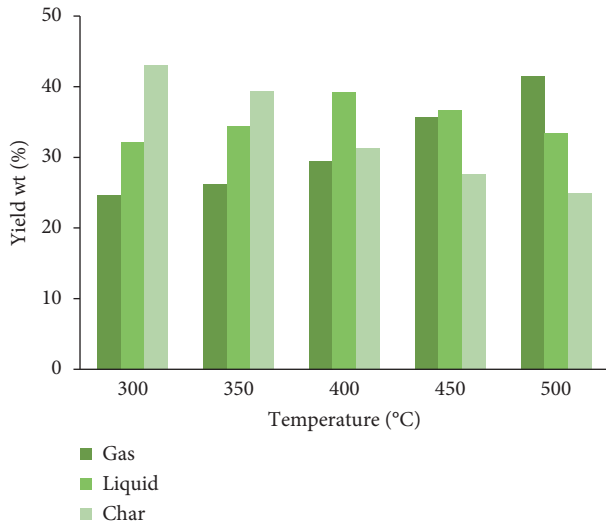
FIGURE 3: Effect of temperature on pyrolysis product yield.

FIGURE 4: Effect of particle size on pyrolysis product yield.

of gas is increased steadily from 24.7 wt% at 300°C to 41.5 wt % at 500°C. The yield of char is continuously decreased from 43.1 to 25.0 wt% for the temperature raises from 300 to 500°C. The increased char products at lower temperature are due to the lower decomposition of the feed particles at poor temperature, and further increase in temperature enhances the heat transfer from the outer to the center core and creates higher fraction of volatiles. A similar pattern was seen in the literature with various biomass samples [25, 26].

3.3.2. Influence of Particle Size. The size of the particles is an important one to consider for pyrolysis process since it influences the rate at which heat is transmitted to the center core of the biomass. The increased particle sizes slow down the heat passage from the hot to the cold end, which favors the yield of char [27]. Also, higher particle diameter is triggering secondary reactions and promotes them to yield more char. Figure 4 illustrates the effect of tea waste particle size on product yield. In this case, the yield of liquid products is enhanced from 37.6 wt% to 43.1 wt% as the particle size of biomass increases from 0.5 mm to 1.0 mm. The increment in particle size after 1.0 mm reduces the yield to 41.2 wt%. The change of biomass diameter from 0.5 mm to 1.25 mm did not much affect the production of char and gas. The production of char and gaseous products is changed from 32.5 wt% and 29.9 wt% to 30.1 wt% and 28.7 wt% when the decrement in the particle size is found from 0.5 mm to 1.25 mm. Only 7.38% and 4% differences were found for char and gas yield between these selected particle sizes. This is similar to previous investigations [28–30], which found that if the particle size was small enough, the particle could be heated uniformly. This study revealed that mass- and heat-transfer constraints had a significant impact on oil yield at large particle sizes exceeding 1.0 mm, resulting in lower liquid yield.

3.3.3. Influence of N_2 Flow Rate. Another component that has an impact on the yield is the flow of carrier gas or sweep
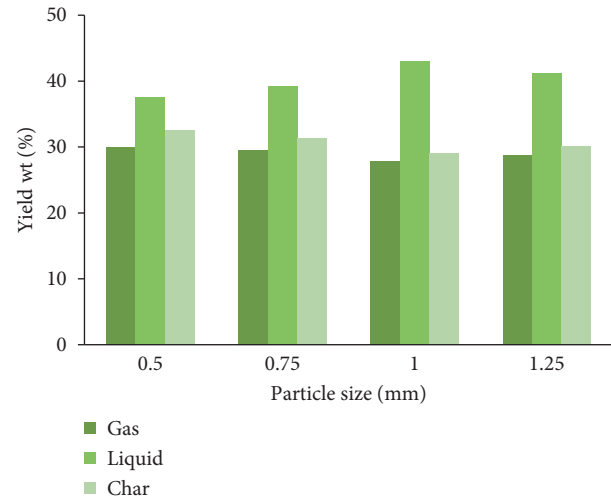
gas. During fluidized bed pyrolysis, a moderate to high amount of vapors are produced, and if they are not expelled, they might become involved in the secondary processes and alter the total composition [31]. Nitrogen, helium, and argon are the commonly used gases for sweeping purpose, out of which nitrogen is used for this study since it is nontoxic, less expensive than the others, and widely available. The improper flow rate not only affects the residence time, but also reduces the secondary breakdown of higher molecular weight products in the hot region. There are a large number of studies focusing on the yield trend by changing its sweep gas flow rate [32, 33]. The influence of N_2 flow rates on the yield of the products is depicted in Figure 5. The study shows higher liquid yield of 46.3 wt% at 1.75 m^3/h. However, it was shown that when the N_2 flow rate exceeded 1.75 m^3/hr, the production of the liquid fractions reduced significantly, which is related to the material fluidization characteristics, residence time, and the heat flow rate within the particle. In proportion to the increase in N_2 flow rate, the material inside the reactor becomes more vigorous and enhances heat transfer rate between fluidized medium and biomass. On the other side, there is reduction in residence time reducing the probability of tar cracking.

3.4. Characterization of the Liquid Products

3.4.1. Physical Characterization. Table 5 shows the elemental compositions and some of the basic properties of the liquid products obtained under optimized conditions. The liquid is found as denser than diesel fuel. The viscosity and flash point are recorded as 4.1 cSt and 135, respectively. Higher viscosity and density are closely related to the performance of the atomizer when it is used as the fuel for fire. The HHV is found as 21.34 MJ/kg, which is much better for pyrolysis oil produced from biomass materials. The property of the liquid obtained in this study is similar as the pyrolysis oil obtained from different biomass materials [34, 35].
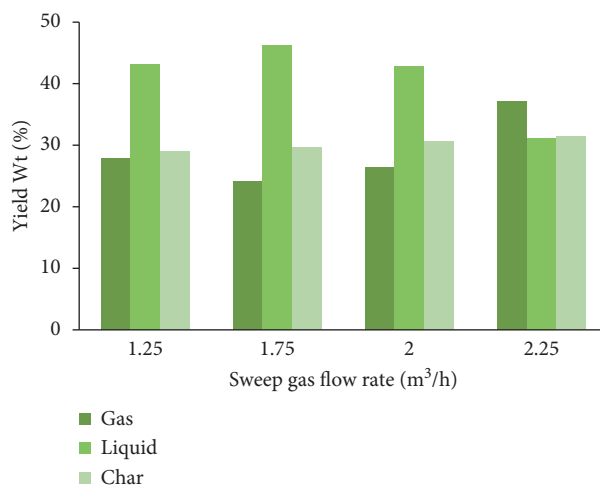
FIGURE 5: Effect of N_2 flow rate on pyrolysis product yield.

TABLE 5: Properties of the liquid.

Component	Value
Density (kg/m^3)	980
Viscosity (cSt)	4.1
Flash point (°C)	135
pH value	4.8
Carbon (wt%)	51.33
Hydrogen (wt%)	7.63
Nitrogen (wt%)	5.14
Sulphur (wt%)	0.02
Oxygen[a] (wt%)	35.88
H/C	1.771
O/C	0.524
HHV (MJ/kg)	21.34

[a]By difference, C,H,N,S-ash free basis.

FIGURE 6: FTIR spectra of the liquid.

3.4.2. FTIR Spectra Analysis. A large variety of complex organic compounds can be found in the oils. Figure 6 depicts the FTIR spectra of the entire liquid fractions. The identified phenols and alcohols are in the sample indicated by the presence of O–H stretching vibrations between 3000 and 3350 cm^{-1}. The existence of alkanes can be determined by the presence of C–H stretching vibrations in the spectra between 2750 and 2950 cm^{-1} and C–H deformation vibrations between 1300 and 1450 cm^{-1}. Furthermore, the bending vibration of C–H groups is located at 1287 cm^{-1} providing the existence of methyl groups in the sample. Carbonyl stretching absorptions are responsible for the presence of the band at approximately 1746 cm^{-1} in the spectra. The identification of C–O stretch at 1124 cm^{-1} and 1010 cm^{-1} indicates the presence of alcohols.

3.4.3. GC-MS Analysis. GC-MS spectroscopy was performed on the liquid sample that was obtained under optimal conditions. A total of 25 major compounds were acknowledged including phenols, alkenes, acids, furans, ketones, nitride, alcohols, and esters. In particular, D-glucopyranoside-D-glucopyranosyl, acetic acid, phenol, 2,6-dimethoxy, nonacosane, and some amounts of caffeine were

identified. The area percentages of D-glucopyranoside-D-glucopyranosyl, acetic acid, phenol, 2,6-dimethoxy, nonacosane, and caffeine are 14.22, 10.45, 7.97, 6.01, and 5.31, respectively. There were a number of additional substances identified in lower levels including 2-methoxy-4-methyl-phenol, 2-methyl-furan, phenol, 4-propyl, 2-phenyl-1-p-tolylethanol, ricinoleic acid, and phenol. The total number of components identified in GC-MS is listed in Table 6.

3.5. Industrial Applications of the Oil Product. The practical applicability of pyrolysis oils as a renewable fuel is still limited, but it is gaining more interests nowadays. The raw pyrolysis oils cannot be blended easily with conventional petroleum-based synthetic fuels [36]. However, the compounds extracted from this pyrolysis liquid can be broadly used in a variety of industries such as pharmaceutical, health care, and cosmetic. Phenols and their derivatives found in the oil are widely used in food, transportation, and coloring agents [37]. The presence of carbonyl compounds and acetic acid can be refined into natural antibacterial agents [38]. The fatty acid contents also can be used in the production of natural pesticide. The study suggests that the liquid products produced using industrial tea wastes eventually take the role

TABLE 6: GC-MS analysis of tea waste pyrolysis oil.

Rt (min)	Name of the compound	Molecular formula	Area %
1.01	2-Methoxy-4-methylphenol	$C_8H_{10}O_2$	1.90
1.21	2-Methyl- furan	C_5H_6O	2.62
1.56	Benzene	C_6H_6	0.92
2.09	Ethyl-piperidine	$C_7H_{15}N$	1.09
3.12	Methyl-pyridone	C_6H_7N	0.46
3.55	Phenol, 4-propyl-	$C_9H_{12}O$	5.44
4.01	Tridecylene	$C_{13}H_{28}$	5.51
6.41	Acetic acid	$C_2H_4O_2$	10.45
7.65	Eicosane	$C_{20}H_{42}$	2.44
7.92	Octadecenoic acid	$C_{18}H_{36}O_2$	5.02
10.46	Hexanedioic acid, bis(2-methylpropyl) ester	$C_{14}H_{26}O_4$	4.73
12.20	Nonacosane	$C_{29}H_{60}$	6.01
15.46	D-glucopyranoside,D-glucopyranosyl	$C_6H_{12}O_6$	14.22
15.92	Phenol, 2,6-dimethoxy	$C_8H_{10}O_3$	7.97
16.05	2-Phenyl-1-p-tolylethanol	$C_{14}H_{16}O$	3.90
16.67	Phenol	C_6H_6O	2.41
16.99	3-Methyl phenol	C_7H_8O	3.09
20.18	Tetradecane	$C_{14}H_{30}$	0.70
21.41	Ricinoleic acid	$C_{18}H_{34}O_3$	5.41
22.83	Caffeine	$C_8H_{10}N_4O_2$	5.31
24.67	Pyridine 2-methyl	C_6H_7N	0.63
25.72	4-Methyl-5h-furan-2-one	$C_5H_6O_2$	0.24
29.33	2,20-Dioxospirilloxanthin	$C_{42}H_{56}O_4$	3.66
31.41	4-Ethyl-2-methoxy phenol	$C_9H_{12}O_2$	1.40
33.69	1,2-Bis(20-quinolylmethyl)ethylene	$C_{20}H_{14}N_2$	3.20

of fossil asphalt due to its considerable heating value. The compounds extracted from pyrolysis oils show promise as environmental remediation agents.

4. Conclusion

The tea wastes obtained from industrial processes were collected and subjected to pyrolysis process with the aim of avoiding the disposal with sewage and utilizing it for energy recovery. The pyrolysis studies show higher liquid output of 46.3 wt% by keeping reactor temperature of 400°C, 1.0 mm particle size, and at N_2 flow rate of 1.75 m^3/hr. The results are explicitly that the yield of liquid is the function of pyrolysis temperature. In this study, temperature is the important factor that determine the yield rather than particle size and inert gas flow rate. Thus, a good platform is made thorough this study for the utilization of industrial tea wastes to produce burner oil with heating value of 21.34 MJ/kg. According to GC-MS investigation, the liquid product consists with a mixture of variety of oxygenated aromatics. The presence of phenols, carbonyl compounds, acetic acid, and fatty acid components can be used for pharmaceutical, health care, cosmetic, food, and transportation industries.

Abbreviations

FTIR: Fourier transform infrared spectroscopy
GC-MS: Gas chromatography-mass spectroscopy
CO: Carbon monoxide
H_2: Hydrogen
Q: Flow rate of the air (m^3/h)
A: Area of the fluidization column (m^2)
V: Velocity (m/s)
ASTM: American society for testing and materials
TGA: Thermogravimetric analysis
DTG: Derivative thermogravimetric
HHV: Higher heating value in (MJ/kg).

Data Availability

The data used to support the findings of this study are included within the article.

Conflicts of Interest

The authors declare that there are no conflicts of interest regarding the publication of this article.

References

[1] W.-T. Tsai, "Analysis of the sustainability of reusing industrial wastes as energy source in the industrial sector of Taiwan," *Journal of Cleaner Production*, vol. 18, no. 14, pp. 1440–1445, 2010.

[2] P. Stehlík, "Contribution to advances in waste-to-energy technologies," *Journal of Cleaner Production*, vol. 17, no. 10, pp. 919–931, 2009.

[3] C. S. Psomopoulos, A. Bourka, and N. J. Themelis, "Waste-to-energy: a review of the status and benefits in USA," *Waste Management*, vol. 29, no. 5, pp. 1718–1724, 2009.

[4] K. Shivaprasad, R. Rajesh, W. Anteneh Wogasso, B. Nigatu, and F. Addisu, "Usage of hydrogen as a fuel in spark ignition engine. In IOP conference series: materials science and engineering," *IOP Conference Series: Materials Science and Engineering*, vol. 376, no. 1, Article ID 012037, 2018.

 [5] K. N. Yogalakshmi, T. P. Devi, P. Sivashanmugam et al., "Lignocellulosic biomass-based pyrolysis: a comprehensive review," *Chemosphere*, vol. 286, Article ID 131824, 2021.

 [6] B. Zhao, D. O'Connor, J. Zhang et al., "Effect of pyrolysis temperature, heating rate, and residence time on rapeseed stem derived biochar," *Journal of Cleaner Production*, vol. 174, pp. 977–987, 2018.

 [7] G. Kabir, A. T. Mohd Din, and B. H. Hameed, "Pyrolysis of oil palm mesocarp fiber catalyzed with steel slag-derived zeolite for bio-oil production," *Bioresource Technology*, vol. 249, pp. 42–48, 2018.

 [8] R. Ravi, S. Pachamuthu, and P. Kasinathan, "Computational and experimental investigation on effective utilization of waste heat from diesel engine exhaust using a fin protracted heat exchanger," *Energy*, vol. 200, Article ID 117489, 2020.

 [9] J. Zhou, G. Liu, S. Wang, H. Zhang, and F. Xu, "TG-FTIR and Py-GC/MS study of the pyrolysis mechanism and composition of volatiles from flash pyrolysis of PVC," *Journal of the Energy Institute*, vol. 93, no. 6, pp. 2362–2370, 2020.

[10] N. S. Ab Rasid, M. Asadullah, and M. Asadullah, "Recent development of biomass fast pyrolysis technology and bio-oil upgrading: an overview," in *Advanced Materials Research* vol. 906, , pp. 142–147, Trans Tech Publications Ltd, 2014.

[11] S. Wang, G. Dai, H. Yang, and Z. Luo, "Lignocellulosic biomass pyrolysis mechanism: a state-of-the-art review," *Progress in Energy and Combustion Science*, vol. 62, pp. 33–86, 2017.

[12] T. Kan, V. Strezov, and T. J. Evans, "Lignocellulosic biomass pyrolysis: a review of product properties and effects of pyrolysis parameters," *Renewable and Sustainable Energy Reviews*, vol. 57, pp. 1126–1140, 2016.

[13] C. S. Dhanalakshmi, M. Mathew, and P. Madhu, "Biomass material selection for sustainable environment by the application of multi-objective optimization on the basis of ratio analysis (MOORA)," in *Materials, Design, and Manufacturing for Sustainable Environment*, pp. 345–354, Springer, Singapore, 2021.

[14] M. Kondo, M. Nakano, A. Kaneko, H. Agata, K. Kita, and H.-o. Yokota, "Ensiled green tea waste as partial replacement for soybean meal and alfalfa hay in lactating cows," *Asian-Australasian Journal of Animal Sciences*, vol. 17, no. 7, pp. 960–966, 2004.

[15] R. Tamizselvan, B. Devanand, S. S. Nanthini, T. Thavasivamanikandan, V. B. Varadha, and V. Kirubakaran, "Establishing auto gasification of tea waste," *AIP Publishing LLC*, vol. 2225, no. 1, Article ID 050006, 2020, March.

[16] S. Hussain, K. P. Anjali, S. T. Hassan, and P. B. Dwivedi, "Waste tea as a novel adsorbent: a review," *Applied Water Science*, vol. 8, no. 6, pp. 1–16, 2018.

[17] R. Soysa, Y. S. Choi, S. J. Kim, and S. K. Choi, "Fast pyrolysis characteristics and kinetic study of Ceylon tea waste," *International Journal of Hydrogen Energy*, vol. 41, no. 37, pp. 16436–16443, 2016.

[18] L. Zhang, C. Xu, and P. Champagne, "Overview of recent advances in thermo-chemical conversion of biomass," *Energy Conversion and Management*, vol. 51, no. 5, pp. 969–982, 2010.

[19] P. Madhu, H. Kanagasabapathy, and I. N. Manickam, "Conversion of cotton residues to bio-oil and chemicals through flash pyrolysis in a fluidised bed reactor," *International Journal of Energy Technology and Policy*, vol. 14, no. 1, pp. 20–33, 2018.

[20] H. Vasu, C. F. Wong, N. R. Vijiaretnam et al., "Insight into Co-pyrolysis of palm kernel shell (PKS) with palm oil sludge (POS): effect on bio-oil yield and properties," *Waste and Biomass Valorization*, vol. 11, no. 11, pp. 5877–5889, 2020.

[21] N. Ozbay, A. E. Pütün, and E. Pütün, "Bio-oil production from rapid pyrolysis of cottonseed cake: product yields and compositions," *International Journal of Energy Research*, vol. 30, no. 7, pp. 501–510, 2006.

[22] B. B. Uzun, E. Apaydin-Varol, F. Ateş, N. Özbay, and A. E. Pütün, "Synthetic fuel production from tea waste: characterisation of bio-oil and bio-char," *Fuel*, vol. 89, no. 1, pp. 176–184, 2010.

[23] S. Jalalifar, R. Abbassi, V. Garaniya, K. Hawboldt, and M. Ghiji, "Parametric analysis of pyrolysis process on the product yields in a bubbling fluidized bed reactor," *Fuel*, vol. 234, pp. 616–625, 2018.

[24] P. A. Horne and P. T. Williams, "Influence of temperature on the products from the flash pyrolysis of biomass," *Fuel*, vol. 75, no. 9, pp. 1051–1059, 1996.

[25] H. S. Choi, Y. S. Choi, and H. C. Park, "Fast pyrolysis characteristics of lignocellulosic biomass with varying reaction conditions," *Renewable Energy*, vol. 42, pp. 131–135, 2012.

[26] A. Trubetskaya, G. Surup, A. Shapiro, and R. B. Bates, "Modeling the influence of potassium content and heating rate on biomass pyrolysis," *Applied Energy*, vol. 194, pp. 199–211, 2017.

[27] J. M. Encinar, J. F. González, and J. González, "Fixed-bed pyrolysis of Cynara cardunculus L. Product yields and compositions," *Fuel Processing Technology*, vol. 68, no. 3, pp. 209–222, 2000.

[28] S. Zhang, Y. Liang, X. Qian, D. Hui, and K. Sheng, "Pyrolysis kinetics and mechanical properties of poly(lactic acid)/bamboo particle biocomposites: effect of particle size distribution," *Nanotechnology Reviews*, vol. 9, no. 1, pp. 524–533, 2020.

[29] A. El Hanandeh, A. Albalasmeh, and M. Gharaibeh, "Effect of pyrolysis temperature and biomass particle size on the heating value of biocoal and optimization using response surface methodology," *Biomass and Bioenergy*, vol. 151, Article ID 106163, 2021.

[30] R. E. Guedes, A. S. Luna, and A. R. Torres, "Operating parameters for bio-oil production in biomass pyrolysis: a review," *Journal of Analytical and Applied Pyrolysis*, vol. 129, pp. 134–149, 2018.

[31] M. Tripathi, J. N. Sahu, and P. Ganesan, "Effect of process parameters on production of biochar from biomass waste through pyrolysis: a review," *Renewable and Sustainable Energy Reviews*, vol. 55, pp. 467–481, 2016.

[32] Y. R. Wulandari, S. S. Chen, G. C. Hermosa et al., "Effect of N2 flow rate on kinetic investigation of lignin pyrolysis," *Environmental Research*, vol. 190, Article ID 109976, 2020.

[33] A. K. Varma, L. S. Thakur, R. Shankar, and P. Mondal, "Pyrolysis of wood sawdust: effects of process parameters on products yield and characterization of products," *Waste Management*, vol. 89, pp. 224–235, 2019.

[34] C. S. Dhanalakshmi and P. Madhu, "Recycling of wood bark of Azadirachta indica for bio-oil and chemicals by flash pyrolysis," *Indian Journal of Ecology*, vol. 46, no. 2, pp. 347–353, 2019.

[35] M. Nurul Islam, R. Zailani, and F. Nasir Ani, "Pyrolytic oil from fluidised bed pyrolysis of oil palm shell and itscharacterisation," *Renewable Energy*, vol. 17, no. 1, pp. 73–84, 1999.

[36] N. Hao, H. Ben, C. G. Yoo, S. Adhikari, and A. J. Ragauskas, "Review of NMR characterization of pyrolysis oils," *Energy & Fuels*, vol. 30, no. 9, pp. 6863–6880, 2016.

[37] L. Negahdar, A. Gonzalez-Quiroga, D. Otyuskaya et al., "Characterization and comparison of fast pyrolysis bio-oils from pinewood, rapeseed cake, and wheat straw using 13C NMR and comprehensive GC × GC," *ACS Sustainable Chemistry & Engineering*, vol. 4, no. 9, pp. 4974–4985, 2016.

[38] C. Mattos, M. C. C. Veloso, G. A. Romeiro, and E. Folly, "Biocidal applications trends of bio-oils from pyrolysis: characterization of several conditions and biomass, a review," *Journal of Analytical and Applied Pyrolysis*, vol. 139, pp. 1–12, 2019.

Research Article

Study on Mechanical Properties and Optimum Fiber Content for Basalt/Polyacrylonitrile Hybrid Fiber Reinforced Concrete

Zhenhai Zeng, Chuanxi Li [ID], Zhuoyi Chen [ID], and Lu Ke

School of Civil Engineering, Changsha University of Science and Technology, Changsha 410114, China

Correspondence should be addressed to Zhuoyi Chen; chenzhuoyi@csust.edu.cn

In order to obtain the design method of hybrid fiber reinforced concrete with better mechanical properties, the hybrid effect of fiber and the optimal fiber dosage are studied. In this paper, basalt fiber (B fiber) and polyacrylonitrile fiber (P fiber) were adopted. The mechanical properties such as compressive strength, splitting tensile strength, and bending toughness of concrete specimens with different fiber volumes were tested. The compressive strength, compressive modulus of elasticity, tensile strength, flexural capacity, and bending stress-strain curves of concrete with different fiber volumes were obtained, and the coefficient of hybrid effect and the ratio of toughness were calculated accordingly. The results show that the addition of fiber has little effect on the compressive modulus of elasticity of concrete, and the tensile strength, flexural strength, and toughness ratio are significantly increased, but the compressive strength is slightly decreased. The mechanical properties of hybrid fiber reinforced concrete, such as compressive strength, tensile strength, flexural strength, and toughness ratio, are better than those of single fiber reinforced concrete. The analysis of the fiber hybrid effect coefficient shows that there is a good hybrid effect between the two types of fibers. When the volume contents of B fiber and P fiber are, respectively, 0.15% and 0.11%, the comprehensive mechanical property of fiber reinforced concrete is the best. Meanwhile, the mechanical properties of the early-age concrete (3 d and 7 d) with this admixture are better than those of the plain concrete.

1. Introduction

After nearly 200 years of development since its inception, concrete has become one of the most important building materials in modern times, but its biggest disadvantage is brittle failure under load and durability problems [1]. Incorporating fibers is an effective way to improve the tensile and flexural properties of the concrete matrix [2–5]. Because the mechanical properties of fiber concrete are largely determined by the fiber properties [6–9] and the properties of each fiber have certain limitations, the reinforcement of a certain fiber alone is limited to the concrete matrix [10–13]. If fibers of different properties are added hybrid, fibers can complement each other through performance advantages to make the matrix have better performance at different levels and loading stages [14–17]. Huang et al. [18] mixed steel fiber (SF) and polypropylene fiber (PF) and conducted mechanical tests such as concrete bending resistance. The

results showed that the two kinds of fiber have a good mixing effect. The mechanical properties of compression and flexural strength are better than those of plain concrete and fiber-only concrete, and the flexural strength of concrete increases the most when the volumetric contents of steel fiber and polypropylene fiber are 0.7% and 0.3%, respectively. Pan [19] studied the influence of basalt fiber (BF) on the mechanical properties of the matrix, and the results showed that the incorporation of basalt fiber can effectively improve the compressive and flexural strength of concrete, with maximum increases of 20% and 22%, respectively. He et al. [20] studied the mechanical properties of basalt-polypropylene hybrid fiber concrete, and the results showed that the split tensile and flexural strength of hybrid fiber concrete was significantly higher than that of plain concrete and single-mixed fiber concrete. In the existing studies [16–22], most of the fiber hybrid methods use steel fiber, polypropylene fiber, or basalt fiber for hybridization, but

there are few reports on the hybridization of basalt fiber and polyacrylonitrile fiber. Studies have shown that the incorporation of fibers can also increase the early-age strength of concrete [23–25]. In this research, basalt fiber (B fiber) and polyacrylonitrile fiber (P fiber) are mixed to make fiber concrete, and the hybrid fiber concrete compressive, tensile, compressive elastic modulus, and flexural toughness tests are carried out, and the plain concrete and single fiber tests are carried out. The results are compared. In the bending toughness test, the stress-strain curve of the tension zone at the bottom of the test block will be obtained, and the toughness ratio of each test block will be obtained through integration. Subsequently, the best combination of the two fiber reinforced concrete matrixes was obtained by comprehensively combining the results of various mechanical performance tests. This paper will also study the mechanical properties of the concrete and plain concrete at the early ages (3 d and 7 d) of the cube compression and splitting tensile and flexural capacity under the optimal fiber blending ratio to verify the hybrid fiber early-age mechanical properties of concrete.

2. Experimental Program

2.1. Fiber Properties and Fiber Volume Content. Basalt fiber (B fiber) and polyacrylonitrile fiber (P fiber) produced by Wuhan Zhongding Economic Development Co., Ltd. were chosen. The specific material properties of the fiber are shown in Table 1, where ρ is the fiber density; σ_b is the tensile strength; E is the elastic modulus; l is the fiber length; d is the fiber diameter; δ is the fiber elongation at break. The fiber volume content is shown in Table 2.

2.2. Concrete Mix Ratio and Specimen Size. P.0 52.5 ordinary Portland cement produced by Shimen Conch Cement Co., Ltd. is used; coarse aggregate is continuous graded crushed stone (particle size 5~31.5 mm); fine aggregate is yellow sand with low mud content and good gradation; the superplasticizer produced by Hengyang Bangaoweiye Environmental Protection Building Material Technology Co., Ltd. has a water reduction rate of 31.2%; laboratory water. The fiber is measured by volume fraction, the amount of other materials is calculated by mass, and the accuracy of weighing meets the specification requirements. The concrete strength grade is C55. The specific configuration is shown in Table 3.

The test blocks were made in accordance with the "Test Regulations for Hydraulic Concrete" SL 352-2006 and "Standard for Test Methods of Fiber Concrete" CECS: 2009. The size of the cube compressive and split tensile test block is 150 mm × 150 mm × 150 mm, the axial compressive and compressive elastic modulus test block size is 150 mm × 150 mm × 300 mm, the size of the test block for the bending toughness test is 150 mm × 150 mm × 550 mm, and 3 pieces are poured in each group.

2.3. Test Methods. The test methods are those of compressive, tensile, compressive modulus of elasticity, and flexural toughness of the cube in "Testing Regulations for Hydraulic

TABLE 1: Material properties of fibers.

Fiber characteristics	BF	PF
ρ (kg·m^{-3})	2 650	1 180
σ_b (MPa)	4 550	979
E (GPa)	99	17.6
l (mm)	12	12
d (μm)	15	13
δ (%)	3.1	21

TABLE 2: Volume rate of fibers (%).

Concrete type	Symbol	BF	PF
Plain concrete	A-1	—	—
Single fiber concrete	A-2	0.1	—
	A-3	0.15	—
	A-4	0.2	—
	P-1	—	0.07
	P-2	—	0.09
	P-3	—	0.11
B-P hybrid fiber dimensional concrete	H-1	0.1	0.07
	H-2	0.1	0.09
	H-3	0.1	0.11
	H-4	0.15	0.07
	H-5	0.15	0.09
	H-6	0.15	0.11
	H-7	0.2	0.07
	H-8	0.2	0.09
	H-9	0.2	0.11

TABLE 3: Mix design of concrete (kg·m^{-3}).

Cement	Sand	Gravel	Water	Water reducing agent
494	649	1 204	153	9.39

Concrete" SL 352-2006 and "Standard for Test Methods of Fiber Concrete" CECS: 2009. 2 000 kN YES-2000B servo testing machine is selected for cube compression, compression elastic modulus, and split tensile and axial compression tests, and the loading rate is controlled at 6-7 kN/s.

The bending toughness test adopts three-point loading, and, at the same time, three resistance strain gauges with a length of 50 mm are sequentially pasted on the bottom surface of the test block in the mid-span transverse direction, as shown in Figure 1. The BX120-50AA series high-precision resistance strain gauge produced by Suzhou Tangdi Technology Co., Ltd. is used, and the load cell is the DYX-306 series cantilever sensor produced by Ningbo Zhongpeng Electric Co., Ltd. The strain value is read every 60 s, and the arithmetic mean value is taken as the tensile strain value in the middle of the test block, and the corresponding bending load is recorded. The test load is controlled by a constant rate, and the load rate is 0.2 mm/min until the test is terminated when the block is broken.

3. Results and Discussion

3.1. Compressive Performance. Figures 2 and 3 compare the results of the cubic compression and axial compression tests of plain concrete (PC) and fiber concrete test blocks.
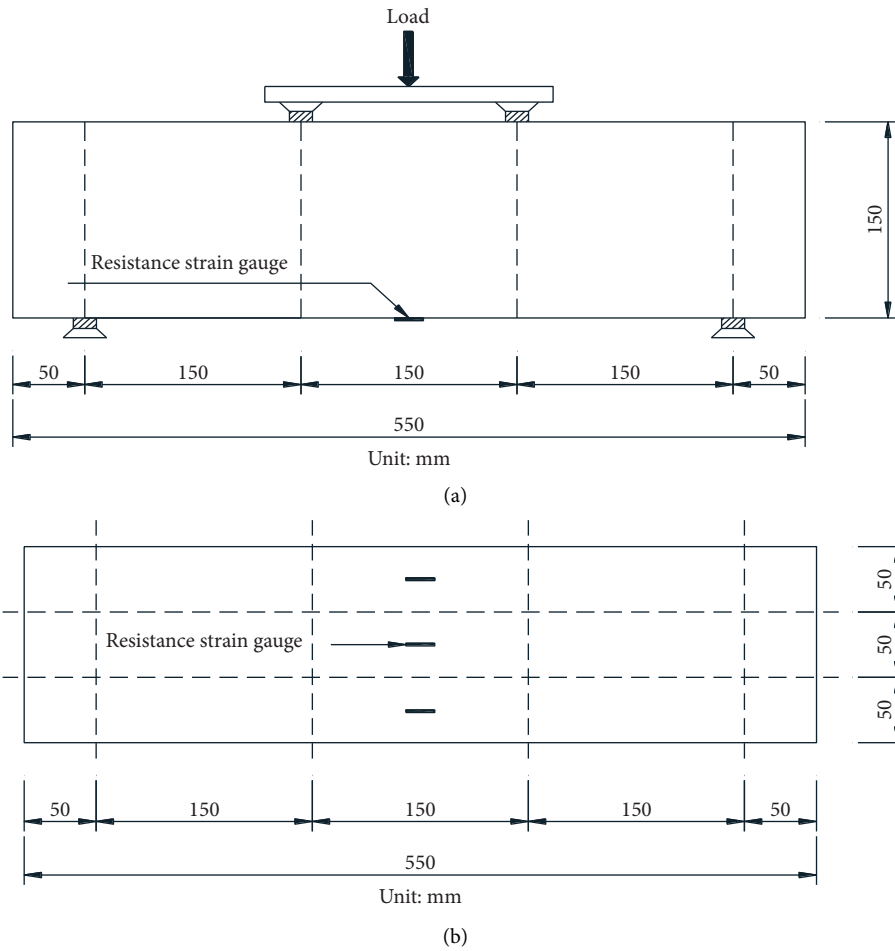
FIGURE 1: Flexural toughness test setup. (a) Side view. (b) Bottom of the test piece.
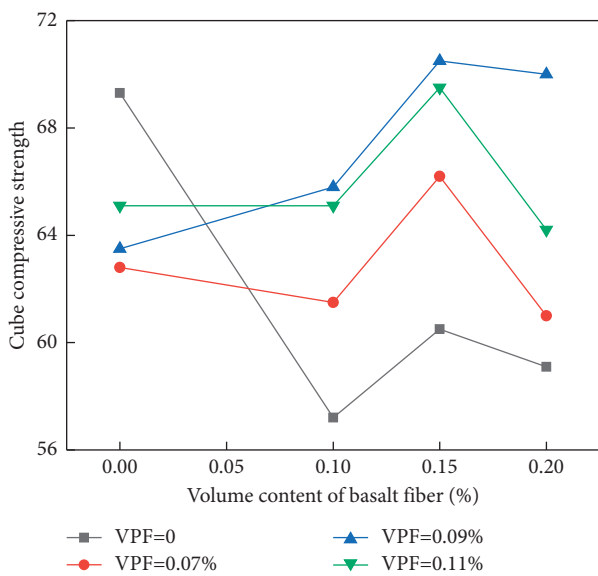
FIGURE 2: Cube compressive strength effect of concrete with different fiber volume rate.
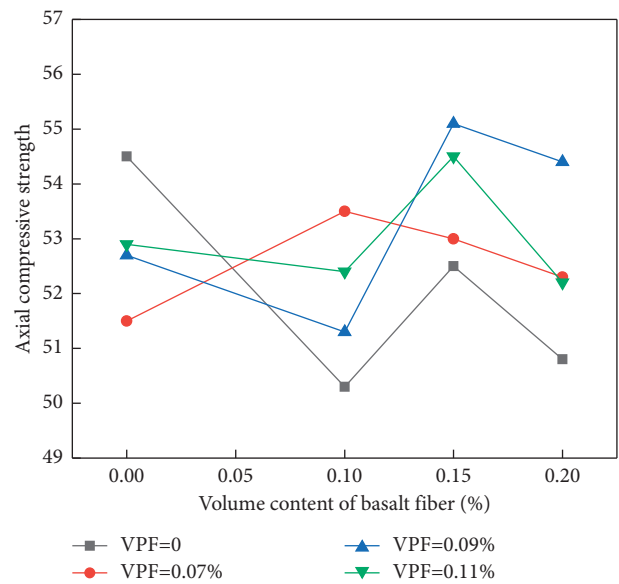
FIGURE 3: Axial compressive strength effect of concrete with different fiber volume rate.

Regarding the cubic compressive strength, (1) in the general trend, single blending or blending of fibers reduces the cubic compressive strength of the matrix by 0.6% to 17%. Only when the volumetric content of BF is 0.15% and its vicinity is ±0.05% and the volumetric content of PF is 0.09% and its vicinity is ±0.02% is the compressive strength slightly higher than that of plain concrete (PC) (1.5%~1.6%). The reason for the analysis is that, in the initial stage of concrete mixing and hardening, the fiber sinks due to its own gravity, resulting in uneven fiber distribution in the matrix, and, at the same time, the phenomenon of fiber sinking and agglomeration, resulting in a cavity in the matrix and a weak section. To a certain extent, it affects the compactness of the matrix, which in turn leads to a decrease in the compressive performance of the concrete matrix. (2) For the compressive performance of basalt fiber concrete (BFRC), with the increase of fiber volume, it shows a trend of first decreasing and then increasing; for the compressive performance of polyacrylonitrile fiber concrete (PFRC) and hybrid fiber concrete (HFRC), with the increase of the fiber volume content, there is a trend of first decreasing and then increasing and decreasing; the reason for the analysis is that when the fiber content is small, the number of effective "carrying networks" formed by the fibers in the matrix is also less. Insufficient quantities cannot overlap each other, which affects the compactness of the concrete matrix and reduces the compressive strength; when the volume of fibers gradually increases to a certain number, and as the "bearing network" increases and overlaps between each other to form a "transmission," "Strength bridge" can inhibit the generation and development of internal cracks in the matrix. When the cracks have appeared, the fibers can pull on the matrix around the cracks, thereby increasing the compressive strength; but when the fiber volume is mixed, when it is too large, the number of fibers in the matrix will be too much, and mutual interference will be formed between the fibers, which will affect the compactness and cohesiveness of the matrix, resulting in a decrease in the compressive strength of the concrete. (3) When the volume content of PF is in the range of 0.07%~0.09% and the volume content of SF is in the range of 0.1%~0.2%, the compressive strength of the PFRC test block is better than that of BFRC. (4) The 'negative effect" of the hybrid fiber on the compressive strength of the matrix is lower than that of the single-blended fiber. The reason is that the BF and PF have their own advantages. When they are mixed, the two types of fiber can "achieve strengths and avoid weaknesses" in the matrix and played a very good synergy. In summary, the H-5, H-6, and H-8 test blocks have relatively better compressive performance, (5) From Figure 2, it can be seen that the changing trend of the axial compressive strength of each fiber concrete and the cube resistance the changing trend of compression results are similar. (6) Integrating the results of the cube and axial compression tests, the optimal blending amounts of fiber in this test are $V_B = 0.15\%$ and $V_p = 0.09\%$ (H-5 test block).

The following can be seen from Figure 4. (1) The PC concrete test block almost immediately loses its ability to resist deformation after reaching the peak of the cubic compressive stress, showing obvious brittle failure;

meanwhile, for the fiber-doped concrete test block under the cubic compressive load, the stress-strain curve can be roughly divided into two stages, namely, the elastic stage and the plastic failure stage. After the load reaches the peak value, it can maintain a certain resistance to deformation. (2) It can be seen from Figure 4(a) that the stress-strain curve of the BFRC test block with different fiber volume content has a higher slope than the PC test block during the load rise stage, indicating that as the load increases, the BF blending increases the ability of concrete to resist deformation which is increased to a certain extent, and the ability to resist deformation is the largest when the volume of BFRC single fiber is 0.15%. (3) Figure 4(b) shows the stress-strain curve of the test block under different PFRC fiber volume content. When the PF volume content is 0.07%~0.09%, the strain rate (slope) of the PFRC test block is greater than that of PC, which indicates that when the load is rising, PF fiber also improves the ability of the matrix to resist deformation; when the PF content reaches 0.11%, the slope of the stress-strain curve of the PFRC test block is smaller than that of the PC, and the "negative effect" described above appears. (4) It can be seen from Figures 4(c) and 4(d) that the volumetric content of BFRP is 0.10%~0.15%, and when the content of PFRC is arbitrary, the slope of the stress-strain curve of the hybrid fiber concrete test block is uniform. Greater than PC, at this time, the two fiber hybrid effects show a synergistic effect and play a role in delaying deformation. When the BFRC volume content reaches 0.20%, only the slope of the H-8 test block is greater than that of the PC, indicating that, due to the excessive number of fibers, the fibers interfere with each other, which has a "negative effect" on the matrix. (5) Figure 2 and Table 4 show the results: when the fiber volume content of the BFRC test block is 0–0.2%, the compressive peak value shows a trend of first increasing and then decreasing; when the fiber volume content of the PFRC test block is 0, when ~0.11 changes, its compressive peak value also shows a trend of first increasing and then decreasing; for HFRC test block, when the volume of BF remains unchanged, its compressive peak value is large as the volume of PF increases, and it shows a trend of first increasing and then decreasing. When the volumetric content of PF remains unchanged, its compressive peak value generally shows a trend of first increasing and then decreasing with the increase of the volumetric content of BF.

3.2. Test Block Failure Form. In the cubic compression test, the PC, BFRC and HFRC blocks decrease immediately when the load reaches the maximum value. The surface of the PC test block fell off and was seriously damaged and finally showed an "I" shape or a cone shape; see Figure 5(a). The surface shedding phenomenon of BFRC test block is obviously better than that of PC, as shown in Figure 5(b); in the compression test of HFRC test block, when the load reaches the maximum value, it will not decrease immediately but will have a certain hysteresis, and most of the surface of the test block will not fall off by itself when it is broken, and it can maintain the original shape as a whole, as shown in Figure 5(c). From the damage morphology, it can be verified

(a)

(b)

(c)

(d)
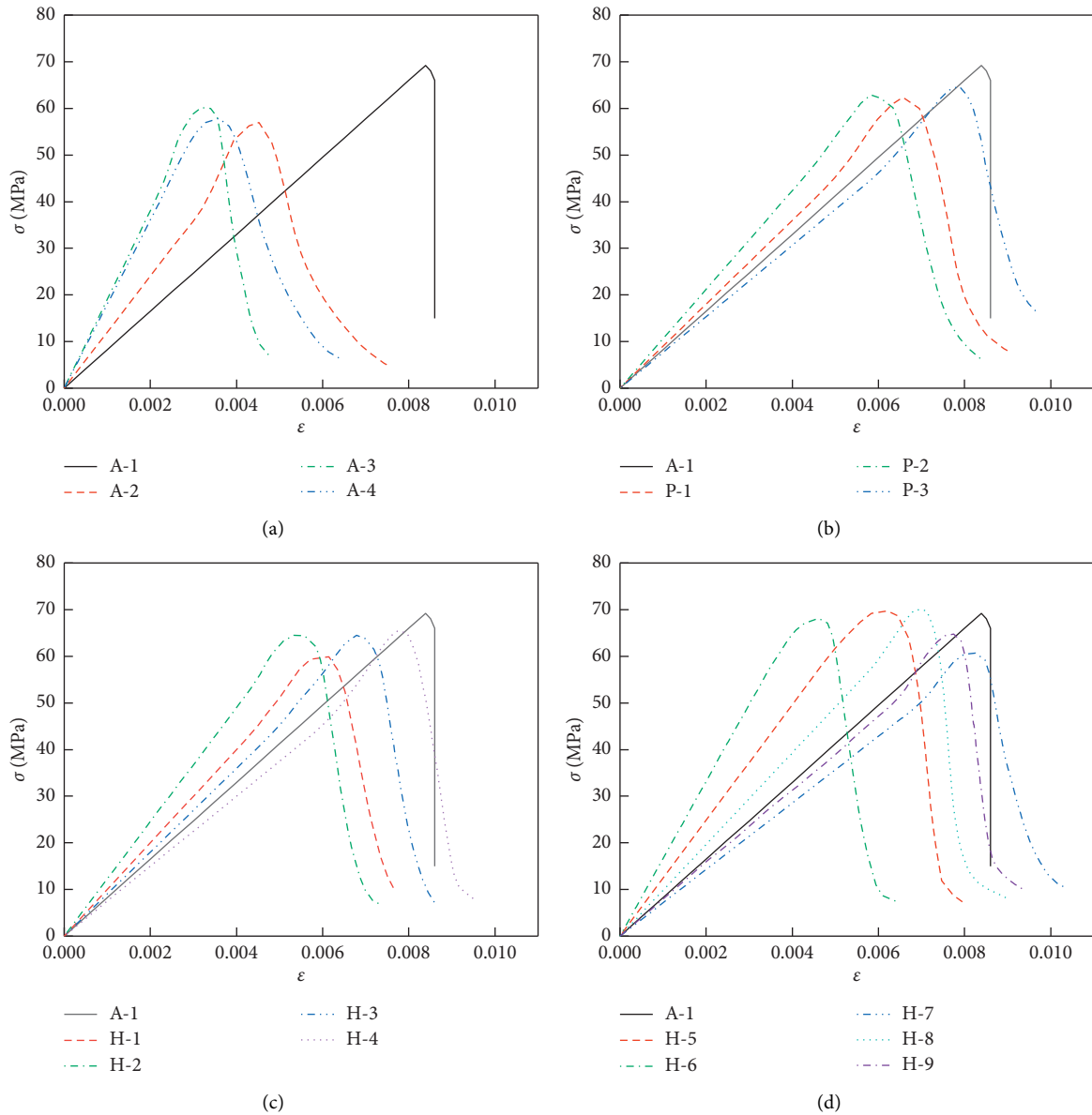
FIGURE 4: Comparison of cubic compressive stress-strain curves with different fiber content (before the peak). (a) PC and BFRC, (b) PC and PFRC, (c) PC and H-1~H-4, (d) PC and H-5~H-9.

that the fibers mentioned above can have a pulling effect on the matrix around the crack and can also have a certain inhibitory effect on the development of the crack. For the concrete test block, the failure mode in the axial compression test is basically the same as the cube compression test.

3.3. Tensile Performance. Figure 6 shows the comparison of split tensile test results between the PC test block and fiber concrete test block. The results show the following: (1) The incorporation of fibers can significantly improve the tensile properties of the concrete matrix. In the case of fiber mixing, except for the H-1 and H-4 test blocks, which are slightly lower than PC, all the test blocks have a greater improvement. The maximum increase can reach

18.6%. (2) For the single-mixed fiber concrete, except for the BFRC test block with a volume of 0.1% BF, which is 5.5% lower than that of PC, the tensile properties of all the other single-mixed fiber test blocks are better than those of PC. The range is 1.5%~17.5%. At the same time, for BFRC test block and PFRC test block, the tensile strength increases with the increase of fiber volume. (3) When the volume of BF is in the range of 0% to 0.15%, the volume of PF is 0.09% and 0.11. % tensile strength is obviously better than 0% and 0.07% series; this is because when the total fiber content is not large, the small and low elastic modulus of PF which is more uniformly dispersed into the matrix during the mixing process to improve the fiber distribution inside the matrix is greatly reduced so that the probability of larger fiber spacing and early cracks in the matrix is greatly reduced. However, when the volume

TABLE 4: Calculation results of fiber mixed effect coefficient.

Symbol	Cube compressive			Splitting tensile			Flexural capacity		
	f_{cc} (MPa)	f_{ct} (MPa)	α	f_{cc} (MPa)	f_{ct} (MPa)	α	f_{cc} (MPa)	f_{ct} (MPa)	α
H-1	61.01	57.39 / 62.36	0.37	4.6	4.42 / 4.73	0.29	5.62	6.06 / 5.37	0.35
H-2	65.29	57.39 / 63.40	0.48	5.14	4.42 / 4.93	0.49	6.7	6.06 / 5.73	0.55
H-3	64.96	57.39 / 65.22	0.45	5.6	4.42 / 5.51	0.58	6.58	6.06 / 6.01	0.52
H-4	66.11	60.21 / 62.36	0.52	4.6	4.7 / 4.73	0.28	5.95	6.6 / 5.37	0.38
H-5	70.24	60.21 / 63.4	0.57	5.03	4.7 / 4.93	0.51	6.23	6.6 / 5.73	0.44
H-6	68.7	60.21 / 65.22	0.54	5.79	4.7 / 5.51	0.63	6.85	6.6 / 6.01	0.58
H-7	60.97	58.54 / 62.36	0.36	4.7	5.15 / 4.73	0.32	5.73	6.55 / 5.37	0.33
H-8	70.13	58.54 / 63.4	0.57	5.01	5.15 / 4.93	0.48	5.83	6.55 / 5.73	0.35
H-9	64.97	58.54 / 65.22	0.45	4.37	5.15 / 5.51	0.23	5.98	6.55 / 6.01	0.38
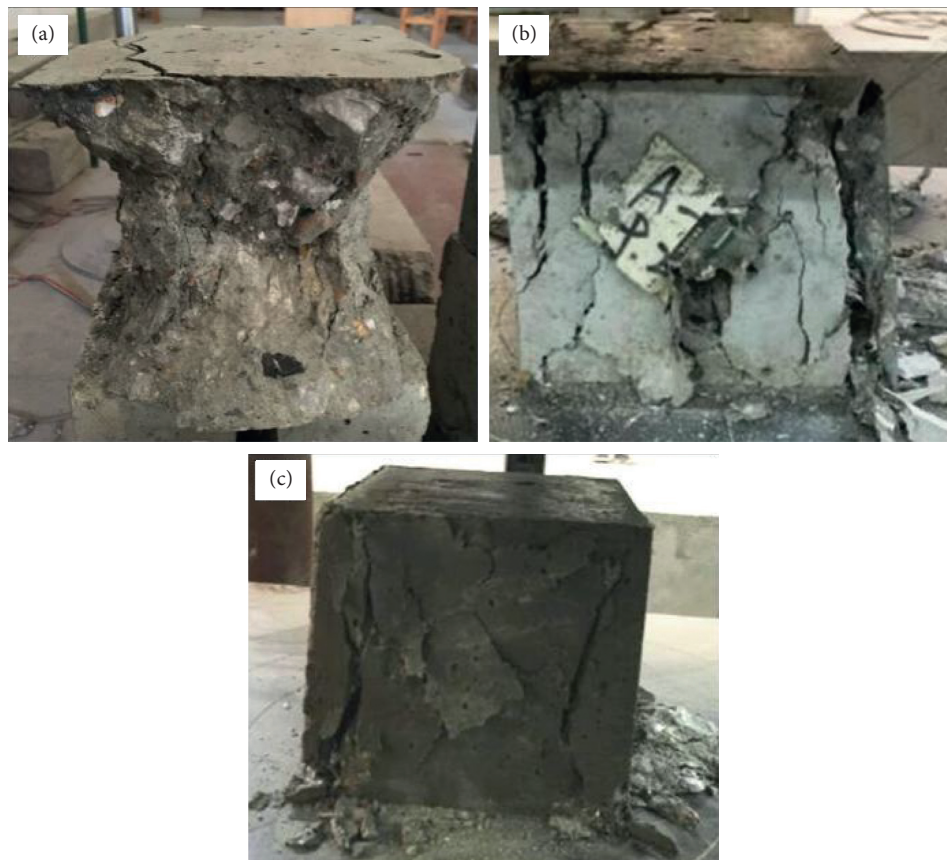
FIGURE 5: Block destroyed mode of cubic compression. (a) PC, (b) BFRC, and (c) HFRC.

of BF content reaches 0.2%, the tensile strength of the 0.11% series of PF content drops sharply, indicating that the "negative effect" mentioned above will be highlighted when the total amount of fiber is too large. (4) For PF, the tensile strength of the test blocks with the volume contents of 0% and 0.07% showed a trend of first decreasing and then increasing with the increase of the BF content, while the test blocks with the volume contents of 0.09% and 0.11% reduced first and then increased. This is because the synergistic effect of various fibers at different
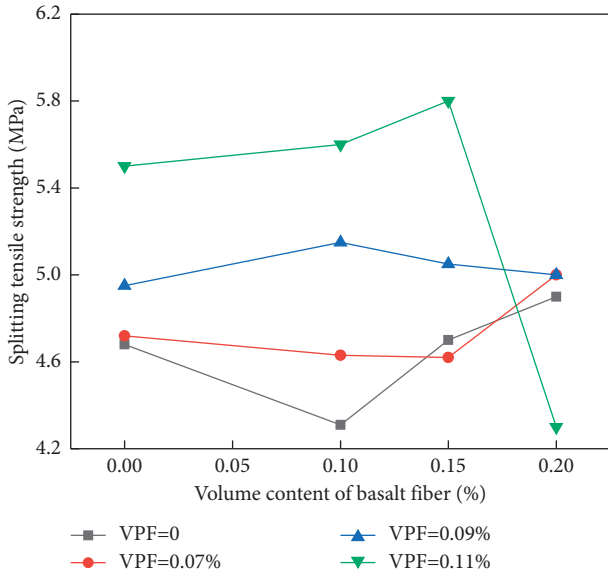
FIGURE 6: Splitting tensile strength effect of concrete with different fiber volume rate.

FIGURE 7: Compression modulus effect of concrete with different fiber volume rate.

stages and different structural levels of the test block will change with the change of fiber volume. That is, when the fiber content is small, the number of fibers in the matrix forming an effective "bearing network" is small and they cannot overlap each other, which affects the compactness of the concrete matrix and causes the splitting tensile strength to decrease; when the fiber volume gradually increases to a certain amount, as the "bearing network" increases and the fibers overlap each other to form a "force transmission bridge," it can inhibit the generation and development of internal cracks in the matrix and can also pull the matrix around the cracks. To increase the splitting tensile strength, at the same time, too much fiber will cause the performance of the matrix to decrease. (5) For splitting, the results of the crack tensile test showed that the tensile strength of H-6 specimens was the highest when the BF content was 0.15% and the PF content was 0.11%, which was 18.6% higher than that of PC.

3.4. Compressive Modulus of Elasticity. The comparison between the compressive elastic modulus test results of each fiber concrete test block and PC is shown in Figure 7. It can be seen that the compressive elastic modulus of each fiber concrete test block has a small change range compared with PC, and the maximum fluctuation range is only 4.1%. Because its test value largely depends on the axial compressive strength value, the overall change trend is also similar to the axial compressive strength. According to the principle of superposition in material mechanics, the elastic modulus of the composite can be considered as the sum of the product of the matrix and fiber's respective elastic modulus and the volume rate (1). Therefore, when the absolute value of the fiber content is low and considering the "negative effect" of fiber concrete, the change of its elastic modulus is very limited.
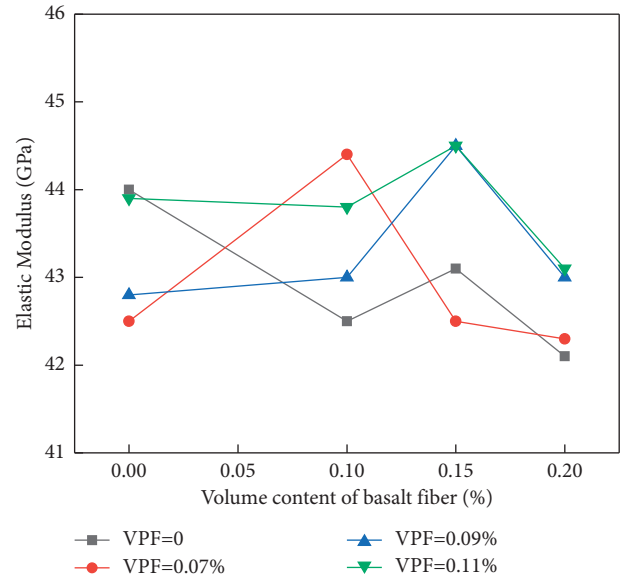
$$E = E_{\text{ft}} + E_B V_B + E_P V_P. \tag{1}$$

In the above formula, E is the elastic modulus of fiber concrete; E_{ft}, E_B, and E_P are the elastic moduli of plain concrete, BF, and PF, respectively; V_B and V_P are the volume contents of BF and PF, respectively.

3.5. Calculation of Flexural Toughness Ratio. The bending stress can be calculated according to formula (2). The toughening effect of fiber on concrete or the deformability of fiber concrete is usually expressed by the toughness R. The toughness of each test block in this paper is calculated by the bending load stress-strain curve. The stress-strain curve of each concrete test block is shown in Figure 6.

$$\sigma_f = \frac{Pl}{bh^2}, \tag{2}$$

where P is the bending load, N; l is the span, $l = 3\,h$, mm; b and h are the width and height, respectively, of the test block section, mm.

In the test, it was found that, with the increase of the load, the cracks on the bottom surface of the trabecular continued to increase. When the cracks developed to a certain width, the midspan tensile strain changed significantly and even became negative. At this time, the resistance strain gauges have been broken. Furthermore, after the PC reaches the peak of the bending load, it quickly breaks and loses its continued load-bearing capacity. Therefore, this paper only plots the stress-strain curve before the test beam reaches the peak of the bending load.

The area enclosed by the stress-strain curve of each test block is calculated by integrating the stress-strain curve of each test block, and this area is the corresponding bending toughness of the test block [26]. In this paper, the area enclosed by the PC block curve is taken as the unit area, and

TABLE 5: Calculation results of the ratio of toughness.

Symbol	σ_f (MPa)	D (mm)	R_x
A-1	5.08	5.3	1
A-2	5.17	8.9	1.8
A-3	5.73	9.5	2.5
A-4	6.01	9.2	2.4
P-1	6.16	10.5	2.0
P-2	6.6	13.6	2.7
P-3	6.55	11.9	2.7
H-1	5.82	12.2	3.5
H-2	6.7	14.8	3.7
H-3	6.58	13.1	3.5
H-4	5.95	9.9	3.1
H-5	6.23	10.8	3.6
H-6	6.85	15.3	4.4
H-7	5.73	12.9	2.9
H-8	5.83	10.9	3.2
H-9	5.98	8.3	3.6
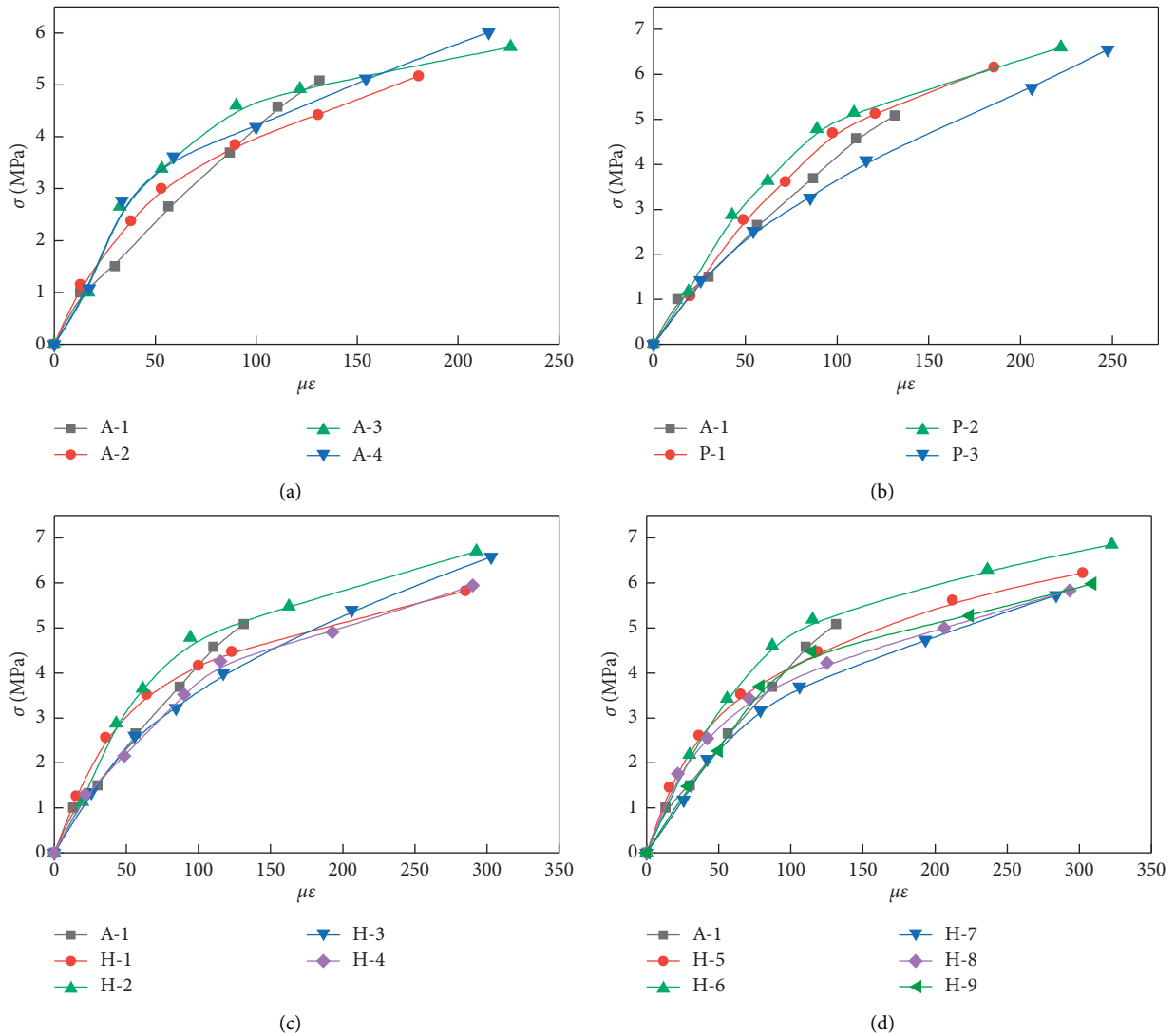
FIGURE 8: Comparison of stress-strain curves of concrete with different volume rates of fibers (before the peak value of flexural capacity). (a) PC and BFRC, (b) PC and PFRC, (c) PC and H-1~H-4, (d) PC and H-5~H-9.

TABLE 6: Mechanical properties of H-6 specimen and unreinforced concrete at an early age.

Symbol	f_{cc} (MPa)			f_{ts} (MPa)			σ_f (MPa)		
	3 d	7 d	28 d	3 d	7 d	28 d	3 d	7 d	28 d
A-1	56.39	60.96	69.11	3.94	4.41	4.88	4.47	4.89	5.08
H-6	60.52	63.00	68.70	4.75	5.24	5.79	5.31	5.97	6.85

the ratio of the toughness of each fiber concrete block to PC is the toughness ratio R_x. Table 5 shows the peak flexural stress σ_f (accurate to 0.01 MPa), the flexural elastic modulus E_f (accurate to 1 MPa), the maximum crack width D in the middle of the span, and the toughness ratio R_x (accurate to 0.01 MPa).

The following can be seen from Figure 8 and Table 5. (1) The PC test block quickly broke after reaching the peak of the bending stress and lost its deformability, showing obvious brittle failure, while the fiber concrete test block remained deformed after the peak. The toughness ratio increases with the increase of BF and shows a decreasing trend. (2) Figure 8(a) shows that the stress-strain curve of the BFRC test block with different fiber volume content has a larger slope before it intersects with the PC, indicating that BF has a role in delaying the deformation as the load increases in the first half of the deformation. The toughness of the matrix is increased to a certain extent. (3) When the volume of PF is between 0.07% and 0.09%, the strain rate or slope of the PFRC test block is less than that of PC, and PF also plays a role in delaying deformation. When the PF volume content increases to 0.11%, the "negative effect" mentioned above occurs, and the strain rate of the PFRC test block is larger. (4) The calculation result of the bending resistance peak value shows that when the fiber volume content in the BFRC test block is in the range of 0~0.2%, the peak value of bending resistance increases with the increase of fiber; when the volume of fiber in the PFRC test block is in the range of 0~0.11%, the peak value of bending resistance first increases and then decreases; for the HFRC test block, when the volumetric content of BF remains unchanged, its peak bending resistance shows an increasing trend with the volumetric content of PF. When the volumetric content of PF remains unchanged, its peak bending resistance increases with the increase of BF. The trend is first roughly increasing and then decreasing. (5) The calculation results of the toughness ratio show that, for the single fiber concrete test block, within the fiber volume content range in this paper, the toughness ratio basically increases with the increase of the fiber volume content. For the HFRC test block, when the BF content remains the same, the toughness ratio basically increases with the increase of PF; when the PF content remains the same, plastic failure is obviously shown. It shows that, within the range of fiber content specified in this study, PF has a better toughening effect on the matrix than BF. (6) When the fiber content is large, it will also have a "negative effect" on the toughness ratio of the HFRC test block, such as H-7 and H-9 test blocks, which have the best toughness ratio compared to H-6. The test block

decreased by 34% and then 18%, but the toughness ratio of the HFRC test block was better than that of the single-doped fiber test block.

3.6. Early-Age Concrete Mechanical Properties. Through the test results and calculations, it can be obtained that the relative best combination of hybrid fiber blending amounts in this test is $V_B = 0.15\%$ and $V_P = 0.11\%$ (H-6 test block). Table 6 shows the test results of the cubic compressive strength f_{cc}, splitting tensile strength f_{ts}, and flexural bearing capacity σ_f of the early age (3 d and 7 d) of the PC test block.

The results show that fiber can also significantly enhance the mechanical properties of early-age concrete. Among them, the compressive strength, splitting tensile strength, and flexural bearing capacity of the H-6 test block at 3 d age reached 88.1%, 82.0%, and 77.5% of its 28 d strength, respectively. The PC increased by 7.3%, 20.6%, and 18.8%; the 3 intensity values of the H-6 test block at 7 d age reached 91.7%, 90.5%, and 87.2% of its own 28 d intensity, which was higher than that of PC at 7 d age, increasing by 3.3%, 18.8%, and 22.1%.

4. Calculation of Fiber Confounding Effect Coefficient

The hybrid effect between basalt fiber and polyacrylonitrile fiber is evaluated from the theoretical point of view of the fiber hybrid effect coefficient. The calculation of the fiber confounding effect coefficient also considers the role of every single-blended fiber, and the fiber confounding effect coefficient is calculated based on literature [23–25]; see the following equation:

$$\begin{cases} \alpha = \dfrac{S - \beta}{\beta}, \\ \beta = \sum S_i \varphi_i, \end{cases} \tag{3}$$

where α is the fiber mixing effect coefficient; S is the mechanical performance test result of the HFRC test block; S_i is the mechanical performance result of the single i-doped fiber test block; φ_i is the volume fraction of the single i-doped fiber.

Formula (3) is the fiber mixing coefficient calculated for single fiber mixed, so the test results of PC block are ignored here. When $\alpha > 0.5$, it will produce a positive effect relative to single fiber concrete, and when $\alpha < 0.5$, it will produce a negative effect. At the same time, combined with the analysis of the above test data, this section specifically calculates the fiber confounding coefficient of the HFRC test block cube compression and splitting tensile and bending resistance. The results are shown in Table 4; f_{cc} is the strength of the HFRC test block, and F_{ct} is the strength of the single fiber concrete test block corresponding to the same volume. It can be seen that the result of the fiber confounding effect coefficient is basically consistent with the comparison of the above test results. When $\alpha < 0.5$, the mechanical properties of HFRC test block are slightly weaker than those of single fiber concrete with equal volume rate, indicating that the fiber mixing effect is negative under the combination of the two

kinds of fibers at this time. When $\alpha > 0.5$, the performance of the HFRC test block is better than that of single fiber concrete; at this time, the fiber mixing effect under the combination of dosage is positive.

5. Conclusion

(1) The incorporation of fibers can significantly improve the mechanical properties of the concrete matrix such as splitting tensile and bending toughness, but, at the same time, it also reduces the compressive strength of the concrete matrix to a certain extent. When single doped basalt fiber, single doped polyacrylonitrile fiber, and fiber are mixed, the splitting tensile performance of concrete is up to 5.5%, 12.9%, and 18.6% higher than that of PC, respectively; the flexural peak value is up to 18.3%, 29.9%, and 34.8% higher than that of PC. The maximum toughness ratio is 2.5, 2.7, and 4.4, respectively; the compressive strength of the cube is increased by −12.9%, −5.6%, and 1.6%, respectively, compared with PC; the compressive strength of the axial center is increased by −3.9%, 2.8, and 1.3% compared with that of PC.

(2) The incorporation of fiber has little effect on the compressive elastic modulus of the concrete matrix. In the case of single and mixed fiber, the influence of the fiber on the compressive elastic modulus of the concrete matrix is between −4.1% and 1.3%. At the same time, fiber can also enhance the mechanical properties of early-age concrete such as compression, tension, and bending.

(3) Through the analysis results of the test data and the calculation results of the fiber mixing effect coefficient, within the fiber volume content range specified in this article, a good mixing effect is shown between basalt fiber and polyacrylonitrile fiber. Based on all the experimental data and calculation results, the optimal blending amounts of basalt and polyacrylonitrile fiber obtained in this paper are $V_B = 0.15\%$ and $V_P = 0.11\%$.

Data Availability

The data used to support this study are available from the corresponding author upon request.

Disclosure

A preprint has previously been published (https://www. researchgate.net/publication/342765161) [27].

Conflicts of Interest

The authors declare that they have no conflicts of interest.

Acknowledgments

References

[1] J. Li, Z. Wu, C. Shi, Q. Yuvan, and Z. Zhang, "Durability of ultra-high performance concrete–a review," *Construction and Building Materials*, vol. 255, Article ID 119296, 2020.

[2] Z. Zhang, X. Shao, and P. Zhu, "Direct tensile behaviors of steel-bar reinforced ultra-high performance fiber reinforced concrete: effects of steel fibers and steel rebars," *Construction and Building Materials*, vol. 243, Article ID 118054, 2020.

[3] Z. Wu, C. Shi, and K. H. Khayat, "Investigation of mechanical properties and shrinkage of ultra-high performance concrete: influence of steel fiber content and shape," *Composites Part B: Engineering*, vol. 174, Article ID 107021, 2019.

[4] G. B. Maranan, A. C. Manalo, B. Benmokrane, W. Karunasena, P. Mendis, and T. Q. Nguyen, "Flexural behavior of geopolymer-concrete beams longitudinally reinforced with GFRP and steel hybrid reinforcements," *Engineering Structures*, vol. 182, pp. 141–152, 2019.

[5] M. Singh, A. H. Sheikh, M. S. Mohamed Ali, P. Visintin, and M. C. Griffith, "Experimental and numerical study of the flexural behaviour of ultra-high performance fibre reinforced concrete beams," *Construction and Building Materials*, vol. 138, pp. 12–25, 2017.

[6] M. F. Al-Lebban, A. I. Khazaly, R. Shabbar, Q. A. Jabal, and L. A. R. Al Asadi, "Effect of polypropylene fibers on some mechanical properties of concrete and durability against freezing and thawing cycles," *Key Engineering Materials*, vol. 895, pp. 130–138, 2021.

[7] A. Abdelrahman, A. Wael, and F. Murad, "Structural performance and moment redistribution of basalt FRC continuous beams reinforced with basalt FRP bars," *Engineering Structures*, vol. 240, Article ID 112390, 2021.

[8] J. He, J. Shi, Y. Zhang et al., "Study on tensile stress-strain relationship of BFRC," *IOP Conference Series: Earth and Environmental Science*, vol. 643, no. 1, Article ID 012040, 2021.

[9] X.-F. Chen, C.-Q. Quan, and C.-J. Jiao, "Experimental study of chloride resistance of polypropylene fiber reinforced concrete with fly ash and modeling," *Materials*, vol. 14, no. 16, p. 4417, 2021.

[10] L. Yang, H. Xie, S. Fang, C. Huang, A. Yang, and Y. J. Chao, "Experimental study on mechanical properties and damage mechanism of basalt fiber reinforced concrete under uniaxial compression," *Structures*, vol. 31, pp. 330–340, 2021.

[11] Y. Aravind Sai and M. Anil Kumar, "Experimental study on mechanical properties of polypropylene fiber reinforced concrete with silica fume," *IOP Conference Series: Materials Science and Engineering*, vol. 1136, no. 1, Article ID 012020, 2021.

[12] K. Cui, L. Xu, X. Li et al., "Fatigue life analysis of polypropylene fiber reinforced concrete under axial constant-amplitude cyclic compression," *Journal of Cleaner Production*, vol. 319, Article ID 128610, 2021.

[13] S. Ashkan, N. Parisa, P. Ali Shadmani, M. M. Moein, H. Moez, and E. H. Vishki, "Prediction of mechanical properties of lightweight basalt fiber reinforced concrete containing silica fume and fly ash: experimental and numerical assessment," *Journal of Building Engineering*, vol. 32, Article ID 101732, 2020.

[14] H. Ahmad, M. Sheikh, Neaz, and N. S. Hadi Muhammad, "Behavior of GFRP bar-reinforced hollow-core polypropylene fiber and glass fiber concrete columns under axial compression," *Journal of Building Engineering*, vol. 44, Article ID 103245, 2021.

[15] M. Khan, M. Cao, and M. Ali, "Cracking behaviour and constitutive modeling of hybrid fibre reinforced concrete," *Journal of Building Engineering*, vol. 30, Article ID 101275, 2020.

[16] C. H. E. N. Qian, L. Xu, and F. Wu, "Experimental investigation on strength of steel- polypropylene hybrid fiber reinforced ultra high performance concrete," *Bulletin of the Chinese Ceramic Society*, vol. 39, no. 3, pp. 740–748, 2020.

[17] H. Wu, Z. Pei, and X. Yang, "Experiment on crack resistance of steel-polypropylene hybrid fiber reinforced concrete," *Journal of Huazhong University of Science and Technology (Nature Science Edition)*, vol. 48, no. 4, pp. 43–47, 2020.

[18] C. Yang, C. Huang, and Y. Che, "Mechanical properties and impermeability of hybrid fiber reinforced concrete," *Journal of Building Materials*, vol. 11, no. 1, pp. 89–93, 2008.

[19] H. Pan, "Experimental study on mechanical property of basalt fiber reinforced concrete," *Bullention of the Chinese Ceramic Society*, vol. 28, no. 5, pp. 955–959, 2009.

[20] J. He, J. Shi, Z. Wang et al., "Effect of hybrid effect on the mechanical properties of hybrid fiber reinforced concrete," *Fiber Reinforced Plastics/Composites*, vol. 9, pp. 26–32, 2016.

[21] Q. Fu, W. Xu, M. Bu, B. Guo, and D. Niu, "Effect and action mechanism of fibers on mechanical behavior of hybrid basalt-polypropylene fiber-reinforced concrete," *Structures*, vol. 34, no. 34, pp. 3596–3610, 2021.

[22] A. Krishna and S. R. M. Kaliyaperumal, "Effect of elevated temperature on strength and ductility of axially loaded hybrid fiber reinforced concrete columns," *Structures*, vol. 34, pp. 3548–3556, 2021.

[23] R. P. Borg, O. Baldacchino, and L. Ferrara, "Early age performance and mechanical characteristics of recycled PET fibre reinforced concrete," *Construction and Building Materials*, vol. 108, pp. 29–47, 2016.

[24] D. Shen, X. Liu, Q. Li, L. Sun, and W. Wang, "Early-age behavior and cracking resistance of high-strength concrete reinforced with Dramix 3D steel fiber," *Construction and Building Materials*, vol. 196, pp. 307–316, 2019.

[25] Z. Liu, W. Robert, F. Du et al., "A study on avalanches of early age basalt fiber reinforced concrete beams during flexure," *Journal of Cleaner Production*, vol. 279, Article ID 123695, 2021.

[26] H. Guo, L. Jiang, J. Tao, Y. Chen, Z. Zheng, and B. Jia, "Influence of a hybrid combination of steel and polypropylene fibers on concrete toughness," *Construction and Building Materials*, vol. 275, Article ID 122132, 2021.

[27] 2020 https://www.researchgate.net/publication/342765161_Study_on_mechanical_properties_and_optimum_fiber_content_for_basaltpolyacrylonitrile_hybrid_fiber_reinforced_concrete.

Research Article

Production and Optimization of Energy Rich Biofuel through Co-Pyrolysis by Utilizing Mixed Agricultural Residues and Mixed Waste Plastics

Chirag Vibhakar,[1] R. S. Sabeenian,[2] S. Kaliappan [ID],[3] Pandurang Y. Patil,[4] Pravin P. Patil,[5] P. Madhu [ID],[6] C. Sowmya Dhanalakshmi [ID],[7] and Habtewolde Ababu Birhanu [ID][8]

[1]*Electrical Engineering Department, Gujarat Power Engineering & Research Institute, Mehsana, Gujarat 382710, India*
[2]*Department of Electronics and Communication Engineering, Sona College of Technology, Salem, Tamil Nadu 636005, India*
[3]*Department of Mechanical Engineering, Velammal Institute of Technology, Chennai, Tamil Nadu 601204, India*
[4]*Department of Environmental Science, Ratnagiri Sub-Campus, University of Mumbai, Ratnagiri, Maharashtra 415639, India*
[5]*Department of Mechanical Engineering, Graphic Era Deemed to be University, Bell Road, Clement Town Dehradun, Uttarakhand 248002, India*
[6]*Department of Mechanical Engineering, Karpagam College of Engineering, Coimbatore, Tamil Nadu 641032, India*
[7]*Department of Mechanical Engineering, SNS College of Technology, Coimbatore, Tamil Nadu 641035, India*
[8]*Faculty of Mechanical Engineering, Arba Minch Institute of Technology, Arba Minch University, P.O. Box 21, Arba Minch, Ethiopia*

Correspondence should be addressed to Habtewolde Ababu Birhanu; habtewold.ababu@amu.edu.et

Two totally waste products, agricultural residues and mixed plastic wastes collected from domestic and industrial sectors, are used in this study for the recovery of energy rich biofuel and value-added chemicals. The copyrolysis experiments using fixed bed reactor are conducted in order to analyse the synergetic effects. The experimental works are carried out with different proportion of mixed plastics blended with agricultural residues. The reaction temperature and biomass-to-waste plastics ratio on product distributions are studied and addressed. The thermogravimetric analysis conducted at different temperatures clearly distinguished the pyrolysis behaviours of biomass and plastics. The positive synergistic effects defined as higher yield of volatiles compared to predicted yield for bio-oil were identified at particular mixing ratio. Both biomass wastes and plastic wastes show optimal performance of 60.42 wt% oil yield at 60% addition of waste plastics. The oil products obtained under favourable conditions have a higher heating value compared to the oil obtained from biomass pyrolysis. The GC-MS study confirmed that the interaction between biomass and plastics during copyrolysis resulted in decreased oxygenated contents in the oil products.

1. Introduction

The development of renewable energy by utilizing waste materials is a promising solution to fossil fuel depletion and global warming issues. It is predicted that coal stocks would be depleted by 2112 and crude oil reserves will be depleted by 2042; at the same time, the energy needed around the world is expected to increase by 56% by 2040 [1]. Utilization of

waste biomass for various purposes has been focused on by many researchers in the past three decades.

The use of agricultural biomass for fuel production is renewable and sustainable. Many literatures reported the use of various agricultural wastes for energy recovery. Lignin, cellulose, hemicelluloses, and a considerable amount of extractives are the primary components of biomass materials [2]. The wastes from agricultural fields are generally burnt in

the open air in the field itself due to their lower bulk density and low value. They are not seasonable and are abundant throughout the world. The agricultural residues generally refer to the remains of plants including pods, stems, and corn. Forest wastes, wood chips, and municipal solid waste are also the examples of biomass energy sources today [3]. The production of liquid fuels from agricultural wastes is recognized as an important renewable resource. The organic liquid from agricultural residues has better fuel properties with considerable heating value. Previously many authors have presented the use of agricultural residues for fuel production through thermochemical conversion processes including pyrolysis. The production of liquid products through pyrolysis is called pyrolysis oil. The properties and quantity of oil produced during pyrolysis depend on the feedstock composition.

With the introduction of plastics, their use extended to every corner of the world. Plastics are currently critical for sustaining a resource-efficient economy [4]. Because of their advantageous properties including lightweight and durability, the plastics are widely used around the world. However, these positive characteristics accelerated the accumulation of plastics in the environment with huge volume [5]. By 2015, around 6300 Mt of waste plastics was produced throughout the world and more than 80% was dumped in the natural environment. Plastic waste management is one of the critical challenges throughout the world due to lack of technology development. India's current waste biomass availability is estimated to reach more than 500 million metric tonnes per year. Biomass presently accounts for 32% of total primary energy consumption in the country. India produces a massive amount of waste plastics every year. However, only one-fourth of this is recycled due to lack of a functioning solid waste management system. In 2019-20, India generated an annual plastic waste of 3.46 Mt of plastic garbage, compared to 3.360 Mt in 2018-19 and 2.383 Mt in 2017-18. In terms of environmental concerns, land filling technique is not suitable and costly, as the by-products are extremely hazardous to both the environment and human health [6]. However, very poor degradability of plastics, on the other hand, generates substantial environmental issues and poses a significant challenge. In 2018, worldwide plastics output surpassed 359 Mt, with major contribution from China and Europian countries [7]. However, India produces 5.58 Mt of single-use plastics annually followed by Japan with 4.7 Mt. In India, only 60% of the plastic wastes are being recycled and the remaining 40% end with landfill. Improper plastic waste disposal can create structural deterioration. The chlorinated plastic can leach hazardous chemicals into the soil, which can seep into groundwater and harm both the environment and the ecosystem. Aside from landfilling, incineration is the possible alternate method to decompose plastic wastes. It is a commonly utilized and approved technique, since it can permanently degrade plastic waste with huge volumetric basis and thermal energy recovery, which may then be converted to electrical energy [8]. It also helps to regulate carbon emissions in the conventional energy industry by substituting alternative fuels [9]. Incineration of plastic wastes resulted in the release of very

dangerous toxic pollutants and dusts which are more harmful to all living organisms [10]. Aside from landfilling and incineration, utilization of these wastes for converting fuels is more popular in order to avoid resource wastage and contamination. When compared to traditional digestion, decomposition of plastic wastes thermally with controlled oxidation gives more benefits including lower emission and higher energy recovery [11]. Thermochemical conversion processes such as pyrolysis and gasification can offer effective recovery of medium-to-high grade fuels.

The intersection of environment protection, resource management, and energy recovery could be a viable research option to gain more popularity among the researchers. In recent years, combination of agricultural and plastic wastes for bio-oil production has gained much interest due to contribution of plastics towards increased heating value. Copyrolysis of biomass and plastics has grown in popularity as a viable alternative method for improving the quality of pyrolysis products. In comparison to traditional biomass and plastic pyrolysis, copyrolysis experiment has been gaining a lot of interest in the recent years. The synergistic impact of chemical interactions between diverse feedstocks plays a key part in copyrolysis process. However, the synergistic effect varies greatly depending on the nature of the raw materials. Because of their unique heating characteristics, microwave pyrolysis and solar pyrolysis have received a lot of attention in the recent years. Furthermore, the kinetics of biomass copyrolysis with plastics have recently been studied in order to gain a better understanding of the mechanism of the synergistic impact. Copyrolysis is the improved technique to produce high energy liquid products by interacting biomass and plastics. According to Johannes et al. [12], the interaction of feed materials and their product distributions are dependent on various parameters including mixing ratio, pyrolysis length, process temperature, and heating rate. Yang et al. [13] analysed the copyrolysis experiment on cedar wood and LDPE and observed a synergistic effect on oil production. The copyrolysis experiments on biomass and plastic waste have been studied extensively by many authors to analyse the process parameters on product yield and quality [4,14,15]. Oyedun et al. [16] and Hassan et al. [17] demonstrated that the type of biomass and amount of plastic during copyrolysis determine the quality of the yield products. Dewangan et al. conducted copyrolysis experiments on sugarcane bagasse combined with LDPE at the blend ratio of 1 : 1 and produced maximum oil fractions with calorific value of 40 MJ/kg. In another experiment carried out by Xue et al., the yield of oil was dependent on the reaction temperature [18]. According to Costa et al. [19], the copyrolysis of rice husk with polyethylene at a temperature range of 350–430°C enhanced the conversions of both biomass and polyethylene towards oil yield. Martinez et al. [20] investigated the effects of slow pyrolysis of biomass and polymers and discovered that the viscosity and acidity of the pyrolysis oil reduced; however, the energy content of the oil increased when compared to pyrolysis oil derived only from biomass. It has also been stated that when biomass and plastics are copyrolyzed, the production of oil is significantly larger than the total amount

of individual oil products obtained from biomass and plastics [21]. The study conducted by many researchers concluded that the copyrolysis of biomass and plastics has a stronger synergistic effect compared to individual pyrolysis [22–24].

This research is based on the pyrolysis of mixed agricultural residues combined with mixed waste plastics collected from domestic and industrial sectors, which is inspired by waste-to-energy concepts. Prior to the copyrolysis process, each of the components is pyrolyzed separately and their product distributions are found. After that, they are copyrolyzed by blending waste plastics with biomass materials at the ratios of 20%, 40%, 60%, and 80% by weight. The goal of this research is to increase the oil production while simultaneously improving the quality. The physical and chemical properties of oil produced under suitable conditions have been examined in order to find its feasibility as a source of energy and a chemical feedstock for a variety of applications.

2. Materials and Methods

2.1. Feedstock Preparation. The agricultural residues utilized for this study are a mixture of wheat straw, sugarcane bagasse, rice straw, corn stover, coconut shell, tobacco leaf, and sunflower shell collected from local field. The plastic materials utilized for this study are the collection of used food containers, beverage bottles, toys, door handles, pipes, and resilient bags made by low-density polyethylene, high-density polyethylene, polyvinyl chloride, polypropylene, and polystyrene. A ball mill is used to cut these feed materials and they are subsequently sieved to keep the size less than 1 mm. The feedstock materials are then subjected to analyses and the values are given in Table 1. Before conducting analysis, they are completely dried in an oven maintained at ±100°C for approximately 2 hours.

2.2. Pyrolysis Reactor Setup. The experiments are conducted in a lab scale fixed bed reactor. Conducting copyrolysis process in a fixed bed reactor is much better compared to

TABLE 1: Properties of feedstock materials in wt%.

Content	Biomass	Mixed plastics
Proximate analysis		
Volatile matter	73.4	90.9
Fixed carbon	15.0	0.4
Moisture content	6.4	0.5
Ash content	5.2	8.2
Ultimate analysis (ash-free basis)		
Carbon	47.1	80.1
Hydrogen	6.2	15.4
Nitrogen	2.1	2.6
Sulphur	0.8	0.4
Oxygen	43.8	1.5

% of O = 100-(C + H + N + S)%.

many available types of pyrolysis reactors [25]. The literature [26] contains a schematic diagram of the reactor system as well as its design specifications and further it is explained in this section. The reactor is comprised of a reactor bed with inner diameter of 100 mm and height of 150 mm. The reactor is heated using electrical resistance heater with ammeter and voltmeter set up. The temperature given to the reactor is controlled by the autotransformer. The temperature of the reactor is kept stable once it reaches the desired value by auto cut-off unit. The reactor is well insulated by insulating material to avoid unnecessary heat loss. It also consists of a condenser, oil collection system, and gas collection system. The condenser was cooled by circulating ice water maintained at a temperature of 5°C. The reaction was continued till no vapour was identified from the condenser. For this purpose, a minimum of 30 min is given to one complete reaction. The condenser's liquid products were collected in conical flasks attached to the condenser. The char at the end of the experimental runs is collected directly from the reactor. The oil fractions are collected through the condenser. After weighing char and oil fractions, the masses of the uncondensable gases are found by material balance method. The formula used to find the desired products from thermal pyrolysis of individual feedstocks is as follows:

$$\text{product yield (wt.\%)} = \frac{\text{desired product (oil or char or gas) in grams}}{\text{amount of feedstock in grams}} \times 100. \tag{1}$$

To find the synergetic effect, the experimental yields during copyrolysis process are compared with predicted yields. The formula used by Zhao et al. [27] is employed to find the predicted yield. The yields obtained from individual pyrolysis of mixed agricultural wastes and mixed plastic wastes are used to find the predicted yields shown in the following equation:

$$\text{predicted yield} = (x1 * Y1 + x2 * Y2), \tag{2}$$

where $Y1$ and $Y2$ are the yields of individual pyrolysis of agricultural residues and waste plastics, respectively. $X1$ and $X2$ are the mass ratios in the blended samples, respectively.

2.3. Analytical Instruments. The mass loss of the feedstock materials depends on the process temperature and heating rate and is investigated using a thermogravimetric analyser (TGA). The thermogravimetric analysis is performed with 10 mg of the sample hated at 10°C/min to explore and compare the degradation process of agricultural residues and waste plastics. Proximate analyses of the materials are done to find the volatile and semivolatile contents of the sample. Elementor Vario EL-III is employed to find the amounts of carbon, hydrogen, nitrogen, and sulphur in the feedstock samples. The oil content obtained at favourable condition is tested for its physical and chemical analysis. The

pH value of the oil is determined using a digital pH metre. The viscosity of the sample is determined using a viscometer (Brookfield Engineering Company). A Pensky-Martens closed-cup device is used to find the flash point of the sample. An electronic calorimetric thermometer (Parr-6772) is employed to determine the heating value of the oil. A GC-MS (Thermo MS DSQ II) is employed to assess the distribution of chemical compounds of the oil products. The equipment consists of a capillary column of 0.25 mm diameter, 30 m length, and 0.25 μm film thickness. For this analysis, the sample of 1 mL was injected at the temperature of 250°C. The oven temperature was set initially to 70°C for 3 minutes before being increased to 250°C at a rate of 10°C/min. The sample injection was done in split mode with the ratio of 20 : 1. With full scan mass spectra, the mass spectrometer was tuned to an ionising voltage of 70 eV. It was run at an interface temperature of 200°C. The analysis is carried out in the range of 50–650 m/z and the chemical components are identified by the use of mass spectrum libraries (NIST14.L).

2.4. Error Analysis. Before conducting the experiment, the Measurement System Analysis (MSA) was utilized to correct the uncertainty in the temperature measurement and electronic weighing machine. Thermocouple is used to measure the temperature of the reactor and weighing machine is used to measure the mass of the pyrolysis product yields. To ensure the repeatability, Test-Retest study was conducted under the same operating conditions. Prior to that, the thermocouple used in the reactor was calibrated in accordance with laboratory standards. The errors for thermocouple and electronic weighing machine were determined as 0.25% and 0.03%, respectively.

3. Results and Discussion

3.1. Thermogravimetric Analysis. Figures 1 and 2 depict TG and DTG curve for agricultural residues and mixed plastic wastes at various temperatures heated at 10°C/min. An increase in temperature for both materials increased the degradation rate. The tests are carried out in an inert atmospheric condition (Argon) and achieved to access the pyrolytic behaviour of the feedstock materials. According to thermogravimetric analysis of agricultural residues, the devolatilization process begins at 160°C and maximum weight loss appears between 350 and 475°C. Around 475 and 550°C, an abrupt change in the slope is recorded, resulting in lower weight loss. The major weight loss of around 70% in the biomass material happens between 250°C and 550°C. During this period, the volatile matters released from the material are maximum. The thermal overlapped degradation of the agricultural residues with major cellulose and hemicelluloses content is the primary cause of the highest mass loss at this temperature range [28]. According to TGA curve, the mixed plastics start to decompose at 330°C. This is due to the long chain polymeric structure of the plastic materials. The decomposition of plastic wastes is characterized at single stage, whereas for biomass materials it was achieved by three different stages [29]. The difference in decomposition stages for
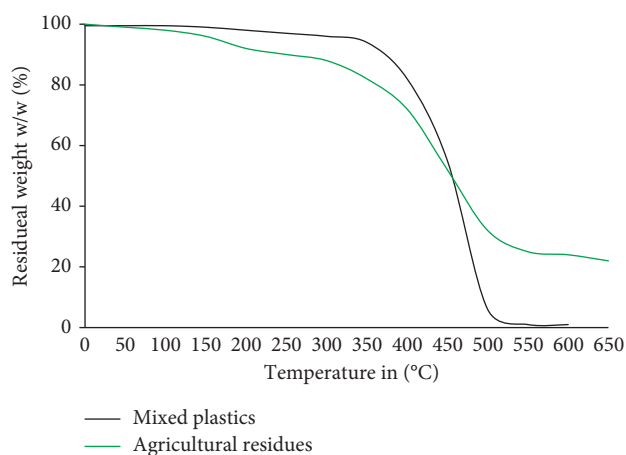
Figure 1: TG analysis for agricultural residues and mixed plastic waste.
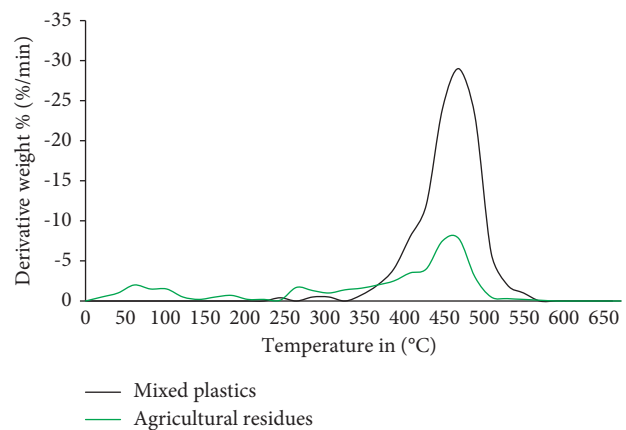
Figure 2: DTG agricultural residues for biomass and mixed plastics.

biomass materials is explained by their structures, since they are made up of cellulose and hemicellulose. From TGA curve, it is found that the degradation of mixed plastics took place in a single phase at higher temperature with limited temperature range. The mixed plastic loses its 97% of mass at temperatures ranging from 375 to 500°C and after that no decomposition was recorded. It can be seen from the data that both curves are overlapped at temperatures around 450°C based on maximum volatile loss, which shows these two feedstocks can be used as cofeed for this process. Compared to mixed plastics, for agricultural residues, some residues were found due to the presence of ash content [17]. The presence of ash content in feedstock is a crucial parameter for the yield of oil products. The ash in the feedstock will affect the quality of the entire pyrolysis products [30]. The amount of ash in the biomass sample has a direct impact on the production and composition of the pyrolysis products. During pyrolysis, ash particles generally extinguish the vapour conversion. In general, biomass with lower ash content is preferable for pyrolysis reactions. On the basis of the data, it can be clear that the appropriate reaction temperatures for both materials are around 450°C to 500°C.

3.2. Pyrolysis of Mixed Agricultural Residues.

Based on the TGA and DTG curve of the mixed agricultural biomass, the pyrolysis experiments are performed between the temperature limits of 300°C and 550°C to find the effect on product distributions. Figure 3 illustrates the yield of oil, char, and gas fractions related to reactor temperature. By applying temperature, the primary activation processes are initiated followed by subsequent vapour phase cracking reactions. According to this study, the product distribution from pyrolysis of mixed agricultural residues is temperature-dependent; however, pretreatments raised the initial degradation process and resulted in higher yields of condensable products. As the pyrolysis temperature was changed from 350 to 450°C, it became obvious that the yield of oil products reached its maximum value at 450°C. However, by increasing the temperature to 550°C, the yield of oil was decreased to 36.5 wt%. The yield of oil fractions reached its maximum at 450°C with a value of 39.8 wt% and it reduced with increasing the temperature. The reduced heat and mass transfer limitations at 450°C resulted in higher yields of oil products. It has been found that higher pyrolysis temperatures accompanied with more secondary reactions lead to more gaseous products with reduced oil products [31]. As shown in Figure 1, the char yield reduced from 41.2 wt% to 23.7 wt% as the final pyrolysis temperature increased from 350 to 550°C. The decrement in char production was observed due to enhanced primary decomposition of biomass or the secondary decomposition of the char residue at higher temperatures [32]. The secondary reactions of the char products at higher temperatures may also result in the yield of gas fractions, which is proportional to the increased pyrolysis temperature. For the temperature of 350°C, the gas yield was observed as 27.2 wt% and maximum of 39.8 wt% at 600°C. The changes in the physical properties of the pyrolysis products are mainly affected by the secondary reactions of tar vapours and the conversion time.

3.3. Pyrolysis of Mixed Plastic Wastes.

Figure 4 shows the pyrolysis behaviour of mixed plastics with respect to reactor temperature. The yield of char is nearly low for all temperatures. At the same time, the oil and gas yields are highly influenced by temperature. The pyrolysis of mixed plastics can be constructed by a narrow range of reactions due to simple monomeric structure. It has been proposed that almost all synthetic polymers disintegrate by a radical mechanism. The yield of char is varied from 18.9 wt% to 3.5 wt% when the temperature is raised from 350°C to 550°C. The lower degradation of plastic products at lower temperature yields higher char products. The yield of gas fraction is steadily increased with respect to increased temperature due to variation in stability of the polymer materials under different temperatures. For 350°C, the yield of gas is 19.9 wt% and the value is changed to 28.4 wt% for the final temperature of 550°C. Many other authors have also found similar findings [33,34]. According to the results, no volatiles were released from the reactor till it reached 300°C. These results were also predicted with TGA analysis. Beyond 300°C, the plastic waste generates condensable volatile contents. The oil products are
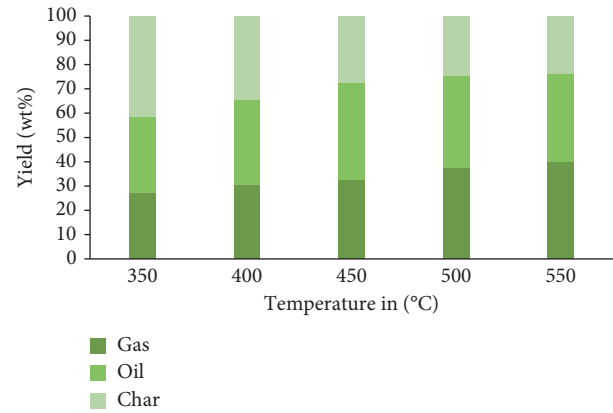
Figure 3: Pyrolysis of mixed agricultural residues performed at 1.0 mm particle size, at 20°C/min heating rate, and at different temperature.
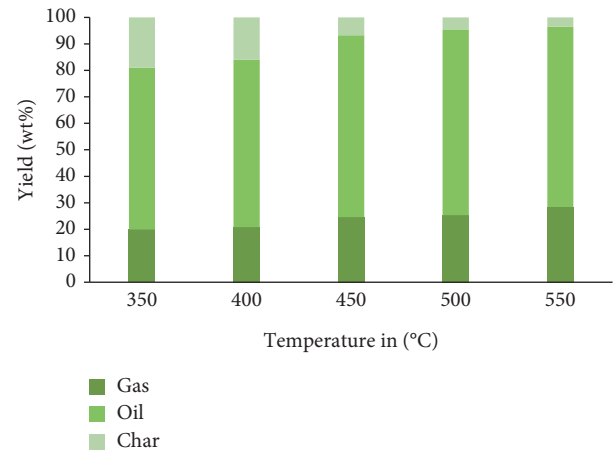
Figure 4: Pyrolysis of mixed plastic wastes performed at 1.0 mm particle size, at 20°C/min heating rate, and at different temperature.

gradually increased from 61.2 wt% to 68.1 wt% when the temperature is changed from 350°C to 550°C. The yield of oil attained maximum at 500°C with 70.2 wt%. The stability of hydrocarbons decreases as the temperature increases. So, at optimum temperature of 500°C, the C=C bonds are broken significantly, resulting in higher volatile product yields. Further increment up to 550°C decreased the oil production to 68.1 wt%. Generally the plastics had lower stability at higher temperature. The higher temperature breaks C=C bonds of the plastic wastes and releases more volatiles [35].

3.4. Copyrolysis Behaviour.

The oil, char, and gas distributions during the copyrolysis under different blend ratio are shown in Figure 5. There was no major difference observed between theoretical and experimental yields up to 40% blend of mixed plastics with agricultural residues. In order to get complete valorization, the holding time was kept constant for all experiments. In comparison to thermal pyrolysis of agricultural residues, the oil products obtained from copyrolysis were substantially higher. For instance, the oil obtained at 60% blend shows maximum compared to the
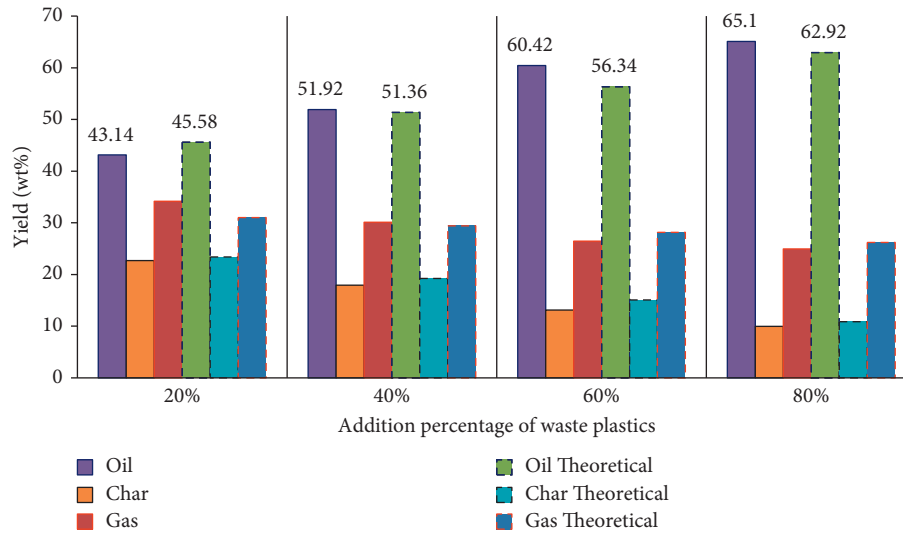
FIGURE 5: Assessment of synergistic effect.

TABLE 2: Physical properties of oil products obtained under different conditions.

Properties	Standard	Source			
		Biomass oil	Mixed plastic oil	Copyrolysis oil	Diesel [40]
Density in kg/m^3	ASTM D445	1025	930	1010	850
Viscosity in cSt	ASTM D4052	7.9	2.4	6.1	3.9
Flash point in °C	ASTM D92	140	95	105	57
Carbon in wt%	ASTM D5373	48.44	86.26	74.74	86.5
Hydrogen in wt%	ASTM D5373	9.0	10.94	9.6	13.2
Nitrogen in wt%	ASTM D5373	0.86	0.78	0.31	0.02
Sulphur in wt%	ASTM D5373	0.18	0.12	0.07	0.24
Oxygen in wt%	By difference	41.52	1.9	15.28	—
Heating value in MJ/kg	ASTM D445	20.9	43.12	35.3	43.6

% of O = 100-(C + H + N + S)%.

predicted value. The yield of oil is increased from 43.14 wt% to 65.1 wt% when the amount of plastics during reaction increases from 20% to 80%. In contrast, the char and gas yields are reduced from 22.7 wt% to 9.96 wt% and from 34.16 wt% to 24.94 wt%, respectively. At 60% addition of plastics, the result shows higher synergistic effect on oil production. At that condition, the predicted yield was only 56.34 wt% but experimentally the yield was recorded as 60.42 wt%. The result shows 7.24% increment compared to prediction. The radical secondary reactions are the main reason for the synergetic effect in this condition [36]. Furthermore, the presence of plastics on the reaction serves as a hydrogenation medium for lignocellulosic material, potentially reducing the polymerization and cross-linking activities ensuing major weight loss [37]. At 80% blend also the synergistic effects are identified for oil yield, but the increment was only 3.46%. As previously mentioned in the literature, during copyrolysis process, the plastics can act as a good hydrogen donor and will result in increased oil products. The higher hydrogen molecules present in the plastic materials will facilitate the conversion of oxygenated compounds into hydrocarbon molecules [38]. According to Onal et al., the radical interaction created by copyrolysis process favours the formation of higher oil products with no phase separation [39].

3.5. Characterization of Oil Products

3.5.1. Physical Analysis. Table 2 shows some of the basic physical characteristics of the oil fractions obtained under optimized conditions from pyrolysis and copyrolysis process. All of the analysis was measured by following ASTM protocol. The heating values of the oils are mostly determined by their hydrocarbon and oxygen content. The oxygen contents in the biomass oil, plastic oil, and copyrolysis oil are 41.52%, 1.9%, and 15.28%, respectively. The large number and concentration levels of oxygen compounds reduce the energy density to less than half those of ordinary fossil-derived fuel. The significant amount of the oxygenated species will cause instability during storage and transportation. The large decline in oxygen percent may explain the increase in heating value of the copyrolysis oil. Due to natural phase separation and radical interaction, the oxygen content of copyrolysis oil is significantly lower than that of other oils. The result shows that the copyrolysis process is an efficient approach for producing oil with higher heating value.

3.5.2. GC-MS Analysis. Gas chromatography-mass spectroscopy is a commonly used technology for the identification and quantification of compounds generated

TABLE 3: GC-MS analysis of the total pyrolysis oil.

Compound name	Molecular formula	Source		
		Biomass oil	Mixed plastic oil	Copyrolysis oil
3-Furaldehyde	$C_5H_4O_2$	0.41	—	0.24
Pyrogallol 1,3-dimethyl ether	$C_8H_{10}O_3$	2.04	—	—
3-Methyl-1-phenyl-1H-inden	$C_{16}H_{14}$	1.21	0.44	1.04
2,4-Dimethyl-1-heptene	C_9H_{18}	—	4.01	3.48
Phenol, 4-methyl-	C_7H_8O	0.52	—	—
9-Octadecenoic acid (z)-	$C_{18}H_{34}O_2$	2.33	—	—
1,3-Pentadiene, 2,4-dimethyl	C_7H_{12}	—	9.42	3.46
1-Hydroxy-2-methoxy-4-methylbenzene	$C_8H_{10}O_2$	3.34	—	—
Phenol	C_6H_5OH	8.41	—	6.03
Azulene	C_9H_8	—	10.42	7.44
Phenol, 2-methoxy-	$C_7H_8O_2$	7.34	—	2.42
Naphthalene, 2-methyl-	$C_{11}H_{10}$	—	1.42	—
1,2-Diphenylcyclopropane	$C_{15}H_{14}$	5.12	2.41	4.55
Phenol, 2,6-dimethyl-	$C_8H_{10}O$	4.32	—	1.04
2-Furancarboxaldehyde,-5-Methyl	$C_6H_6O_2$	1.10	—	—
Benzaldehyde, 4-hydroxy-3-methoxy	$C_8H_8O_3$	0.68	0.12	—
Phenol, 4-ethyl-2-methoxy-	$C_9H_{12}O_2$	0.32	—	0.98
Dibenzo[a,e]cyclooctene	$C_{16}H_{12}$	3.54	4.26	—
3-Methyl-1-phenyl-1H-indene	C16H14	—	2.68	1.04
Pyrene, 1-methyl-	$C_{17}H_{12}$	1.21	0.22	0.94
1,4-Dimethoxybenzene	$C_8H_{10}O_2$	3.27	—	—
Stearic acid, methyl ester	$C_{19}H_{38}O_2$	5.26	3.42	3.46
2-Isopropyl-2,5-dihydrofuran	$C_7H_{12}O$	3.46	—	0.55
Octadecanenitrile	$C_{18}H_{35}N$	6.44	—	0.94
1,2-benzendiol	$C_6H_6O_2$	5.05	—	—
Trimethylamine	C_3H_9N	4.21	0.85	3.45
1-Ethynyl-1,2,3,4-tetrahydro-a´-carboline	$C_{13}H_{12}N_2$	—	3.01	2.88
5-Hydroxymethylfurfural	$C_6H_6O_3$	0.24	—	—
Acetol	$C_3H_6O_2$	5.48	—	1.46
Acetic acid	$C_2H_4O_2$	16.42	—	6.79
3-Undecene, (Z)-	$C_{11}H_{22}$	—	3.49	—
Tetradecane	$C_{14}H_{30}$	—	4.47	—
Furfural	$C_5H_4O_2$	1.72	—	—
Butyholachone	$C_4H_8O_4$	3.77	0.49	2.07
2,5-Pyrrolidinedione, 1-methyl	$C_5H_7NO_2$	0.44	—	—
2-Methoxy tetrahydro furane	$C_5H_{10}O_2$	0.97	0.10	0.12
4-Ethyl-2-methoxy phenol	$C_9H_{12}O_2$	1.92	—	—
Ethisterone	$C_{21}H_{28}O_2$	—	6.42	1.46

during pyrolysis. The analysis was performed on the oil fractions acquired under optimized conditions. The NIST library and the compound probability percentage are used to trace the GC-MS compounds in the oil samples. The identified chemical components in the raw biomass pyrolysis are mostly the oxygenated contents and the plastic oil has majority of aliphatic hydrocarbons. Table 3 shows the presence of various chemical components in the pyrolysis and copyrolysis oil. The decreased oxygenated components in mixed plastic oil enhance the stability of the oil. The acid contents present in the biomass pyrolysis oil resulted from the decomposition of hemicellulose in the biomass materials. On the other side, decomposition of lignin is the primary reason for the presence of phenolic compounds in the biomass derived oil. The components of the oil contain the mixture of alkane, alkene, and alkyl group compounds with oxygenated elements.

4. Conclusion

This study found that pyrolysis of mixed agricultural residues combined with mixed plastic wastes has the potential options for the production of high-grade pyrolysis oil with a higher oil yield of 60.42 wt% at 60% blend of waste plastics. The yield of pyrolysis oil was greatly affected by the reactor temperature. It is the most significant parameter to valorize the feedstock. The physical characteristics of the oil acquired under copyrolysis process have higher heating value with reduced oxygen content. The synergistic impacts of copyrolysis process were investigated in terms of the pyrolysis process and its product yield. In comparison to theoretical data, synergistic effects occurred at 60% plastic blend showing 7.24% higher oil yield than other blend proportions. Rather than creating cross reaction products, these synergistic effects were discovered by identifying the composition of chemicals in copyrolysis oil. The copyrolysis oil obtained

from mixed agricultural residues and mixed plastics was identified as a biofuel candidate with heating value of 35.3 MJ/kg, which is higher compared to biomass pyrolysis oil. The higher heating value represents that it can be used directly as furnace oil for boiler and can be upgraded to be used as a fuel for IC engines. The report received by GC-MS confirmed the relations between biomass and plastics throughout the copyrolysis process resulting in decreased oxygenated products. Further study is possible to analyse the reaction kinetics and applications to get benefits in waste treatment and utilization.

Nomenclature

ASTM: American Society for Testing and Materials
DTG: Derivative thermogravimetry
GC-MS: Gas chromatography-mass spectrometry
LDPE: Low-density polyethylene
TGA: Thermogravimetric analysis
X_1:   Mass ratio of agricultural residues
X_2:   Mass ratio of waste plastics
Y_1:   Pyrolysis yield of agricultural residues
Y_2:   Pyrolysis yield of waste plastics.

Data Availability

The data used to support the findings of this study are included within the article.

Conflicts of Interest

The authors declare that there are no conflicts of interest regarding the publication of this article.

References

[1] A. Dewangan, D. Pradhan, and R. K. Singh, "Co-pyrolysis of sugarcane bagasse and low-density polyethylene: influence of plastic on pyrolysis product yield," *Fuel*, vol. 185, pp. 508–516, 2016.

[2] K. P. Shadangi and K. Mohanty, "Co-pyrolysis of Karanja and Niger seeds with waste polystyrene to produce liquid fuel," *Fuel*, vol. 153, pp. 492–498, 2015.

[3] Y. He, W. Qian, J. Wang, Y. Xiong, P. Song, and R. Wang, "High value-added reutilization approach for waste biomass materials," *Transactions of the Chinese Society of Agricultural Engineering*, vol. 32, no. 15, pp. 1–8, 2016.

[4] S. Papuga, P. Gvero, and L. Vukic, "Temperature and time influence on the waste plastics pyrolysis in the fixed bed reactor," *Thermal Science*, vol. 20, no. 2, pp. 731–741, 2016.

[5] R. Geyer, J. R. Jambeck, and K. L. Law, "Production, use, and fate of all plastics ever made," *Science Advances*, vol. 3, no. 7, Article ID e1700782, 2017.

[6] D. Hoornweg, P. Bhada-Tata, and C. Kennedy, "Environment: waste production must peak this century," *Nature*, vol. 502, no. 7473, pp. 615–617, 2013.

[7] Plastics Europe, "An Analysis of European Plastics Production," *Demand and Waste Data*, Plastics Europe: Association of plastic manufacturers, brussels, Belgium, p. 8, 2015, http://www.plasticseurope.org/Document/plastics---the-facts-2015.aspx?Page=DOCUMENT&FolID=2.

[8] R. H. J. M. Gradus, P. H. L. Nillesen, E. Dijkgraaf, and R. J. Van Koppen, "A cost-effectiveness analysis for incineration or recycling of Dutch household plastic waste," *Ecological Economics*, vol. 135, pp. 22–28, 2017.

[9] R. Ravi, S. Pachamuthu, and P. Kasinathan, "Computational and experimental investigation on effective utilization of waste heat from diesel engine exhaust using a fin protracted heat exchanger," *Energy*, vol. 200, Article ID 117489, 2020.

[10] N. Ágnes and K. U. T. I. Rajmund, "The environmental impact of plastic waste incineration," *AARMS–Academic and Applied Research in Military and Public Management Science*, vol. 15, no. 3, pp. 231–237, 2016.

[11] C. S. Dhanalakshmi and P. Madhu, "Recycling of wood bark of Azadirachta indica for bio-oil and chemicals by flash pyrolysis," *Indian Journal of Ecology*, vol. 46, no. 2, pp. 347–353, 2019.

[12] I. Johannes, L. Tiikma, and H. Luik, "Synergy in co-pyrolysis of oil shale and pine sawdust in autoclaves," *Journal of Analytical and Applied Pyrolysis*, vol. 104, pp. 341–352, 2013.

[13] J. Yang, J. Rizkiana, W. B. Widayatno et al., "Fast co-pyrolysis of low density polyethylene and biomass residue for oil production," *Energy Conversion and Management*, vol. 120, pp. 422–429, 2016.

[14] R. Ravi and S. Pachamuthu, "Experimental investigation on innovatory waste heat recovery system impacts on DIESEL engine exhaust emissions," *Energy Sources, Part A: Recovery, Utilization, and Environmental Effects*, vol. 43, no. 24, pp. 1–24, 2020.

[15] A. Ephraim, D. Pham Minh, D. Lebonnois, C. Peregrina, P. Sharrock, and A. Nzihou, "Co-pyrolysis of wood and plastics: influence of plastic type and content on product yield, gas composition and quality," *Fuel*, vol. 231, pp. 110–117, 2018.

[16] A. O. Oyedun, C. Z. Tee, S. Hanson, and C. W. Hui, "Thermogravimetric analysis of the pyrolysis characteristics and kinetics of plastics and biomass blends," *Fuel Processing Technology*, vol. 128, pp. 471–481, 2014.

[17] H. Hassan, B. H. Hameed, and J. K. Lim, "Co-pyrolysis of sugarcane bagasse and waste high-density polyethylene: synergistic effect and product distributions," *Energy*, vol. 191, Article ID 116545, 2020.

[18] Y. Xue, S. Zhou, R. C. Brown, A. Kelkar, and X. Bai, "Fast pyrolysis of biomass and waste plastic in a fluidized bed reactor," *Fuel*, vol. 156, pp. 40–46, 2015.

[19] P. Costa, F. Pinto, M. Miranda, and R. N. André, "Study of the experimental conditions of the co-pyrolysis of rice husk and plastic wastes," *Chemical Engineering Transactions*, vol. 39, pp. 1639–1644, 2014.

[20] J. D. Martínez, A. Veses, A. M. Mastral et al., "Co-pyrolysis of biomass with waste tyres: upgrading of liquid bio-fuel," *Fuel Processing Technology*, vol. 119, pp. 263–271, 2014.

[21] M. Brebu, S. Ucar, C. Vasile, and J. Yanik, "Co-pyrolysis of pine cone with synthetic polymers," *Fuel*, vol. 89, no. 8, pp. 1911–1918, 2010.

[22] M. Sajdak and R. Muzyka, "Use of plastic waste as a fuel in the co-pyrolysis of biomass. Part I: the effect of the addition of plastic waste on the process and products," *Journal of Analytical and Applied Pyrolysis*, vol. 107, pp. 267–275, 2014.

[23] M. Sajdak, R. Muzyka, J. Hrabak, and K. Słowik, "Use of plastic waste as a fuel in the co-pyrolysis of biomass," *Journal of Analytical and Applied Pyrolysis*, vol. 112, pp. 298–305, 2015.

[24] S. S. Mohapatra and R. K. Singh, "Production and characterization of the maximum liquid product obtained

from co-pyrolysis of sugarcane bagasse and thermocol waste," *Cellulose*, vol. 28, no. 7, pp. 4223–4239, 2021.

[25] J. Fei, J. Zhang, F. Wang, and J. Wang, "Synergistic effects on co-pyrolysis of lignite and high-sulfur swelling coal," *Journal of Analytical and Applied Pyrolysis*, vol. 95, pp. 61–67, 2012.

[26] C. Sowmya Dhanalakshmi and P. Madhu, "Utilization possibilities of Albizia amara as a source of biomass energy for bio-oil in pyrolysis process," *Energy Sources, Part A: Recovery, Utilization, and Environmental Effects*, vol. 41, no. 15, pp. 1908–1919, 2019.

[27] Y. Zhao, X. Yang, Z. Fu, R. Li, and Y. Wu, "Synergistic effect of catalytic co-pyrolysis of cellulose and polyethylene over HZSM-5," *Journal of Thermal Analysis and Calorimetry*, vol. 140, no. 1, pp. 363–371, 2020.

[28] H. Shafaghat, H. W. Lee, Y. F. Tsang et al., "In-situ and ex-situ catalytic pyrolysis/co-pyrolysis of empty fruit bunches using mesostructured aluminosilicate catalysts," *Chemical Engineering Journal*, vol. 366, pp. 330–338, 2019.

[29] V. A. Alvarez and A. Vázquez, "Thermal degradation of cellulose derivatives/starch blends and sisal fibre bio-composites," *Polymer Degradation and Stability*, vol. 84, no. 1, pp. 13–21, 2004.

[30] A. Trubetskaya, M. T. Timko, and K. Umeki, "Prediction of fast pyrolysis products yields using lignocellulosic compounds and ash contents," *Applied Energy*, vol. 257, Article ID 113897, 2020.

[31] P. T. Williams and A. R. Reed, "Pre-formed activated carbon matting derived from the pyrolysis of biomass natural fibre textile waste," *Journal of Analytical and Applied Pyrolysis*, vol. 70, no. 2, pp. 563–577, 2003.

[32] İ. Demiral and E. A. Ayan, "Pyrolysis of grape bagasse: effect of pyrolysis conditions on the product yields and characterization of the liquid product," *Bioresource Technology*, vol. 102, no. 4, pp. 3946–3951, 2011.

[33] M. del Remedio Hernández, A. Gómez, Á. N. García, J. Agulló, and A. Marcilla, "Effect of the temperature in the nature and extension of the primary and secondary reactions in the thermal and HZSM-5 catalytic pyrolysis of HDPE," *Applied Catalysis A: General*, vol. 317, no. 2, pp. 183–194, 2007.

[34] A. López, I. De Marco, B. M. Caballero, M. F. Laresgoiti, and A. Adrados, "Influence of time and temperature on pyrolysis of plastic wastes in a semi-batch reactor," *Chemical Engineering Journal*, vol. 173, no. 1, pp. 62–71, 2011.

[35] K. G. Burra and A. K. Gupta, "Kinetics of synergistic effects in co-pyrolysis of biomass with plastic wastes," *Applied Energy*, vol. 220, pp. 408–418, 2018.

[36] G. Özsin and A. E. Pütün, "A comparative study on co-pyrolysis of lignocellulosic biomass with polyethylene terephthalate, polystyrene, and polyvinyl chloride: synergistic effects and product characteristics," *Journal of Cleaner Production*, vol. 205, pp. 1127–1138, 2018.

[37] H. Yuan, H. Fan, R. Shan, M. He, J. Gu, and Y. Chen, "Study of synergistic effects during co-pyrolysis of cellulose and high-density polyethylene at various ratios," *Energy Conversion and Management*, vol. 157, pp. 517–526, 2018.

[38] L. Zhou, Y. Wang, Q. Huang, and J. Cai, "Thermogravimetric characteristics and kinetic of plastic and biomass blends co-pyrolysis," *Fuel Processing Technology*, vol. 87, no. 11, pp. 963–969, 2006.

[39] E. Önal, B. B. Uzun, and A. E. Pütün, "Bio-oil production via co-pyrolysis of almond shell as biomass and high density polyethylene," *Energy Conversion and Management*, vol. 78, pp. 704–710, 2014.

[40] D. Raguraman, A. Kumar, S. Prasanna Raj Yadav et al., "Performance and emission characteristics of pyrolysis oil obtained from neem de Oiled cake and waste polystyrene in a compression ignition engine," *Advances in Materials Science and Engineering*, vol. 2021, Article ID 3728852, 2021.

Research Article

Performance and Emission Characteristics of Pyrolysis Oil Obtained from Neem de Oiled Cake and Waste Polystyrene in a Compression Ignition Engine

D. Raguraman,[1] **Aditya Kumar,**[2] **S. Prasanna Raj Yadav,**[3] **Pandurang Y. Patil,**[4]
J. Samson Isaac,[5] **C. Sowmya Dhanalakshmi** ⓘ**,**[6] **P. Madhu** ⓘ**,**[7]
and J. Isaac JoshuaRamesh Lalvani ⓘ[8]

[1]*School of Mechanical Engineering, Bharath Institute of Higher Education and Research, Chennai, Tamil Nadu 600126, India*
[2]*Department of Mechanical Engineering, Netaji Subhas University of Technology, Dwarka, New Delhi 110078, India*
[3]*Department of Mechanical Engineering, Easwari Engineering College, Chennai, Tamil Nadu 600089, India*
[4]*Department of Environmental Science, Ratnagiri Sub-Campus, University of Mumbai, Ratnagiri, Maharashtra 415639, India*
[5]*Department of Biomedical Engineering, Karunya Institute of Technology and Sciences, Coimbatore, Tamil Nadu 641114, India*
[6]*Department of Mechanical Engineering, SNS College of Technology, Coimbatore, Tamil Nadu 641035, India*
[7]*Department of Mechanical Engineering, Karpagam College of Engineering, Coimbatore, Tamil Nadu 641032, India*
[8]*Faculty of Mechanical Engineering, Arba Minch Institute of Technology, Arba Minch University, P.O. Box 21,*
 Arba Minch, Ethiopia

Correspondence should be addressed to J. Isaac JoshuaRamesh Lalvani; isaac.jrl@amu.edu.et

Plastic is a resilient, chemically inert, lightweight, and low-cost material. It sticks around in the environment for more than hundred years, threatening nature and spreading toxins. The current study deals with the use of waste polymeric materials and de oiled cake for the production of liquid oil and its blend on the performance and emission characteristics of diesel engine. The tests were conducted in an engine fuelled with diesel and four distinct blends such as 5% (B5), 10% (B10), 15% (B15), and 20% (B20), respectively. The liquid oil was produced by co-pyrolysis of neem de oiled cake (NDC) and waste polystyrene (WPS) in 1 : 2 blend ratio. The raw pyrolysis oil and its different blends were tested for their physical and chemical characteristics in order to find their suitability. Brake power (BP), brake thermal efficiency (BTE), brake-specific fuel consumption (BSFC), emissions of carbon monoxide (CO), hydrocarbon (HC), and nitrogen oxide (NOx) are used to assess the performance of the engine. The experimental results reveal that BTE at all blends is lower than diesel at all loads and the BSFC increases with increasing blend ratio and falls with increasing engine load. At higher loads, the deviation of performance and emission values from baseline diesel up to B10 is very small. It is found from the results that the liquid oil derived from NDC and WPS up to 10% blend will be the promising additive for fossil fuels.

1. Introduction

Many countries in the world have launched zero plastic waste initiative, which seeks to boost collection of wastes and recovery of value added products and eliminate plastic contamination throughout the plastics lifecycle. The increase in the global population and need for polymeric materials in all sectors led to a rise in the gathering of waste polymer materials in the environment. Waste management policies and increased fuel cost led the researchers to find possible substitute to meet increased energy demand by replacing fossil fuels [1]. Increased air, water, and soil pollutions, change of climate, and global warming are most likely to blame for the continued degradation of the global ecosystem [2]. The burning of fossil fuels in all industrial sectors and transport vehicles are the primary source of these harmful

pollutants. The increased thermal efficiency and outstanding drivability of the diesel engine have a propensity to use in transport sector as well as power plants [3]. By 2040, the rapid development of automobiles keeps continued fuel consumption all over the world which consumes around 25% of global energy, and it is found to increase more than 160 quadrillion BTU [4]. The global economy is also increasing based on the population at a rate of 3.4% per year and anticipated to climb from 7.5 to 9 billion. The energy need for transportation sector is predicted to increase by 30% [5]. It is also estimated that, by 2050, 27% of the world's transportation fuel will be derived from biomass and waste resources [6]. Many researchers have previously conducted engine performance analysis using various biodiesel and different engine modification systems. Soudagar et al. conducted engine analysis using different blends of cottonseed oil biodiesel with various percentages of octanol additives along with multiwalled carbon nanotubes. The study showed that 20% blend of biodiesel with 5%, 10%, and 15% octanol consumes lower fuel. The addition of nanoparticles in this experiment stabilized fuel consumption and increased the BTE of the engine [7]. Karuppan et al. conducted the experiment on homogenous charge compression ignition engine fuelled with chicken fat oil biodiesel. Based on the analysis, the engine operated with blended biodiesel offers high peak pressure and higher heat release rate than neat diesel fuel [8]. Regarding emission, Verma et al. conducted experimental investigations on diesel engine operated with roselle biodiesel-diesel blend. The blend up to 20% shows 18.89% reduction in smoke compared to diesel [9]. In order to enhance the performance of the engine, Vinukumar et al. conducted the engine experiment with the addition of coconut shell nanoparticles with diesel and biodiesel blend. Without changing any modification, the engine shows better performance with reduced NOx emission [10]. Similarly, the engine operated with various blends of mahua biodiesel and sardine fish oil biodiesel showed better performance compared to diesel fuel [11, 12].

Waste plastics are a form of waste that is abundant and may be utilised for generating electricity. Plastic manufacturing has increased dramatically for the past three decades, reaching more than 130 million tonnes per year [13]. Synthetic polymers such as polyethylene, polypropylene, polyvinyl chloride, and polystyrene have seen a substantial increase in use for the last twenty years. These materials are long-lasting and light-weight used for households and industrial purposes but disposing of these wastes is the serious issue by considering sustainable environment. The old and traditional plastic waste disposal method followed in many parts of the world is land filing. But it should not be disposed since these plastics are disintegrated for up to 1,000 years. As a result, a proper recycling of these wastes should be identified by various recycling processes such as mechanical, chemical, biological, and thermal recycling. Biofuels made from waste materials are garnering a lot of attention and interest because of their numerous benefits and the availability of their feedstocks. Many researchers have focused on biofuel generation by utilizing agricultural residues and waste plastics through

pyrolysis, hydropyrolysis, and catalytic cracking [14]. The type employed for the study is based on the type of feedstock material, precursor, and final form of fuel. The benefits of the pyrolysis technique compared to other techniques for biofuel production have been highlighted by several studies [15, 16]. In pyrolysis, the waste solid particles are transformed into liquid oil by applying heat up to 750°C with maximum liquid yield of 60–70%. The bio-oil produced from biomass materials on the other hand has unstable fuel characteristics compared to mineral oil. The water content in the bio-oil is the main drawback that decreases the energy content of the fuel [17]. Co-pyrolysis process of biomass with synthetic waste polymer may be explored to enhance the stability of the produced oil. Polymers in the co-pyrolysis process act as hydrogen donors with less hydrogen containing lignocellulosic materials such as biomass. The plastic wastes are generally having higher hydrogen molecules that enhance the stability of the liquid product when pyrolyzed with biomass materials compared to thermal biomass pyrolysis [18]. From the data obtained from previous studies, this process yields high-quality liquid products due to synergetic effects [19–22] and can be utilised in internal combustion engines.

During biodiesel synthesis process, a bulk quantity (~40%) of solid waste is produced from the oil feedstocks. For example, neem seed is a potential feedstock producing neem seed oil. It is nonedible seed that contains up to 60% oil kernel and 40% neem de oiled cake (NDC) [23, 24]. It is an industrial by-product, and it has received higher interest since it is available abundantly through many oil industries. However, the major disadvantage with this feedstock is the presence of excess oxygen. Therefore, utilization of liquid oil obtained from thermal pyrolysis of raw NDC would result in engine damage as well as the emission of CO, HC, and NOx. By considering the above drawbacks, co-pyrolysis of NDC with waste polymeric material is selected for making high-grade liquid oil. Among all types of plastic wastes, polystyrene has attracted the attention of many researchers due to higher volatiles and recovery rate [25]. At 2016, more than 54 million kg of expanded polystyrene wastes were recycled into various forms. Normally, the waste recycling stations do not accept expanded waste polystyrenes due to their higher carbon footprints and higher processing charge [26]. On the other hand, it is a low-cost raw material for the production of fuels and valuable chemicals. These wastes produce less gaseous products with less insoluble organic materials, minimising the environmental effect caused by waste plastics [27]. These are the main reasons to choose waste polystyrene for oil extraction purpose. Polystyrene or waste thermocol is used as a co-feed with biomass pyrolysis yielding high-quality liquid oil due to a synergistic effect [28]. For the past two decades, the researchers have hardly studied the behaviour of the various engines operated with co-pyrolysis oil as a fuel. Previously, Mohapatra et al. [4] conducted various analyses on IC engine using different blends of liquid oil derived from sugarcane bagasse and thermocol wastes. When compared to neat diesel oil, the authors found that 5% blend has improved performance and emissions characteristics. Pradhan et al. [29] studied engine performance

analysis of diesel blended with pyrolysis oil obtained from the mixture of mahua seeds and waste thermocol, and they reported some decrement in BTE and NOx with increased blend.

The present work in this series also focuses on the assessment of performance and emission characteristics of diesel engine using co-pyrolysis oil produced from NDC and WT. The engine was investigated by using four different blends of neat diesel and co-pyrolysis oil. The primary objective is to explore the use of waste polymeric materials and de oiled cake for the production of liquid oil and its blend on diesel engine performance. There are no literatures that focused on engine studies using different biodiesel blends obtained from nonedible seed cake and waste polystyrene.

2. Materials and Methods

2.1. Materials. Neem de oiled cake used for this study is collected from local oil industries in Coimbatore, India. It is rich in protein, with higher nutritional value. After oil extraction, these cakes are processed for making fertilizers and sometimes they are used for cooking purpose. The waste polystyrene used for packing electronic goods was also collected from local scrap vendors. The two feed materials used for this study are complete industrial waste products. The NDC was dried in open atmosphere for more than 15 days and then oven dried at approximately 60°C for 12 hours. The waste polystyrene collected for this study is 95% air with high volume. In order to reduce its volume, the material was shredded and then dried at 100°C. Figure 1 shows the photographic views of the feedstock materials used for this study.

2.2. Characterization. Various characterizations of the selected materials are done to find the suitability for pyrolysis process as displayed in Table 1. The analysis was carried out by air dry basis. All the analyses are carried out by following ASTM standard test procedures reported in Table 1. Parr-6772 bomb calorimeter is employed to find the calorific value of the feedstocks, oil, and tested fuel. After extracting co-pyrolysis oil, the various properties such as density, kinematic viscosity, flash point, fire point, cetane number, carbon residue, and calorific value are analysed.

2.3. Pyrolyzer Setup. The co-pyrolysis experiments were conducted to extract pyrolysis oil by utilizing lab-scale fixed bed reactor. The reactor (diameter: 100 mm, length: 150 mm) holds around 50 g of feed materials blended in the ratio of 1 : 2 (NDC : WPS) per run. The experiments were repeated till adequate amount of oil was extracted for this study under the same operating conditions. Required amount of heat is applied to the reactor via 2000 W electrical heater and controlled by autotransformer which controls the heat input rate. The reactor is maintained at 550°C which is measured by two K type thermocouples positioned at two different points. The evolved gases passed through a condenser to convert condensable volatiles into liquid oil. The

temperature of the water in condenser circuit is maintained less than 5°C.

2.4. Engine Setup. The engine setup used for this study is Kirloskar make TV1 single-cylinder, four-stroke compression ignition type. The engine is attached with various pieces of equipment to measure crank angle, pressure, airflow, temperature, load, and fuel flow. The setup is also configured with a manometer, fuel flow measurement system, air flow measurement system, and process indicator. The engine is generating a rated output power of 5.20 kW. The swept volume of the engine is found as 661.45 cc. Table 2 contains the engine's basic specifications. The gas emitted from the engine is allowed through AVL type multigas analyzer to compute the level of CO, HC, and NOx. The tests are carried out on different blends of pyrolysis oil and diesel. Figure 2 shows the block diagram of the engine test-rig.

2.5. Characterization of Co-Pyrolysis Oil and Blends. The pyrolysis and its blends with neat diesel, namely, B5, B10, B15, and B20, are analysed for its basic fuel properties such as viscosity, density flash point, fire point, cetane number, carbon residue, and calorific value, and their values are exhibited in Table 3. All the properties are measured in accordance with ASTM standards. FTIR spectroscopy is also employed to examine the functional groups present in the co-pyrolysis oil. The FTIR spectrum data was taken in the range 400–4000 cm^{-1} with 4 cm^{-1} resolution.

3. Results and Discussion

3.1. Pyrolysis and Its Product Characterization. During co-pyrolysis experiments, a maximum of 73.4 wt% of pyrolysis oil yield was obtained using feed ratio of 1 : 2 (NDC : WPS) at 550°C reactor temperature. Table 4 describes the basic properties of co-pyrolysis oil and its blends along with diesel. The basic properties of diesel were somewhat changed when it was blended with co-pyrolysis oil. During blends, the density and kinematic viscosity are observed in increased trends. The flash and fire points of the blended fuels are increased up to B10; after that, the values are decreased till B20. The cetane number of the raw co-pyrolysis oil is very low compared to diesel, and the reductions in cetane number with respect to higher blends are ascribed to the presence of polystyrene contents [30]. The calorific value of the blended fuel was directly impacted by the presence of oxygen in the blend [31].

3.2. FTIR Analysis of Co-Pyrolysis Oil. The FTIR spectrum of the co-pyrolysis oil is shown in Figure 3. The oil was found with the combination of various aliphatic hydrocarbons with the absorption peaks of 3100.66 cm^{-1} and 2833.55 cm^{-1}. The oxygenated compounds in the oil were shown by the appearance of C=O stretching vibration at 1738.13 cm^{-1}, also showing the existence of carbonyl group. The alcohols and esters compound in the oil was detected by O-H stretching vibrations at 3619.9 cm^{-1} and C-O stretching vibrations at

(a)   (b)

FIGURE 1: Feedstock material for co-pyrolysis oil. (a) Neem de oiled cake. (b) Waste polystyrene.

TABLE 1: Feedstock characteristics.

Material	Volatile matter	Fixed carbon	Moisture	Ash	Carbon	Hydrogen	Nitrogen	Sulphur	Oxygen	Calorific value
NDC	78.25	8.91	7.52	5.32	51.62	5.27	3.1	0.31	39.7	17.92
WPS	98.18	0.49	0.24	1.09	89.2	8.82	0.01	—	1.97	40.49
Standard	ASTM D3175	By difference	ASTM D3173	ASTM D3174	ASTM D5373				By difference	ASTM D445

TABLE 2: Engine setup and specification.

Make and model	Kirloskar TV 1
Type	Four strokes, compression ignition, water cooled
Compression ratio	17.5 : 1
No. of cylinders	Single
Rated power	5.2 kW
Engine capacity	661 cc
Bore	87.5 mm
Rated speed	1500 rpm
Stroke	110 mm
Injection pressure	210 bar
Dynamometer	Eddy current
Start of injection	23°bTDC

1177.37 cm^{-1}. The N-H bend obtained at 1490.83 shows the presence of amides in the liquid oil. The C=C stretching at 1430.27 cm^{-1} indicates the presence of aromatic compounds in the co-pyrolysis oil. The C-H bending vibrations at 752 cm^{-1} showed an indication of aromatic hydrocarbons or arenes. The C-H bend that appeared at 674.31 shows the presence of aromatic compounds in the oil sample. The presence of strong aromatic compounds also occurred in the previous study [32, 33].

3.3. Engine Performance Analysis

3.3.1. Brake Power. Figure 4 depicts the variance in braking power with respect to engine load. The brake power of an IC engine is generally defined as the power available at the crankshaft. With increasing engine loads, the value of brake power for all tested fuels exhibited in increased trend. The brake power of the engine at full load conditions is 3.52, 3.45, 3.41, 3.3, and 3.18 kW for diesel, B5, B10, B15, and B20, respectively. Comparing with diesel, the result showed 1.99% and 3.13% decrement in brake power while the engine is operated at B5 and B10. For B15 and B20, the decrement in brake power was recorded as 6.25% and 9.66%, respectively, compared to diesel. At higher load operating condition beyond B10, a considerable loss in brake power was recorded. The higher decrements in brake power beyond B10 are due to inferior combustion properties of the fuel. The higher viscosity, presence of oxygen, and reduced calorific value decreased the engine brake power in all loads [34]. The same trends also obtained on CI engine were analysed by Pradhan et al. [29].

3.3.2. Brake-Specific Fuel Consumption. BSFC is basically defined by the ratio of the amount of fuel spent in kg to the engine's unit power output in kWh at the same engine load. It is the indicator used for the measurement of performance of any fuel. The values of BSFC are always expected to be low to the modified test fuels. Figure 5 shows the effect in BSFC based on different loads. The blended fuels achieved higher specific fuel consumptions for engine load than diesel oil due to its lower energy content in contrast with diesel. So to provide the same power output, the blended fuel requires injecting more fuel than diesel. As the volume proportion of co-pyrolysis oil to diesel oil increased, the value of BSFC increased for all loads. The higher viscosity of the blended fuels resulted in bigger fuel droplets due to poor atomization, penetration, and air-fuel mixing. Hence, it deteriorates
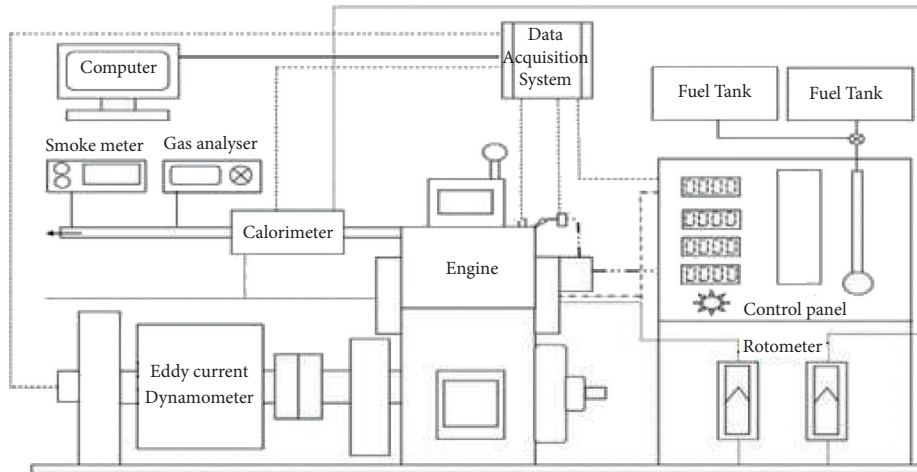
FIGURE 2: Block diagram of engine testing setup.

TABLE 3: Blend type with diesel.

Co-pyrolysis oil + diesel percentage	Blend name
0% + 100%	D
5% + 95%	B5
10% + 90%	B10
15% + 85%	B15
20% + 80%	B20

the burning and consumed higher fuel for specific output power [35]. The value of BSFC goes to its minimum value for all tested fuels as increased load might be due to the increased in-cylinder temperature. At elevated load conditions, the fuels can enter at proper condition to ignite to produce improved combustion efficiency. The similar pattern of output was also obtained from the previous researchers [36, 37]. In comparison to diesel fuel, the increment on the BSFC value is calculated to 3.85, 7.69, 19.23, and 26.92% for B5, B10, B15, and B20, respectively.

3.3.3. Brake Thermal Efficiency.

BTE is an important measure that demonstrates how the chemical energy of the fuel can be transformed efficiently into mechanical energy [38]. For any modified test fuel, the BTE is expected to be high by the researchers. Accordingly, Figure 6 portrayed the variation in BTE at different loads. The higher BTE value was recorded with baseline diesel fuel for all loads, while the lowest BTE value was recorded for B20 test fuel. The values of BTE at 100% load are 31.76, 31.21, 30.11, 27.45, and 25.03% for diesel, B5, B10, B15, and B20, respectively. A slight variation in BTE was recorded up to B10 blends. For B5 and B10, the result showed 1.73% and 5.2% decrement in BTE, whereas for B15 and B20 the values have changed to 13.57% and 21.19%, respectively. The higher variation in BTE for B15 and B20 blends is consistent with the previous literature, since the higher blends with higher heat loss have higher fuel consumption [39]. The blend's poor combustion character produced low BTE due to its lower volatility, lower calorific value, and increased viscosity. An improper burning

characteristic due to incomplete air-fuel is also the reason for reduced BTE.

3.4. Emission Characteristics

3.4.1. CO Emission.

Emission of CO is the effect of an incomplete combustion that begins to increase when the fuel cannot be oxidised or is oxidised insufficiently. Figure 7 shows the CO concentrations of diesel and blended fuels with respect to engine load. At lower loads, the CO emission value of blended fuels is closer to baseline diesel oil. For example, at 20% load, the CO emissions of diesel, B,5 and B10 are equal to 0.06%, whereas the values for B15 and B20 are 0.07% [40]. For a rated load of 40%, 60%, 80%, and 100%, the emission values observed at B5 and B10 blends were the same, and they are closer to neat diesel. At full load, the values were increased as the volumetric blending ratio of co-pyrolysis oil was increased. The increase in CO was less for B5 and B10; however, these values are for B15 and B20. This is due to the inefficient combustion, low volatility, and poor fuel-air mixture caused by higher viscosity [41] and may be endorsed to the presence of various chemical elements in the co-pyrolysis oil [29]. The low cetane number of the fuel causes the combustion to deteriorate with higher CO emissions, as seen by the decreased in-cylinder peak pressure. However, engine is operated with low to medium blended fuel at medium load, the level of increase in CO emissions is moderate and has no practical implications.

3.4.2. HC Emission.

Figure 8 illustrates the emission of HC concentrations based on engine load. Reduced loads resulted in lower HC emissions, whereas higher loads resulted in higher HC concentrations. The higher level of HC emissions is source d from incomplete combustion of fuel-air mixture. At 100% load, conditions for baseline diesel fuel HC emission varied from 23 ppm at 20% load and 29 ppm. For B5 and B10, it changed from 25 ppm and 26 ppm to 30 ppm and 31 ppm at 20% load to 100% load, respectively. In this study, increased blend increases the emission of HC. The increase in HC emission was less in case of B5 and B10,

TABLE 4: Properties of the fuel.

Items	Co-pyrolysis oil	B5	B10	B15	B20	Diesel
Density (kg/m^3)	1005	875	895	910	925	850
Kinematic viscosity (cSt)	4.28	3.95	4.12	4.15	4.20	3.9
Flash point (°C)	72	52	61	58	56	57
Fire point (°C)	75	61	73	68	65	67
Cetane number	24	40	38	35	33	50
Carbon residue	1.3	0.4	0.7	0.9	1.0	0.1
Calorific value in MJ/kg	40.3	42.76	42.62	42.10	41.7	43.60
Elemental analysis in wt%						
C	80.2	—	—	—	—	86.5
H	9.5	—	—	—	—	13.2
N	0.34	—	—	—	—	0.02
S	0.01	—	—	—	—	0.24
O[a]	9.95	—	—	—	—	—
H/C molar ratio	1.411	—	—	—	—	—
O/C molar ratio	0.093	—	—	—	—	—
Empirical formula	$CH_{1.41}N_{0.003}O_{0.093}$	—	—	—	—	—

[a]Percentage of oxygen = 100% − (C% + H% + N% + S%).
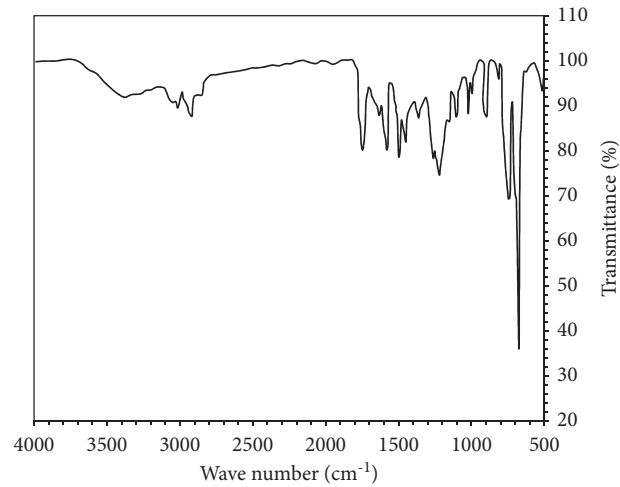
FIGURE 3: FTIR spectrum of co-pyrolysis oil.
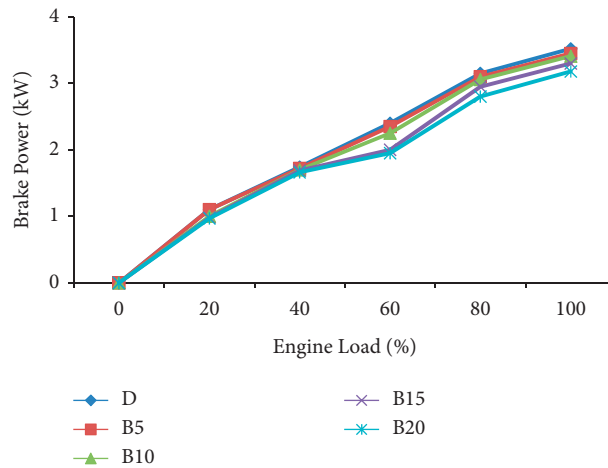
FIGURE 4: Variation of brake power with load.
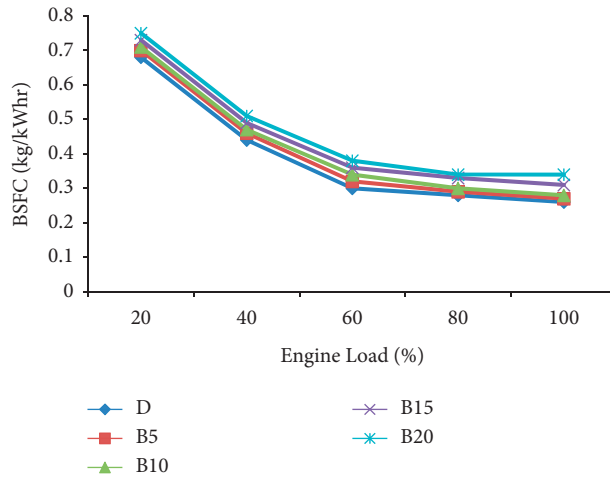
Figure 5: Variation of BSFC with load.
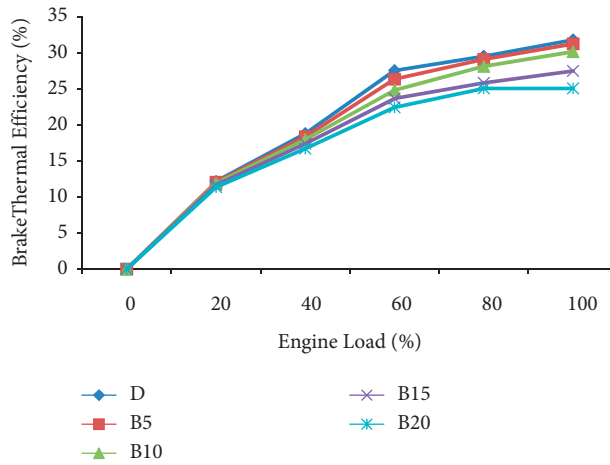
Figure 6: Variation of BTE with load.
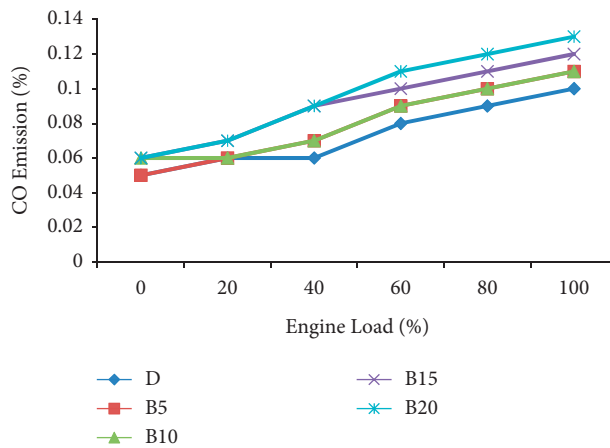
Figure 7: Variation of CO emissions with load.

though the values are more for B15 and B20. At 100% load, the emission of HC for B15 and B20 is recorded as 34 ppm and 36 ppm, respectively. In comparison to diesel fuel, the increment on the HC value is calculated to 3.45, 6.9, 17.24, and 24.14% for B5, B10, B15, and B20, respectively. The increased HC values for increased blends are caused by the
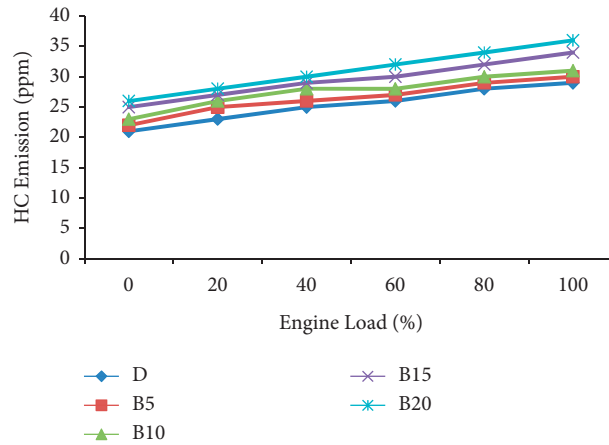
FIGURE 8: Variation of HC emissions with load.
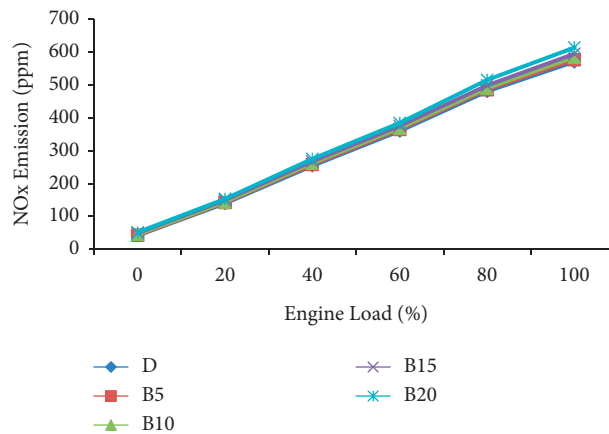
FIGURE 9: Variations of NOx emissions with load.

poor atomization, air-fuel mixing, and vaporization. The lower cetane number of the fuel causes longer ignition delay, increasing the impinging of fuel spray [42]. The presence of aromatic hydrocarbons in co-pyrolysis oil also enhanced the emission of HC since it is not breaking during combustion [43].

3.4.3. NOx Emission. NOx is another one important emission parameter which is formed inside the combustion chamber by the combination of nitrogen and oxygen. It is closely related to engine load since the formation is temperature dependent [44]. Figure 9 depicts the generation of NOx for various tested fuels. For diesel, NOx emission values are varied from 140 ppm at 20% load and 570 ppm at 100% load. For B5 and B10, the NOx emissions are varied from 142 to 144 ppm at 20% load and 576 to 584 ppm at 100% load. In general, more pyrolysis oil blends with diesel resulted in higher NOx emissions. The generation of NOx is often aided by higher oxygen levels in the combustion chamber [45]. Similarly, co-pyrolysis oil produced from

waste polystyrene and neem de oiled cake has certain oxygenated hydrocarbons, promoting the formation of NOx during combustion.

4. Conclusion

Co-pyrolysis oil from neem de oiled cake and waste polystyrene with the blend ratio of 1 : 2 were produced at the temperature of 550°C and blended with diesel to make different blends such as B5, B10, B15, and B20. The experimental results showed that B5 and B10 have quite related output properties like diesel. The BTE for all blended fuels is lower than diesel at all load conditions due to reduced calorific value. The value of BSFC increases with higher blend and decreased with increased load. The value of CO, HC, and NOx emissions increased as the amount of co-pyrolysis oil in the blend increases. Up to 10% blend, the decrement in engine performance and increment in engine emission are very minimal. From the results, it can be understood that the liquid oil derived from neem de oiled cake and waste polystyrene can be used as a promising

additive for fossil fuels. Further improvement can be possible by adding nanofuel additives, engine modification such as thermal barrier coating, and exhaust gas recirculation.

Nomenclature

NDC: Neem de oiled cake
WPS: Waste polystyrene
BTU: British thermal unit
IC: Internal combustion
CI: Compression ignition
BP: Brake power
BTE: Brake thermal efficiency
BSFC: Brake-specific fuel consumption
CO: Carbon monoxide
HC: Unburnt hydrocarbon
NOx: Oxides of nitrogen
ASTM: American Society for Testing and Materials
C: Carbon
H: Hydrogen
N: Nitrogen
S: Sulphur
FTIR: Fourier transform infrared spectroscopy.

Data Availability

The data used to support the findings of this study are included within the article.

Conflicts of Interest

The authors declare that there are no conflicts of interest regarding the publication of this article.

References

[1] A. Demirbas, "Potential applications of renewable energy sources, biomass combustion problems in boiler power systems and combustion related environmental issues," *Progress in Energy and Combustion Science*, vol. 31, no. 2, pp. 171–192, 2005.

[2] R. R. Appannagari, "Environmental pollution causes and consequences: a study," *North Asian International Research Journal of Social Science and Humanities*, vol. 3, no. 8, pp. 151–161, 2017.

[3] S. Curran, V. Prikhodko, K. Cho et al., "In-cylinder fuel blending of gasoline/diesel for improved efficiency and lowest possible emissions on a multi-cylinder light-duty diesel engine," SAE International, Warrendale, PA, USA, (No. 2010-01-2206). SAE Technical Paper, 2010.

[4] S. S. Mohapatra, M. K. Rath, R. K. Singh, and S. Murugan, "Performance and emission analysis of co-pyrolytic oil obtained from sugarcane bagasse and polystyrene in a CI engine," *Fuel*, vol. 298, Article ID 120813, 2021.

[5] M. Mohsin, Q. Abbas, J. Zhang, M. Ikram, and N. Iqbal, "Integrated effect of energy consumption, economic development, and population growth on CO2 based environmental degradation: a case of transport sector," *Environmental Science and Pollution Research*, vol. 26, no. 32, Article ID 32824, 2019.

[6] M. Sharifzadeh, M. Sadeqzadeh, M. Guo et al., "The multi-scale challenges of biomass fast pyrolysis and bio-oil upgrading: review of the state of art and future research directions," *Progress in Energy and Combustion Science*, vol. 71, pp. 1–80, 2019.

[7] M. E. M. Soudagar, A. Afzal, M. R. Safaei et al., "Investigation on the effect of cottonseed oil blended with different percentages of octanol and suspended MWCNT nanoparticles on diesel engine characteristic," *Journal of Thermal Analysis and Calorimetry*, pp. 1–18, 2020.

[8] D. Karuppan, A. M. Manokar, P. Vijayabalan et al., "Experimental investigation on pressure and heat release HCCI engine operated with chicken fat oil/diesel-gasoline blends," *Materials Today: Proceedings*, vol. 32, pp. 437–444, 2020.

[9] T. N. Verma, U. Rajak, A. Dasore et al., "Experimental and empirical investigation of a CI engine fuelled with blends of diesel and roselle biodiesel," *Scientific Reports*, vol. 11, no. 1, pp. 1–23, 2021.

[10] K. Vinukumar, A. Azhagurajan, S. C. Vettivel, N. Vedaraman, and A. H. Lenin, "Biodiesel with nano additives from coconut shell for decreasing emissions in diesel engines," *Fuel*, vol. 222, pp. 180–184, 2018.

[11] A. H. Lenin, R. Ravi, and K. Thyagarajan, "Performance characteristics of a diesel engine using mahua biodiesel as alternate fuel," *Iranica Journal of Energy and Environment*, vol. 4, no. 2, pp. 136–141, 2013.

[12] R. K. Kamaraj, G. R. Jinu, A. F. Panimayam, and H. L. Allasi, "Performance and exhaust emission optimization of a dual fuel engine by response surface methodology," *Energies*, vol. 11, no. 12, Article ID 3508, 2018.

[13] P. H. Vu, O. Nishida, H. Fujita, W. Harano, N. Toyoshima, and M. Iteya, "Reduction of NOx and PM from diesel engines by WPD emulsified fuel," SAE International, Warrendale, A, USA, (No. 2001-01-0152). SAE Technical Paper, 2001.

[14] A. Dewangan, D. Pradhan, and R. K. Singh, "Co-pyrolysis of sugarcane bagasse and low-density polyethylene: influence of plastic on pyrolysis product yield," *Fuel*, vol. 185, pp. 508–516, 2016.

[15] Z. Wang, K. G. Burra, T. Lei, and A. K. Gupta, "Co-pyrolysis of waste plastic and solid biomass for synergistic production of biofuels and chemicals-a review," *Progress in Energy and Combustion Science*, vol. 84, Article ID 100899, 2021.

[16] R. K. Singh and K. P. Shadangi, "Liquid fuel from castor seeds by pyrolysis," *Fuel*, vol. 90, no. 7, pp. 2538–2544, 2011.

[17] E. Önal, B. B. Uzun, and A. E. Pütün, "Bio-oil production via co-pyrolysis of almond shell as biomass and high density polyethylene," *Energy Conversion and Management*, vol. 78, pp. 704–710, 2014.

[18] H. J. Park, H. S. Heo, K. S. Yoo et al., "Thermal degradation of plywood with block polypropylene in TG and batch reactor system," *Journal of Industrial and Engineering Chemistry*, vol. 17, no. 3, pp. 549–553, 2011.

[19] F. Abnisa, W. W. Daud, S. Ramalingam, M. N. B. M. Azemi, and J. N. Sahu, "Co-pyrolysis of palm shell and polystyrene waste mixtures to synthesis liquid fuel," *Fuel*, vol. 108, pp. 311–318, 2013.

[20] V. I. Sharypov, N. G. Beregovtsova, B. N. Kuznetsov et al., "Co-pyrolysis of wood biomass and synthetic polymers mixtures: part IV: catalytic pyrolysis of pine wood and polyolefinic polymers mixtures in hydrogen atmosphere," *Journal of Analytical and Applied Pyrolysis*, vol. 76, no. 1-2, pp. 265–270, 2006.

[21] N. Marin, S. Collura, V. I. Sharypov et al., "Copyrolysis of wood biomass and synthetic polymers mixtures. part II: characterisation of the liquid phases," *Journal of Analytical and Applied Pyrolysis*, vol. 65, no. 1, pp. 41–55, 2002.

[22] S. Papari, H. Bamdad, and F. Berruti, "Pyrolytic conversion of plastic waste to value-added products and fuels: a review," *Materials*, vol. 14, no. 10, p. 2586, 2021.

[23] J. N. Nair, A. K. Kaviti, and A. K. Daram, "Analysis of performance and emission on compression ignition engine fuelled with blends of neem biodiesel," *Egyptian Journal of Petroleum*, vol. 26, no. 4, pp. 927–931, 2017.

[24] S Rathinam, J.B Sajin, G Subbiah, A Rajeev, and S PrakashS, "Assessment of the emission characteristics of the diesel engine with nano-particle in neem biodiesel," *Energy Sources, Part A: Recovery, Utilization, and Environmental Effects*, vol. 42, no. 21, pp. 2623–2631, 2020.

[25] K. B. Park, Y. S. Jeong, B. Guzelciftci, and J. S. Kim, "Two-stage pyrolysis of polystyrene: pyrolysis oil as a source of fuels or benzene, toluene, ethylbenzene, and xylenes," *Applied Energy*, vol. 259, Article ID 114240, 2020.

[26] R. R. N. Bhattacharya, K. Chandrasekhar, P. Roy, M. V. Deepthi, and A. Khan, "Challenges and opportunities: plastic waste management in India," *The Energy and Resources Institute*, vol. 24, 2018.

[27] B. B. Uzoejinwa, X. He, S. Wang, A. E. F. Abomohra, Y. Hu, and Q. Wang, "Co-pyrolysis of biomass and waste plastics as a thermochemical conversion technology for high-grade bio-fuel production: recent progress and future directions elsewhere worldwide," *Energy Conversion and Management*, vol. 163, pp. 468–492, 2018.

[28] R. Prakash, R. K. Singh, and S. Murugan, "Experimental investigation on a diesel engine fueled with bio-oil derived from waste wood–biodiesel emulsions," *Energy*, vol. 55, pp. 610–618, 2013.

[29] D. Pradhan, V. Volli, R. K. Singh, and S. Murgun, "Co-pyrolysis behavior, engine performance characteristics, and thermodynamics of liquid fuels from mahua seeds and waste thermocol: a comprehensive study," *Chemical Engineering Journal*, vol. 393, Article ID 124749, 2020.

[30] P. R. Churkunti, J. Mattson, C. Depcik, and G. Devlin, "Combustion analysis of pyrolysis end of life plastic fuel blended with ultra low sulfur diesel," *Fuel Processing Technology*, vol. 142, pp. 212–218, 2016.

[31] Q. Van Nguyen, Y. S. Choi, S. K. Choi, Y. W. Jeong, and Y. S. Kwon, "Improvement of bio-crude oil properties via co-pyrolysis of pine sawdust and waste polystyrene foam," *Journal of Environmental Management*, vol. 237, pp. 24–29, 2019.

[32] G. Özsin and A. E. Pütün, "A comparative study on co-pyrolysis of lignocellulosic biomass with polyethylene terephthalate, polystyrene, and polyvinyl chloride: synergistic effects and product characteristics," *Journal of Cleaner Production*, vol. 205, no. 20, pp. 1127–1138, 2018.

[33] F. Abnisa, W. W. Daud, and J. N. Sahu, "Optimization and characterization studies on bio-oil production from palm shell by pyrolysis using response surface methodology," *Biomass and Bioenergy*, vol. 35, no. 8, pp. 3604–3616, 2011.

[34] L. Tarabet, K. Loubar, M. S. Lounici, S. Hanchi, and M. Tazerout, "Experimental evaluation of performance and emissions of DI diesel engine fuelled with eucalyptus bio-diesel," in *Proceedings of the Internal Combustion Engines: Performance, Fuel Economy and Emissions*, pp. 167–176, 2011.

[35] G. Chen, C. Liu, W. Ma et al., "Co-pyrolysis of corn cob and waste cooking oil in a fixed bed," *Bioresource Technology*, vol. 166, pp. 500–507, 2014.

[36] M. Karagöz, Ü. Ağbulut, and S. Sarıdemir, "Waste to energy: production of waste tire pyrolysis oil and comprehensive

analysis of its usability in diesel engines," *Fuel*, vol. 275, Article ID 117844, 2020.

[37] Ü. Ağbulut, A. E. Gürel, and S. Sarıdemir, "Experimental investigation and prediction of performance and emission responses of a CI engine fuelled with different metal-oxide based nanoparticles–diesel blends using different machine learning algorithms," *Energy*, vol. 215, Article ID 119076, 2021.

[38] N. Phetyim and S. Pivsa-Art, "Prototype co-Pyrolysis of used lubricant oil and mixed plastic waste to produce a diesel-like fuel," *Energies*, vol. 11, no. 11, p. 2973, 2018.

[39] S. Lee, L. Chen, K. Yoshida, and K. Yoshikawa, "Application of waste biomass pyrolysis oil in a direct injection diesel engine: for a small scale non-grid electrification," *Journal of Energy and Power Engineering*, vol. 9, pp. 929–943, 2015.

[40] A. Dhar and A. K. Agarwal, "Performance, emissions and combustion characteristics of Karanja biodiesel in a transportation engine," *Fuel*, vol. 119, pp. 70–80, 2014.

[41] T. Ito, Y. Sakurai, Y. Kakuta, M. Sugano, and K. Hirano, "Biodiesel production from waste animal fats using pyrolysis method," *Fuel Processing Technology*, vol. 94, no. 1, pp. 47–52, 2012.

[42] M. S. Radwan, M. A. Ismail, S. M. S. Elfeky, and O. S. M. Abu-Elyazeed, "Jojoba methyl ester as a diesel fuel substitute: preparation and characterization," *Applied Thermal Engineering*, vol. 27, no. 2-3, pp. 314–322, 2007.

[43] Y. Kidoguchi, C. Yang, R. Kato, and K. Miwa, "Effects of fuel cetane number and aromatics on combustion process and emissions of a direct-injection diesel engine," *JSAE Review*, vol. 21, no. 4, pp. 469–475, 2000.

[44] E. Buyukkaya and M. Cerit, "Experimental study of NOx emissions and injection timing of a low heat rejection diesel engine," *International Journal of thermal Sciences*, vol. 47, no. 8, pp. 1096–1106, 2008.

[45] P. Senthilkumar and G. Sankaranarayanan, "Effect of Jatropha methyl ester on waste plastic oil fueled DI diesel engine," *Journal of the Energy Institute*, vol. 89, no. 4, pp. 504–512, 2016.

Research Article

The Durability of High-Strength Concrete Containing Waste Tire Steel Fiber and Coal Fly Ash

Babar Ali [iD],[1] **Erol Yilmaz** [iD],[2] **Ahmad Raza Tahir,**[1] **Fehmi Gamaoun,**[3,4]
Mohamed Hechmi El Ouni,[5,6] **and Syed Muhammad Murtaza Rizvi**[1]

[1]*Department of Civil Engineering (CVE), COMSATS University Islamabad (CUI)-Sahiwal Campus, Sahiwal 57000, Pakistan*
[2]*Department of Civil Engineering, Recep Tayyip Erdoğan University, Rize, Turkey*
[3]*Department of Mechanical Engineering, College of Engineering, King Khalid University, Abha 61421, Saudi Arabia*
[4]*Laboratory of Mechanics of Sousse, National Engineering School of Sousse, University of Sousse, Sousse 4054, Tunisia*
[5]*Department of Civil Engineering, College of Engineering, King Khalid University, P.O. Box 394, Abha 61411, Saudi Arabia*
[6]*Applied Mechanics and Systems Research Laboratory, Tunisia Polytechnic School, University of Carthage, La Marsa,
 Tunis 2078, Tunisia*

Correspondence should be addressed to Babar Ali; babar.ali@cuisahiwal.edu.pk

The demands for high-strength concrete (HSC) have been increasing rapidly in the construction industry due to the requirements of thin and durable structural elements. HSC is highly brittle. Therefore, to augment its ductility behavior, expensive fibers are used. These negative drawbacks of HSC can be controlled by incorporating waste materials into its manufacturing instead of conventional ones. Therefore, this study assessed the performance of HSC produced with different quantities of waste tire steel fiber (WSF) and fly ash (FA). WSF was used at two doses, namely, 0.5% and 1%, by volume in HSC, with low-to-medium volumes of FA, that is, 10%–35%. The studied durability parameters included rapid chloride permeability (RCP) and chloride penetration depth (CPD) by immersion method (28 and 120 days) and acid attack resistance (AAR) (28 and 120 days). Various basic mechanical properties of HSC were also analyzed, such as compressive strength (f_{CM}), modulus of elasticity (E_{CM}), splitting-tensile strength (f_{CTM}), and modulus of rupture (f_{CRM}). The results revealed that the damaging effect of WSF on the RCP resistance of HSC is probably due to the high conductivity of steel fibers. However, test results of *CPD* showed that WSF produced insignificant changes in chloride permeability of HSC. Furthermore, when made with FA, WSF-reinforced HSC yielded very low chloride permeability. Both WSF and FA contributed to the improvement in the *AAR* of HSC. WSF was highly useful to tensile properties while it showed minor effects on compressive properties (f_{CM} and E_{CM}). Optimum ductility and durability can be achieved with HSC incorporating 1% WSF and 10%–15% FA.

1. Introduction

The impacts of cement concrete manufacturing and its uses are quite complex to comprehend. Some impacts are positive, and others are negative, depending on the situation. Portland cement is the vital ingredient of concrete that has various environmental, economic, and social impacts. The impacts of cement also contribute to those of the concrete. The cement industry alone releases about 7% of the total greenhouse emissions produced all over the world [1]. Rapid growth in urban populations and the requirement of modern infrastructure have increased the demand for cement, which consequently reflects badly on the quality of the environment and social life. About 0.7–1 kilogram of global warming gases is produced due to 1-kilogram production of Portland cement, depending on the type of energy source and technology employed to manufacture cement [2]. While the other ingredients of concrete such as sand and gravels have a small CO_2 footprint, their cost and CO_2 footprint largely depend on their transportation distances between the

quarry and concrete batching plant. Therefore, about 85% of emissions of cement concrete are dependent on the binder constituent of concrete [3, 4]. The most effective way to control the environmental impact of concrete is to minimize its cement consumption. This can be achieved by the utilization of industrial waste powders that possess pozzolanicity and hydraulicity. The substitution of a small and medium volume of cement with these waste powders can drastically reduce the CO_2 footprint of concrete. However, the efficacy of potential cement substitution materials should be assessed properly in terms of their contribution towards durability and mechanical performance. The cost to strength [5, 6] or CO_2 footprint to strength ratio analysis [7] should always be performed to judge the technical performance of cementitious materials.

Fly ash (FA) is a common waste mineral powder, which is a product of pulverized fuel ash burning for electric power generation. FA incorporation into cement concrete cannot only decrease the CO_2 footprint of concrete, but it can also resolve waste disposal problems associated with high volumes of coal ashes. FA can help in gaining a circular economy in modern-day concrete manufacturing. Pakistan relies heavily on nonrenewable supplies of energy, such as coal-fed power plants. Therefore, abundant supplies of FA are available in this country. FA is rich in alumina-silica, and it has minor amounts of calcium and iron oxides. It qualifies as a potential cement replacement material [8]. The effects of FA on the properties of concrete have been studied properly. It helps in the slow consumption of residual portlandite $Ca(OH)_2$ and positively affects the resistance of concrete against water absorption, chloride attack, and drying shrinkage [9–11]. Low levels of FA can cause minor improvements in the mechanical performance of concrete [12], but its high levels drastically reduce mechanical strength [7, 13]. The degree of the effectiveness of FA depends on its fineness, chemical composition, and unburnt carbon content [14–17]. Generally, FA with high fineness and low carbon content is considered suitable for concrete applications.

Due to the increasing information gained related to material availability, design, and construction techniques, the practical scope of high-strength concrete (HSC) applications has been expanded dramatically. Rising inclination towards lightweight elements, large spans in buildings and bridges have increased the demands for HSC. However, there is a faction among designers unwilling to use HSC owing to its some drawbacks compared to conventional normal strength concrete (NSC) [18]. To begin with, HSC has a low f_{CTM} compared to its f_{CM}. The increase in the strength class of concrete reduces the ratio between f_{CTM} and f_{CM} [19]. This means that the gain in f_{CTM} achieved due to the low water-cement ratio is not proportional to the gain in f_{CM}. Due to low ductility, HSC is extremely brittle in fire temperatures. Due to a dense microstructure, the fire resistance of HSC is incredibly lower than the NSC [20].

The brittleness issue of HSC can be addressed by using fibers. Various options for fiber reinforcements are available, such as steel, carbon, polypropylene, polyvinyl, and glass fibers [21–23]. The use of fibers substantially enhances the tensile and fracture toughness of HSC. The selection of fiber type varies depending upon the application of HSC. Fiber addition is highly useful in enhancing f_{CTM} and flexural strength f_{CRM} of HSC [22]. In short, fibers can overcome the inherent issue of brittleness associated with both plain HSC and NSC. Research has shown the negative effects of fiber addition on the economy and the environmental impact of concrete [24]. High transportation distances significantly increase the cost and CO_2 footprint of fibers [24]. Their small doses can noticeably increase the cost and CO_2 footprint of concrete. Fiber addition also requires technical supervision; it creates workability issues when used in HSC. Therefore, the use of additional measures and materials to control the quality of concrete can increase the final cost. Therefore, the selection of fiber type should be made based on a comprehensive cost to benefit ratio analysis.

The development of ductile, cheap, and environment-friendly HSC is not possible without considering the less energy-intensive fibers compared to industrially manufactured fibers available at distant locations. Currently, researchers are investigating the potential of waste tire steel fibers (WSF) as the fiber reinforcement in cement concrete. Since WSF is composed of ultra-high-strength steel wires, which are designed for good fatigue resistance, it can become a potential fiber reinforcement material. WSF behaves similar to virgin steel fiber to a great extent, considering the properties of ultra-high performance concrete [25]. Considering the wider availability of old waste tires, WSF can become a local fiber-reinforcement material in all regions of the world, so high transportation costs can be avoided by adopting WSF instead of industrial fibers.

New steel fiber and WSF behave similarly as fiber reinforcement due to the same material. Small doses of WSF can be useful to f_{CM} of concrete, whereas using a large dose of WSF can lessen the f_{CM} of concrete [26]. A high dose of WSF increases the porosity of concrete due to workability issues that reflect badly in terms of compression stiffness of concrete [26]. WSF can postpone the collapse of concrete under compression; it can ensure ductile and slow cracking with a significant warning before collapse [27]. The effect of WSF on the properties of concrete significantly depends on the length, shape, texture, and residual rubber content of fiber [28]. The incorporation of 0.46% volume of irregular-shaped WSF in concrete improved its f_{CM} by 25% [29]. At the same volume of 0.75% WSF and new steel fibers, f_{CTM} of concrete increased by 28% and 26%, respectively, whereas by the use of WSF carrying mixed filament lengths, f_{CTM} of plain concrete was increased by about 50% [30, 31]. Similar to compressive behavior, the postpeak flexure response of concrete depends on the type, dose, and the number of filaments per unit volume. f_{CRM} of concrete significantly increases with the rise in WSF dosage [32, 33]. WSF provides a crack-arresting mechanism that helps in delaying the onset of rupture failure of concrete [31, 34–37].

The incorporation of FA and WSF into HSC can integrate the benefits of ductility, durability, and ecofriendliness. The simultaneous use of waste mineral admixtures and fibers proves beneficial in three different ways: (1) fine particles of mineral admixtures can improve the distribution of

filaments throughout the matrix of concrete [38], [39]; (2) mineral admixtures increase the interface between filaments and binder matrix that improves the bond performance of fibers [40, 41]; and (3) some mineral admixtures reduce the water demand of concrete due to their slow hydration and filling action, hence reducing the requirement of water-reducing agents to maintain the workability of fiber-reinforced concretes [42–45]. Due to these benefits, fibers and mineral admixture addition show some synergistic results on the performance of concrete [9]. There are very few studies that investigate the combined behavior of FA and WSF. However, many studies are available related to the combined behavior of industrial fibers and waste mineral admixtures (i.e., FA, silica fume, slag, etc.) [46–48]. The combined behavior of WSF and mineral admixture was studied by Mastali and Dalvand [27]. They found that the combined addition of silica fume and WSF improves the overall toughness and strength of concrete.

Very little information is available on the durability behavior of HSC made with the combined incorporation of WSF and FA. Moreover, information on mechanical behavior is also deficient. Due to already explained environmental, economic, and ductility benefits, the combined effect of WSF and FA should be properly investigated on the properties of HSC. Therefore, this research aimed to evaluate the effects of different combinations of FA (0, 10, 15, 25, and 35%) and WSF (0, 0.5, and 1%) on the properties of HSC. The examined durability parameters involve RCP and CPD by immersion method (at 28 and 120 days) and AAR (at 28 and 120 days). Various basic mechanical properties of HSC were also studied experimentally, such as f_{CM}, f_{CTM}, f_{CRM}, and E_{CM}. The findings of this research fill an important research gap related to the durability of waste tire steel fiber-reinforced concrete. Moreover, the combined effect of FA and WSF on both durability and mechanical properties of HSC has never been studied before.

2. Materials and Methods

2.1. Constituent Materials

2.1.1. Binding Materials. HSC mixes were prepared with 53-grade cement, which was used as the major binder. It is qualified as "Type-I cement" per ASTM C150 [49]. FA containing a low percentage of lime was acquired from a local coal power plant. It was a by-product of bituminous coal. The generation of FA was estimated to be 10% of the annual cement production of Pakistan. The composition of the FA is Class F type, known for pozzolanicity potential but low hydraulicity. Important properties of FA and 53-grade cement are given in Table 1.

2.1.2. Aggregates. Quarry sand of "Lawrencepur" was used as fine aggregate to manufacture HSC. This sand is recommended for good-quality concrete production in Punjab, Pakistan. This coarse-grained sand has a good distribution of particle sizes and has a "fineness moduli" of 2.92. Crushed dolomite sandstone was used as coarse aggregate. This aggregate was derived from Kirana Hills of Sargodha, Punjab,

Pakistan. Engineering properties of fine and coarse aggregates are given in Table 2, which were important inputs in the mix design procedure of HSC. The diversity in particle sizes of both "quarry sand" and "crushed coarse aggregate" is shown in Figure 1. The maximum aggregate sizes for "fine" and "coarse" aggregates are 4.75 and 12.5 mm, respectively.

2.1.3. WSF. WSF used in this research was derived from old waste tires of truck vehicles. The tire-bead wires, when removed from waste tires, contained residual rubber. Therefore, heat treatment was applied to remove the rubber particles from steel wires. Removing rubber particles is necessary to ensure a good bond between fibers and the matrix of the concrete. Moreover, rubber reduces f_{CM} of concrete owing to its low density [28]. Finally, clean steel wires were chopped into lengths of about 30 mm. WSF consists of spun filaments as can be noticed in Figure 2. The diameter of each filament was about 1.2 mm. WSF also contains microsteel wires that were twined around the main filament in the tire bead. These small wires may provide hybrid (mixed-length and mixed-diameter effects) of fibers on the properties of HSC.

2.1.4. Water-Reducing Agent and Water. The desired workability of an HSC mixture was achieved by using a commercial third-generation water-reducing agent "ViscoCrete 3110." It also helped in controlling the drop in workability due to the addition of WSF. Tap water from the concrete laboratory was used in the preparation and curing of HSC mixes. It has a pH of 7.9 and total dissolved solid content of 170 mg/L.

2.2. Design HSC Concrete Mixes with Different Combinations of WSF and FA. In this research control or reference, HSC was designed for a cubical f_{CM} of 70 MPa. This strength class was achieved by employing a water-binder ratio of 0.30. In order to achieve good workability (a slump value of 190–210 mm), the "ViscoCrete 3110" water-reducing agent was used at 0.75% by weight of binder in reference HSC. Details about the composition of a reference mix are given in Table 3. In HSC, FA was used at five different levels, 0%, 10%, 15%, 25%, and 35%, by volumetric replacement of cement. Since FA is lighter than cement, the replacement of cement with FA should be done by volume. Then, with each incorporation level of FA, three different doses of WSF, 0%, 0.5%, and 1%, by a volumetric fraction of concrete were used. Therefore, the experimental campaign studied a total of 15 concrete mixtures. Details of all 15 mixes are given in Table 3. It is worth mentioning here that plain HSC mixtures containing FA achieved the required range of workability at 0.75% dose of water-reducing agent, while all fiber-reinforced HSC mixes required a 1% dose of water-reducing agent to achieve desirable workability. The workability was because the use of WSF increased the stiffness of fresh concrete. Therefore, the loss in workability due to the fiber addition was compensated with a high dose of plasticizer. All plain mixtures (without fibers) (serial nos. 1, 4, 7, 10, 13)

TABLE 1: Engineering characteristics of binders used in this study.

Binder	Chemical properties						Physical properties		
	CaO	Al$_2$O$_3$	SiO$_2$	Fe$_2$O$_3$	LOI	PSG	Density (kg/m^3)	SSA (m^2/kg)	Soundness (%)
FA	4.3	28.4	61.0	3.4	1.4	2.31	1128	345	—
Cement	64.2	6.7	23.9	4.3	4.7	3.12	1441	321	0.09

LOI: loss on ignition; PSG: particle specific gravity; SSA: specific surface area.

TABLE 2: Engineering characteristics of aggregates used in this research.

Aggregate type	Particle size (mm)		WA (%)	PSG	FM
	Max	Min			
Quarry sand (fine aggregate)	4.75	0.075	0.76	2.66	2.92
Crushed sandstone (coarse aggregate)	12.5	2.36	0.79	2.72	—

WA: water absorption at 24 hrs; PSG: particle specific gravity; FM: fineness modulus.
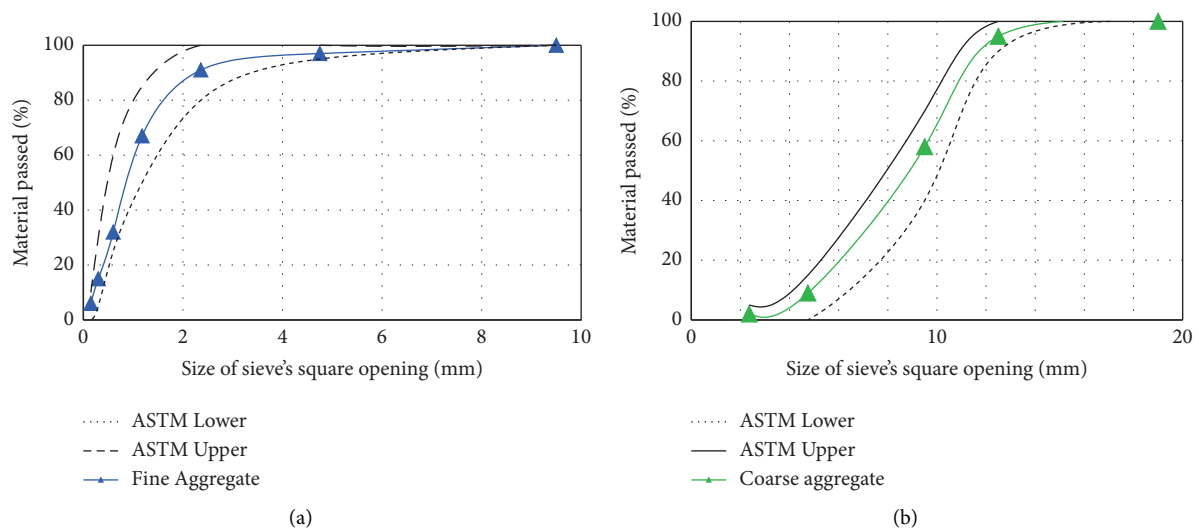

(a)

(b)

FIGURE 1: The aggregate size gradation curves of (a) quarry sand and (b) coarse aggregate following ASTM C33 [50].

FIGURE 2: An overview of a random sample of WSF.

attained a slump value of 180–210 mm, while WSF-reinforced mixes (serial nos. 2, 3, 5, 6, 8, 9, 11, 12, 14, and 15) attained slump values of 125–145 mm.

2.3. Mixing Method. HSC mixes containing WSF (serial nos. 2, 3, 5, 6, 8, 9, 11, 12, 14, and 15) were mixed in four continuous stages: (1) in the first step, cement, FA, and aggregates were mixed in machine mixer for 2 mins at a speed of 40 rev/min (revolutions per minute); (2) in the second step, half the amount of water and water-reducing agents were added to mix and blend in machine mixer continued for 2 mins at a speed of 40 revs/min; (3) in the third step, the remaining quantities of water-reducing agent and water were added and mixed, and blending was done at high speed of 60 rev/min for 2 mins; and (4) in the

TABLE 3: Information about the composition of concrete mixtures.

Serial. no.	Mix ID	FA (%)	WSF (%)	Cement (kg/m³)	FA (kg/m³)	Fine aggregate (kg/m³)	Coarse aggregate (kg/m³)	WSF (kg/m³)	Water (kg/m³)	SP (%)
1	F0WF0 (Ref)	0	0	500	0	865	904	0	150	0.75
2	F0WF0.5		0.5	500	0	859	898	39	150	1
3	F0WF1		1	500	0	852	891	78	150	1
4	F10WF0		0	450	37	865	904	0	150	0.75
5	F10WF0.5	10	0.5	450	37	859	898	39	150	1
6	F10WF1		1	450	37	852	891	78	150	1
7	F15WF0		0	425	56	865	904	0	150	0.75
8	F15WF0.5	15	0.5	425	56	859	898	39	150	1
9	F15WF1		1	425	56	852	891	78	150	1
10	F25WF0		0	375	93	865	904	0	150	0.75
11	F25WF0.5	25	0.5	375	93	859	898	39	150	1
12	F25WF1		1	375	93	852	891	78	150	1
13	F35WF0		0	325	130	865	904	0	150	0.75
14	F35WF0.5	35	0.5	325	130	859	898	39	150	1
15	F35WF1		1	325	130	852	891	78	150	1

fourth stage, measured quantities of WSF were charged into the mixer, and machine mixing was done for 4 mins at 80 revs/min to ensure proper dispersion of cement particles and fiber filaments. Plain mixes (serial nos. 1, 4, 7, 10, 13) were mixed in the first three stages which were used for the mixing of WSF-HSC mixes.

After completion of mixing, fresh concrete mixtures were tested for the slump, and mixes qualifying the workability requirements were proceeded for casting. During the casting stage, the machine mixer kept running at a low speed of 40 rev/min. Casting was completed within 4–5 mins of completion of the mixing stage.

2.4. Sample Details and Testing Methods. Six cubes of 100 mm dimensions were prepared for each mixture. The f_{CM} was determined at 28 and 120 days; three cubes of each mix were tested at one age. The standard of testing was followed as per ASTM C39 [51]. The testing setup is shown in Figure 3(a). Cylindrical samples of 100 mm diameter and 200 mm height were cast for E_{CM} testing, as shown in Figure 3(b). Three cylinders per mix were cast, of which were tested at 28 days and the remaining three 120 days. The standard of testing was adopted from ASTM C469 [52]. This test was performed to estimate the effect of WSF on the ductility of samples. For this purpose, cylindrical specimens of "100 mm diameter and 200 mm" height were prepared. Three replica samples of each mix were tested at 28 days. The standard of testing was adopted from ASTM C496 [53]. The testing overview is shown in Figure 3(c). "Flexural strength" or "modulus of rupture f_{CRM}" is a tensile property of concrete that is employed in the design equations of flexural elements, such as slabs and pavements. For each mix, three specimens having dimensions of 100 mm × 100 mm × 350 mm were tested for the calculation of f_{CRM}. f_{CRM} was determined under the third-point loading method adopted from ASTM C1609 [54]. The test setup is shown in Figure 3(d).

The chloride durability is an important characteristic of concrete that tells about the life of a reinforced structural element. *RCP* test was conducted on 100 mm diameter × 50 mm height disc specimens of each mix. The test method was adopted from ASTM C1202 [55]. *RCP* test was performed by maintaining a potential difference of 60 volts for the duration of 6 hrs. The overview of *RCP* testing is shown in Figure 4.

Chloride-ion penetration depth (*CPD*) by immersion method was also measured to understand the effects of WSF and FA on the permeability of chloride ions in the absence of applied voltage. Since WSF addition highly increases the electrical conductivity of HSC [43], it becomes more convenient to adopt the natural process of measuring chloride penetrability of HSC rather than the *RCP* test, to avoid wrong interpretation of *RCP* test results of steel fiber-reinforced concretes. For the immersion test method, six cylindrical specimens (100 mm height × 100 mm diameter) of each mix were cured in tap water for 28 days, and then air-dried for 3 days at room temperature. These air-dried specimens were then soaked in a 10% solution of sodium chloride (NaCl) salt. *CPD* was then measured by spraying 0.1 normality solution of silver nitrate ($AgNO_3$) salt, on the split surfaces of NaCl conditioned samples after periods of 28 and 120 days. Three replica samples were tested at each age to determine the average *CPD* value of each HSC mix.

Measuring the *AAR* of HSC is very important, as there are some applications where concrete experiences harsh acidic environments, such as in components of sewerage networks. Method of *AAR* testing was adopted from a previous study [9], where *AAR* was measured by quantifying the differences between fresh samples and acid exposed samples. For *AAR* testing, three replica specimens (100 mm cubes) of each mix were cured in tap water for 28 days. These specimens were then air-dried at room temperature for 3 days. Then, the samples of all mixes were exposed to sulfuric acidic (H_2SO_4) solution of 5% concentration. The change in
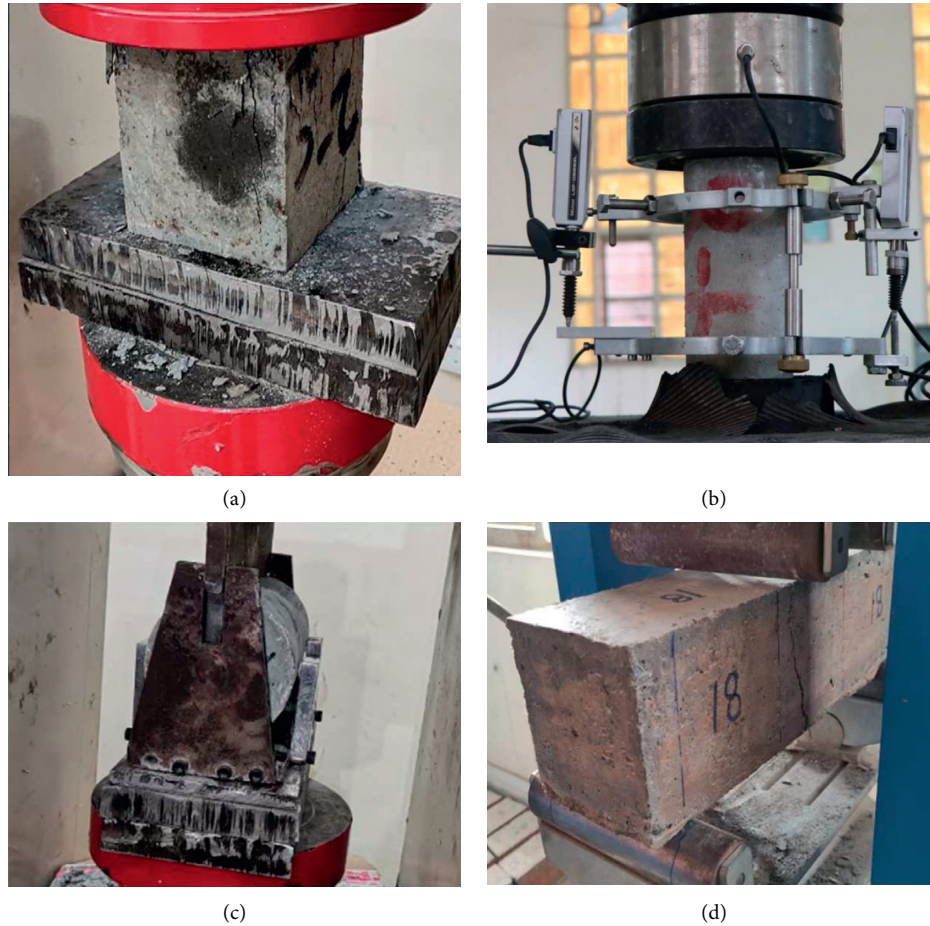
(a)

(b)

(c)

(d)

FIGURE 3: Overview of mechanical testing. (a) Compression test on 100 mm cubes. (b) Overview of axial testing for ECM determination. (c) Splitting-tensile test on "100 mm × 200 mm" cylindrical samples. (d) Overview of flexural testing on "100 mm × 100 mm × 350 mm" prismatic samples.

FIGURE 4: Overview of RCP testing.

the mass of specimens was measured after exposure periods of 14, 28, 56, and 120 days.

3. Results and Discussion

3.1. Compressive Properties

3.1.1. Compressive Strength (f_{CM}). f_{CM} of all fifteen mixes at the ages of 28 and 120 days is shown in Figure 5. Both FA and WSF addition showed mixed effects of f_{CM} depending

on their percentage in an HSC mix. The 28 days f_{CM} of HSC was increased by 6% at 10% FA addition. This improvement in f_{CM} was credited to the effective filling effect and development of pozzolanic products [12, 15]. While f_{CM} of HSC decreased notably compared to the reference mix, with the rising level of FA. This could be blamed on a reduction in the overall lime content of the binder. Although smaller particles of FA provided a filling effect, at a high level, FA fails to develop necessary reactions responsible for strength. As FA particles reacted slowly with available portlandite,
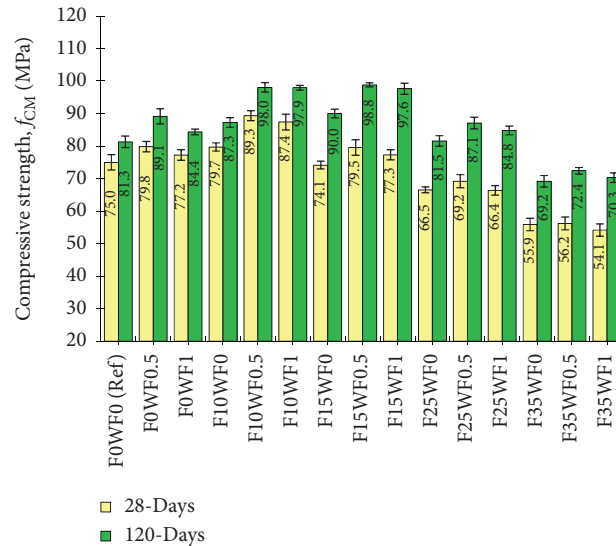
Figure 5: Effect of FA and WSF combinations on compression testing results of concrete.

HSC mixtures containing 10–15% developed noticeably (i.e., 7–11%) higher f_{CM} than the reference mix. While mix containing 25% FA showed f_{CM} similar to the reference mix at 120 days.

0.5% WSF improved f_{CM} by about 6.5 and 10% at 28 and 120 days, respectively. While 1% WSF did not show a significant effect on f_{CM} generally on all five types of plain mixes (1, 4, 7, 10, 13). At a high-volume fraction, the negative effect of WSF can be blamed on an increase in porosity and heterogeneity in the HSC matrix. A high volume of fibers produces small void pockets that decrease the efficiency of fibers contributing to the compression stiffness of concrete. Similar behavior was observed with WSF in another study [37]. Moreover, new steel fiber also showed mixed effects on f_{CM} of HSC with varying doses [56, 57]. High volume doses of fibers were not effective in increasing the peak-load capacity, but these were beneficial to the postpeak response. The high volume of WSF restricted the sharp failure and helped in sustaining a noticeable residual strength after peak load. The failure patterns of plain HSC and WSF-HSC are shown in Figure 6.

The combined effect of WSF and FA on f_{CM} of HSC at 28 and 120 days can be observed in Figure 7. Maximum f_{CM} was shown by HSC containing 0.5% WSF and 10–15% FA because both 0.5% WSF and 10–15% FA were individually helpful to f_{CM}; therefore, their combined addition significantly improved f_{CM}. Mix no. 5 (F10WF0.5) showed 19% and 21% greater f_{CM} than reference mix at 28 and 120 days, respectively. It is also worth mentioning that, due to the increase in age and hardening of the binder with 10–15% FA, 1% WSF showed a similar effect on f_{CM} compared to 0.5% WSF at 120 days. An increase in age may improve the bond of fibers with HSC's matrix. Therefore, F10WF1 showed performance similar to FA10WF0.5 at 120 days.

At 120 days, maximum f_{CM} was shown by FA15WF0.5, which was 22% higher than that of the reference mix. At 120 days, mixes incorporating 0.5–1% WSF and 10–25% FA showed noticeably higher f_{CM} than the reference mix. These results showed the usefulness of ecofriendly FA and WSF in improving f_{CM}. The combined addition of FA and WSF not only improves the mechanical and ductility performance of HSC but also can substantially decrease cost and carbon footprint due to a reduction in cement quantity.

3.1.2. Modulus of Elasticity (ECM).

E_{CM} is a measure of compression stiffness of concrete significantly within the elastic limit state of the material. The results of all HSC mixtures with different combinations of FA and WSF are shown in Figure 8. The relationship between WSF, FA, and relative E_{CM} of HSC is shown in Figure 9.

The addition of 10% FA showed a small improvement in E_{CM} of HSC. In contrast, the 28-day E_{CM} of HSC decreased considerably with the rising FA percentage. While, at 120 days, E_{CM} of HSC containing 10–15% FA was comparable with that of the reference HSC. Small percentages of FA can increase the compression stiffness by decreasing the pore size. The filling effect of small FA particles can cause a small increase in the density of concrete that improves the compressive stiffness, while pozzolanic activity also contributes to strength at lower levels of FA [7, 58]. In contrast, high-volume FA addition decreases the pozzolanic activity and inactive filler content of concrete increases. This slows the strength development and reduces E_{CM} [59].

Literature has shown insignificant effects of new steel fibers on E_{CM} [60] because fibers do not activate when the loading is well within the elastic limit of concrete. Therefore, E_{CM} of HSC entirely depends on the development level of basic ingredients of concrete. The addition of 1% WSF proved detrimental to E_{CM} as it caused a small reduction of 2–5% in E_{CM} because, at a high-volume fraction, the density of concrete might decrease due to the poor dispersion of fibers. 1% new steel fiber addition also showed a negative effect on E_{CM} [60]. Very few studies investigated the axial stress-strain characteristics of WSF-HSC mixes. A study showed a small increase (1–8%) in E_{CM} of ultra-high
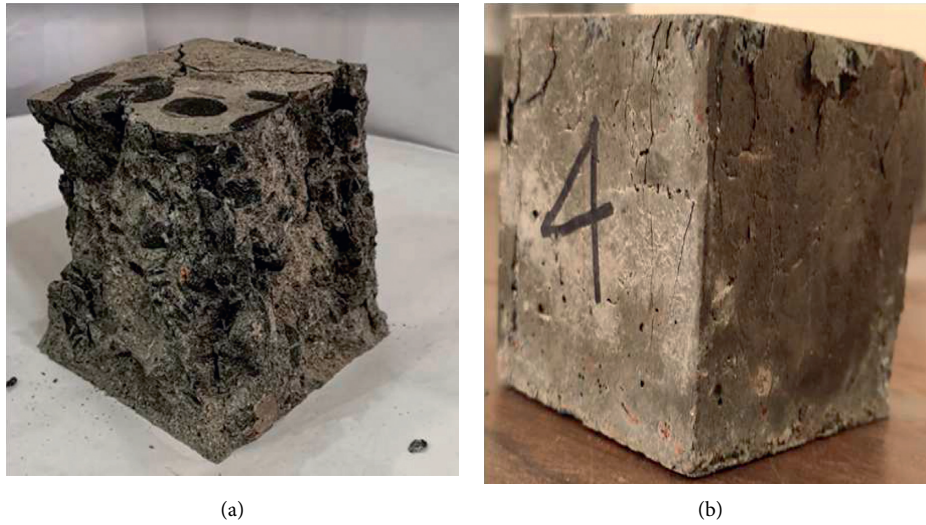
(a)

(b)

FIGURE 6: Compression failure. (a) Cube with 0% WSF. (b) Cube with 1% WSF.
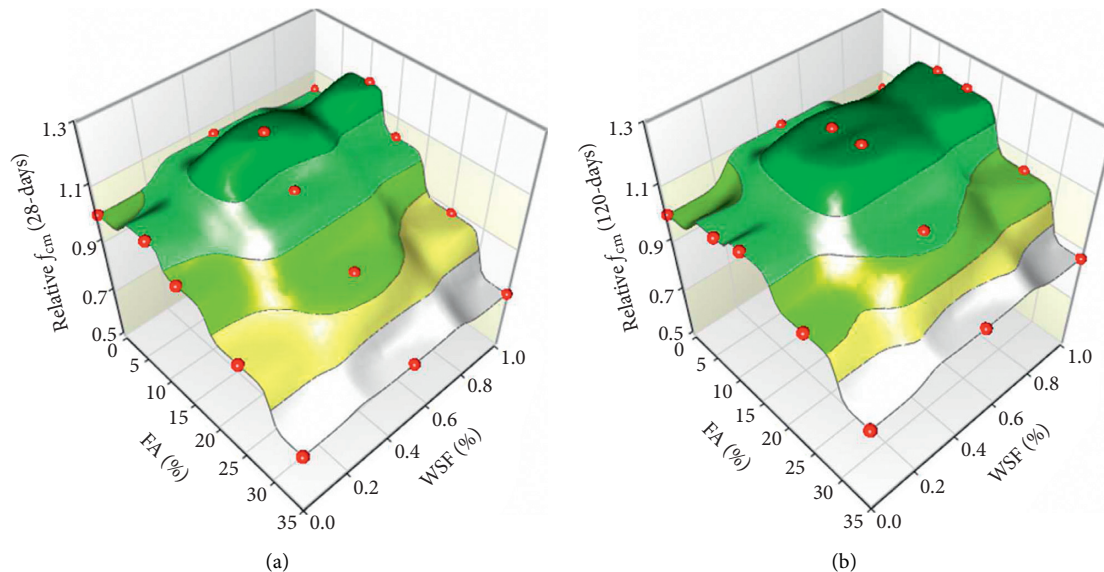

(a)

(b)

FIGURE 7: Relationship between FA, WSF, and relative f_{CM} values of HSC: (a) 28 days and (b) 120 days.

performance concrete due to 2–3% volume of WSF [61]. In contrast, a lot of efforts are still required towards understanding the effects of WSF on E_{CM} of concrete as the deficiency on this topic has been highlighted in a recent review study [62]. However, from this study, it can be concluded that 0.5% WSF proved to be useful to E_{CM}, while 1% WSF slightly lowered the E_{CM}.

The maximum E_{CM}, 4–5% higher than reference HSC, was shown by HSC containing 10% FA and 0.5% WSF at both 28 and 120 days. The negative effect of 1% WSF was more pronounced in HSCs containing a high volume of FA because increasing FA content in the binder decreased the matrix strength and eventually the bond performance of WSF. The low strength of the matrix weakened the grip over fibers; hence, it decreased the efficiency of WSF. In contrast, the negative effect of 1% WSF on E_{CM} was more pronounced

at 28 days in the HSC mix with a high volume of FA compared to the E_{CM} of these mixtures at 120 days. As the age of HSC increased, the negative effect of 1% WSF on E_{CM} reduced because the hardening of binder paste improves the bond performance of fibers [41].

3.2. Tensile Properties

3.2.1. Splitting-Tensile Strength (f_{CTM}). f_{CTM} was found out by conducting a split-tensile test on standard cylindrical samples of all mixes. The average f_{CTM} of each HSC mix with standard deviation value is shown in Figure 10. Brittleness is a major issue with the application of HSC because it has a small f_{CTM} value compared to the respective f_{CM}. Therefore, the fiber addition becomes a viable option to increase the ductility and fire resistance of HSC. As can be seen from the
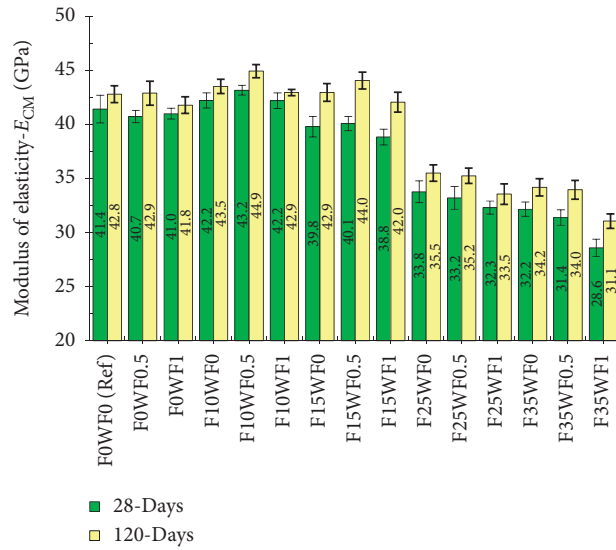
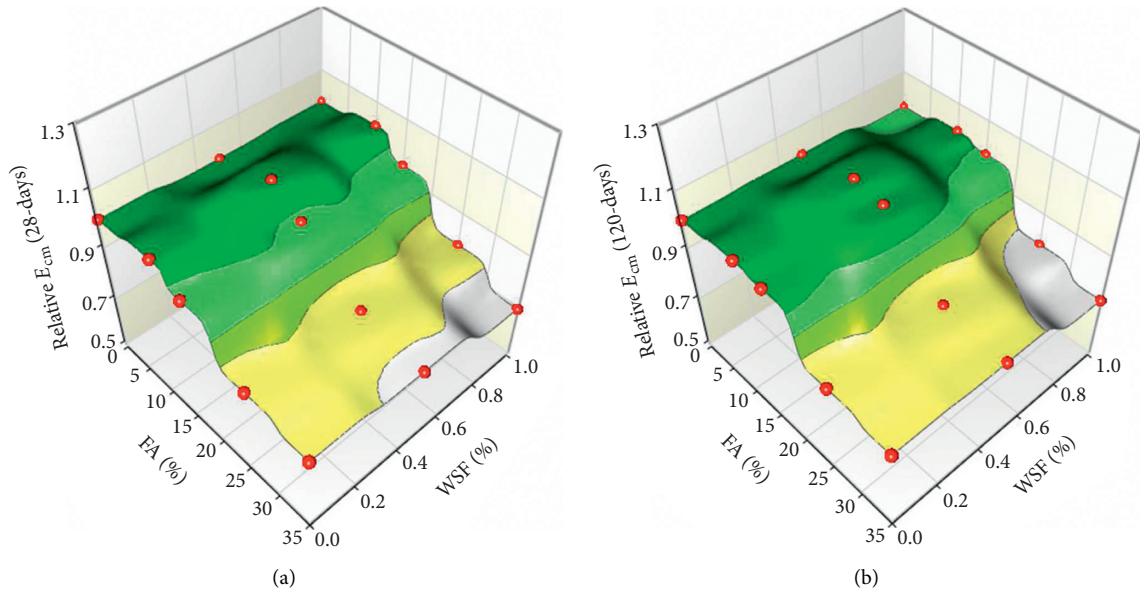FIGURE 8: Effect of different combinations of WSF and FA on the $(E)_{CM}$ of HSC.

(a)

(b)

FIGURE 9: Relationship between FA, WSF, and relative $(E)_{CM}$ values of HSC: (a) 28 days and (b) 120 days.
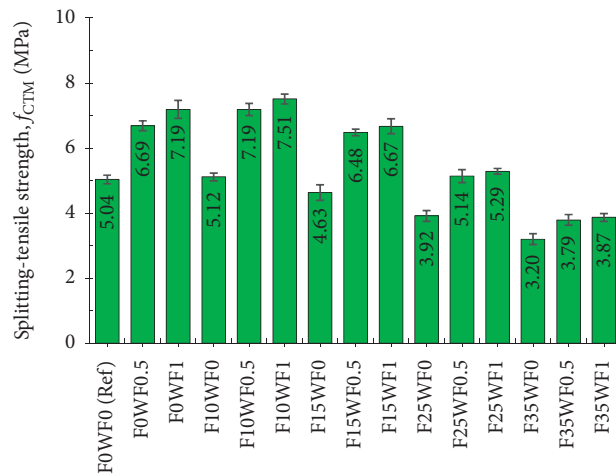

FIGURE 10: The f_{CTM} value of HSC with different incorporation levels of FA and WSF.

results, WSF proved very useful in advancing the tensile strength of HSC. An overall improvement of 32% and 42% was noticed in f_{CTM} of HSC (containing 0% FA) at 0.5% and 1% WSF addition. Studies have shown positive effects of WSF on f_{CTM} [63]. This improvement, as observed with industrial fibers, is credited to the crack-arresting behavior of WSF [27]. FA addition showed a negative effect on f_{CTM} of HSC. FA higher than 10% caused a drastic decline in tensile strength, whereas 10% replacement of cement with FA caused a small 2% increase in f_{CTM}. In contrast, 15, 25, and 35% FA addition reduce f_{CTM} of HSC by 8, 22, and 36%, respectively, because the decrease in strength development with the rising FA percentage in a binder and the filler effect of FA particles does not contribute to tensile strength.

The combined addition of 1% WSF and 10% FA showed an increase of 49% in f_{CTM} of HSC compared to the reference HSC mix. This showed using a smaller percentage of FA as cement replacement can synergize the benefits of using FA and WSF together. There was a certain improvement in the bond strength of WSF with the addition of 10% FA in the binder matrix. This has been observed with the combined use of FA (at a small level) and industrial steel [9] and glass fibers [58]. FA particles being spherical and smaller than cement particles can improve the particle packing in the binder matrix of HSC, in addition to the pozzolanicity potential of FA. These positive effects of a small percentage of FA reflect the improvement of the bond performance of fibers.

WSF has shown some positive effects on high-volume FA-HSC mixes. As we know, FA is ecofriendly and the cost and carbon footprint of concrete significantly drops when it replaces cement in the binder [7], but it badly affects the tensile performance of HSC. Therefore, WSF can help in controlling the drop of f_{CTM} due to the addition of a high volume of FA. The more important observation here is that HSC made with 25% FA and 1% WSF showed higher f_{CTM} than the reference HSC mix. The mix made with both FA and WSF was not just better in f_{CTM} than the reference mix, but it was also ecofriendly and cheap compared to the reference mix. WSF addition was not just useful in increasing the load at which HSC failed under splitting action. It was also very beneficial in containing the crack-width after the peak load, as shown in Figure 11. After the peak load, WSF-reinforced HSC possessed high residual strength than the plain HSC mix.

The net effect of WSF addition on f_{CTM} of HSC was reduced with the rising FA level in the binder. As FA decreased the strength of HSC, the grip of the binder over WSF weakens. Therefore, the net increase in f_{CTM} due to WSF addition was significantly influenced by the binder composition.

The ratio between f_{CTM} and f_{CM} of each HSC mix is shown in Figure 12. This ratio can be used to assess the ductility of a particular concrete mix. A higher value of the f_{CTM}/f_{CM} ratio indicates high ductility, while a lower value shows low ductility. It can be observed that the use of fibers increased the f_{CTM}/f_{CM} of HSC. The increase in f_{CTM}/f_{CM} of HSC was proportional to the reinforcement index. Figure 12 also showed that f_{CTM} of HSC increased from 6.7% to 9.3%

of f_{CM} as WSF content increased from 0 to 1%. f_{CTM}/f_{CM} of FA mixes went on decreasing with the rise in FA content. This showed that the brittleness of concrete increased when a high volume of FA was used. The relationship surface between FA and WSF contents and relative or normalized f_{CTM} is shown in Figure 13. According to this surface, maximum relative f_{CTM} of HSC was achieved within 0–15% FA and 0.5–1% WSF contents. On the contrary, the lowest relative f_{CTM} was shown by mixes incorporating 35% FA for a given content of WSF.

3.2.2. Modulus of Rupture (f_{CRM}).

f_{CRM} is another indirect measure of the tensile capacity of cement-based composites. The effect of different combinations of FA and WSF on f_{CRM} of HSC is shown in Figure 14. The variation in f_{CRM} results with the changing FA and WSF contents was similar to that observed in the case of f_{CTM} results. However, f_{CRM} was highly sensitive to WSF addition compared to f_{CTM}. Comparing the results of f_{CM}, E_{CM}, f_{CTM}, and f_{CRM} revealed that WSF addition yielded maximum benefits to f_{CRM}. Similar to WSF, other industrial fibers (steel, coconut, glass, polypropylene, etc.) [43, 56, 58, 64] have also shown maximum utilization in flexural behavior.

f_{CRM} of HSC increased by 56% and 78% due to the addition of 0.5% and 1% WSF, respectively. This showed a significant increment in the flexural toughness and ductility of HSC with WSF addition. On the contrary, a significant reduction in f_{CRM} was noticed at 15–35% FA addition. f_{CRM} of HSC dropped by 37% at 35% replacement of cement with FA. At high volume incorporation, FA is generally known to aggravate the mechanical properties of HSC similarly [5, 13, 65]. The common effect of FA addition was observed on the reduction level of all tested mechanical strength properties, that is, f_{CM}, E_{CM}, f_{CTM}, and f_{CRM}. It is because the change in microstructural growth is similarly reflected in compression and tensile properties.

The combination of 10% FA and 0.5–1% WSF showed superior results among all mixes. F10WF1 and F10WF0.5 showed 83% and 65% higher rupture strength than the reference mix. The synergistic effect of FA and WSF was noticed in F10WF1 and F10WF0.5. For example, the net increase in f_{CRM} due to 1% WSF addition in 0% FA-HSC was 70%, while 1% WSF showed an improvement of about 80% in 10% FA-HSC. The high net effect of WSF was achieved because of the synergistic behavior of 10% FA and 1% WSF. Improvement in the particle size distribution within HSC's matrix increases the pullout strength of WSF. However, the efficiency of WSF decreased significantly in HSC mixes containing a high volume of FA because the binder matrix containing high FA volume showed slow development and incomplete growth of microstructure at an early age.

It is generally known that FA incorporation shows some detrimental effects on the tensile properties of concrete. However, it is an ecofriendly and durable substitution of cement. The results of this study show that mixes with up to 25% FA can show better f_{CRM} than reference mix if 0.5–1% WSF is used as the reinforcement. Although choosing industrial fibers, to overcome the f_{CRM} strength loss of HSC
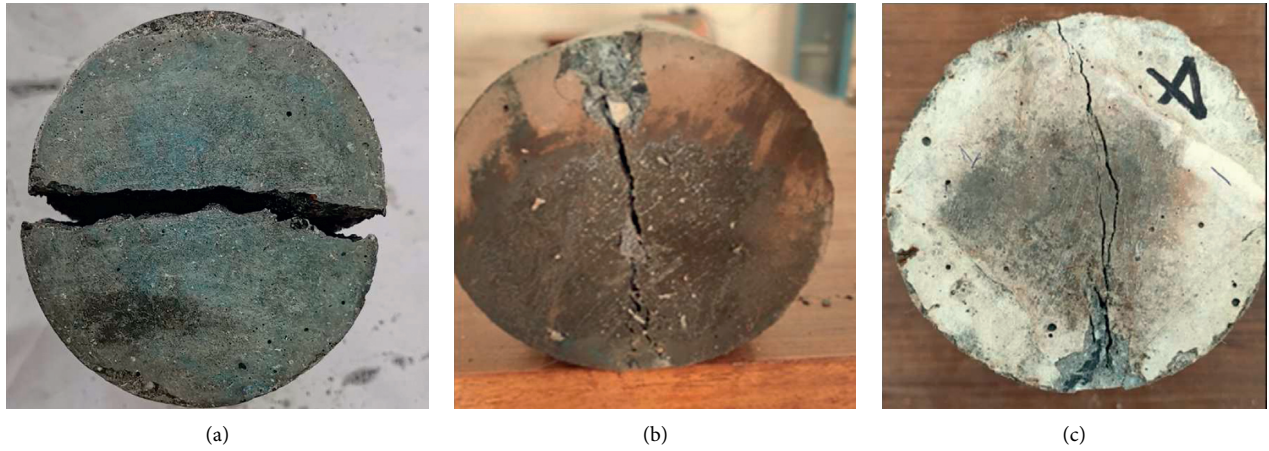
FIGURE 11: Splitting-tensile failure modes of HSC with (a) 0% WSF, (b) 0.5% WSF, and (c) 1% WSF.
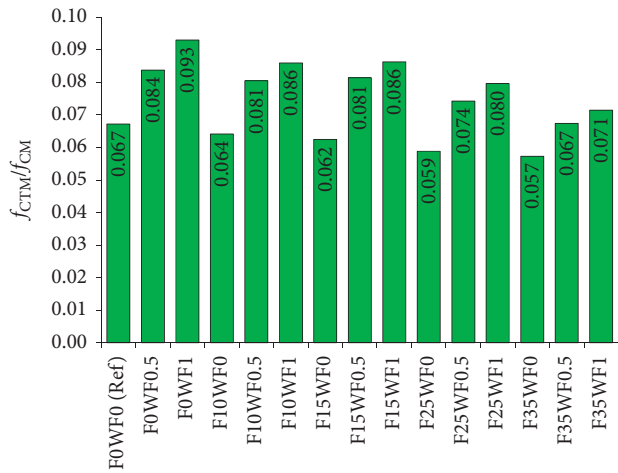

FIGURE 12: The ratio between f_{CTM} and f_{CM} of all HSC mixes.
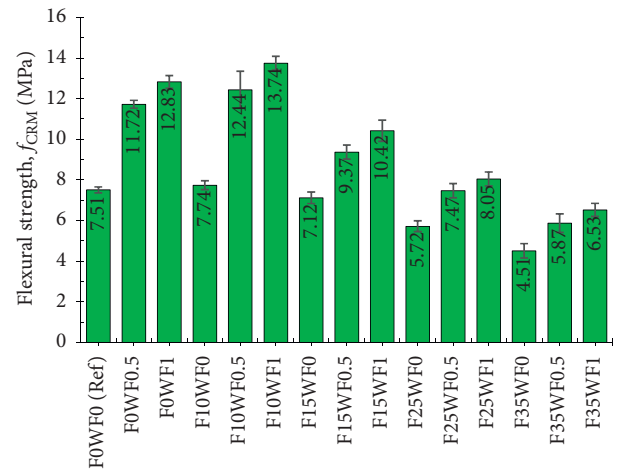

FIGURE 14: The f_{CRM} of each HSC mix with different incorporation levels of FA and WSF.
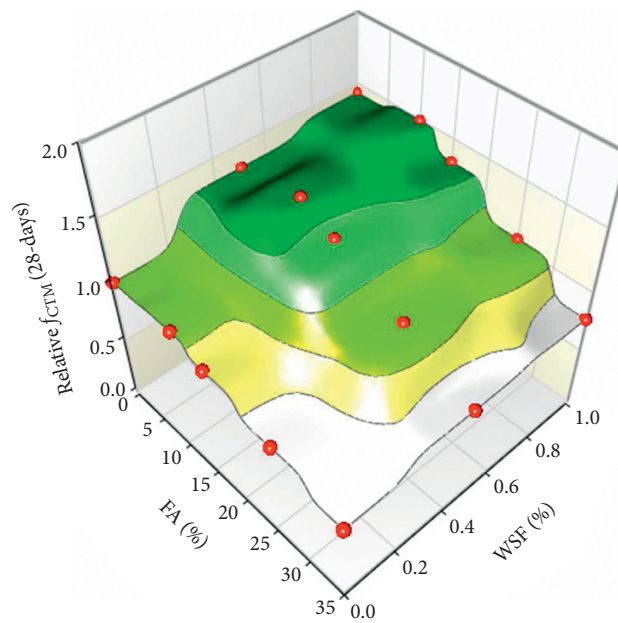

FIGURE 13: Relationship between WSF and FA contents and relative f_{CTM}.

due to FA, is an expensive and non-ecofriendly option, WSF, which is a waste product with minimum energy involved in its processing, can be used with FA to produce ductile and ecofriendly HSC. In addition to economic benefits, the HSC composite built with FA and WSF offers high flexural toughness and residual strength than reference HSC.

The f_{CRM}/f_{CM} ratio of each HSC mix is shown in Figure 15. It is noticed that plain HSC mixes made with or without FA showed f_{CRM}/f_{CM} ratio between 0.06 and 0.1. It means for HSC, f_{CRM} is about 6–10% of the corresponding f_{CM}. Fiber-reinforced HSC mixes yielded f_{CRM} about 16–18% of the f_{CM} value. High f_{CRM}/f_{CM} was shown by HSCs made with 0.5–1% WSF and 0–10% FA. The use of high-volume FA decreased the f_{CRM}/f_{CM} value significantly even for WSF-reinforced mixes. F35WF0, F35F0.5, and F35F1 showed f_{CRM}/f_{CM} values notably lower than the plain-reference mix (F0WF0). These findings suggested that the strength and development of the binder matrix substantially influence the efficiency of WSF. A 3-dimensional plot between relative f_{CRM}, WSF, and FA percentage is shown in Figure 16. The highest plateau (the maximum values of relative f_{CRM}) on this surface belongs to 0.5–1% WSF contents and 10% FA,
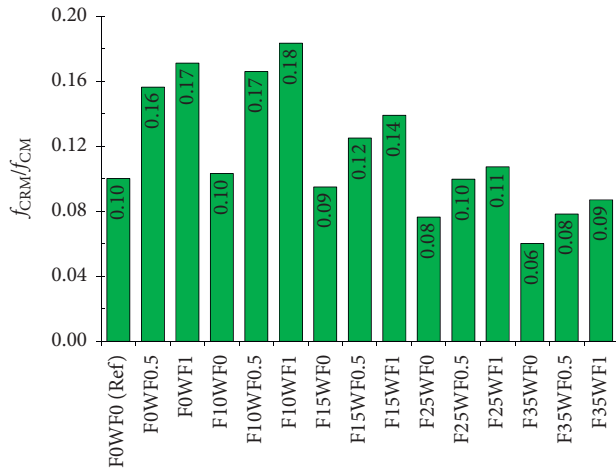
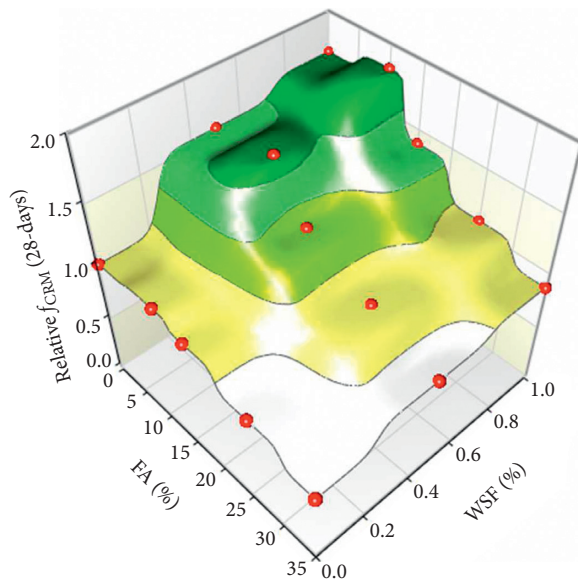FIGURE 15: The ratio between f_{CRM} and f_{CM} of all HSC mixes.

FIGURE 16: Relationship between WSF and FA contents and relative f_{CRM}.

while the lowest valley on the surface (the minimum values of relative f_{CRM}) is related to HSC mixes with 25–35% FA and 0–0.5% WSF contents.

3.3. Chloride Permeability Test Results

3.3.1. Rapid Chloride Permeability (RCP).
RCP test is used for rapid assessment of chloride-ion permeability resistance of cementitious concretes. The representative *RCP* value of a mix largely depends on the microstructural density and development. Moreover, it is also affected by the ability of concrete to conduct electrical charges. The effect of WSF and FA was determined on *RCP* resistance of HSC at 28 and 120 days. The results are presented in Figure 17.

The *RCP* values of all HSC mixes are lower than 2000 coulombs, which means *RCP* of all mixes comes under the category of "low" chloride-ion permeability, according to
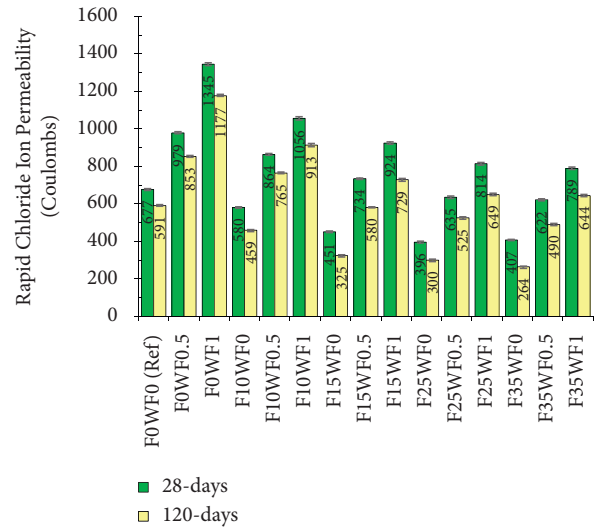

FIGURE 17: *RCP* of each HSC mix with different incorporation levels of FA and WSF.

Table 4. Moreover, plain mixes made with and without FA showed *RCP* values significantly lower than those noticed for WSF-reinforced mixes. *RCP* values of plain HSC mixes are lower than 1000, which indicates that plain mixes have "very low" chloride-ion permeability.

Very low *RCP* values of plain mixes are mainly because of a small water-binder ratio (i.e., 0.3). *RCP* of concrete further decreased with the rise in FA content; see Figure 18. The use of 10, 15, 25, and 35 FA decreased the *RCP* by 15%, 34%, 42%, and 40%, respectively. The decrease in *RCP* with FA inclusion in the binder is mainly credited to the filling effect of FA particles. Moreover, an increase in the tricalcium aluminate content of concrete increases the chloride binding capacity of concrete [10]. The inverse relationship between FA and *RCP* has also been observed in past research [67]. A decrease in the electrical conductivity of concrete has also been reported with the addition of slag in the binder of HSC [43].

The high electrical conductivity of WSF increased the *RCP* of HSC. About 50% and 100% increase of *RCP* was observed at the addition of 0.5 and 1% volume fraction of WSF in HSC. This immense increase in RCP indicates that WSF-HSC is more vulnerable to corrosion attacks. Not only are the main steel bars vulnerable to corrosion attack but also the filaments of WSF can degrade over time in HSC. Degradation of both WSF and main reinforcement will eventually lead to a decrease in the capacity of structural elements. The small increase in the permeability of HSC due to fiber addition may also contribute to an increase in *RCP* since permeability also favors the rapid penetration of chloride ions. A significant increase in the electrical conductivity of HSC has been observed due to the incorporation of industrial steel fiber [57]. The directly-proportional relationship between *RCP* and WSF contents is shown in Figure 19.

The use of FA significantly decreased the *RCP* of WSF-reinforced HSC. This means that FA can be used to compensate for the loss in chloride durability of HSC due to WSF

TABLE 4: Electrical indication of chloride durability [66].

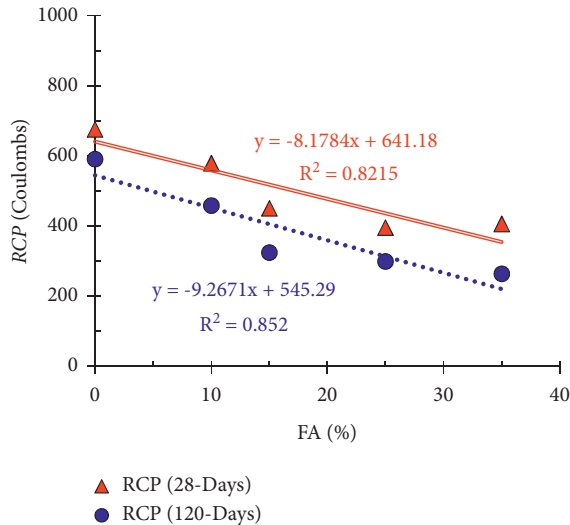| Electrical charge (coulombs)	Chloride penetrability of concrete
>4000	Very high
2000–4000	Normal
1000–2000	Low
100–1000	Very low
<100	Insignificant

FIGURE 18: Relationship between FA content in binder and corresponding *RCP* values of HSC.
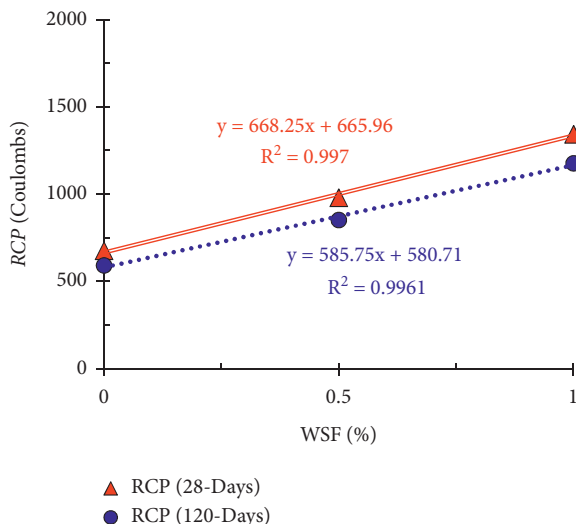

FIGURE 19: Relationship between WSF content and corresponding *RCP* values of HSC.

addition. To obtain *RCP* values of WSF-reinforced HSC in the range of the "very low" category, the use of 10–15% FA is necessary. The use of the high volume of FA showed high *RCP* resistance, but it reduced the strength, which would probably be the main drawback considering the application of high-volume FA in HSC. However, it is not possible to achieve an *RCP* value similar to the reference mix when

using 1% WSF without considering the use of the high volume of FA.

3.3.2. Chloride Penetration Depth (CPD). The *CPD* is a reliable and more realistic measurement of chloride penetrability of cementitious material than *RCP*, which is not affected by the electrical conductivity of the material. It largely depends on the porosity, saturation of pore-solution, and microstructural growth of concrete. The *CPD* of each HSC mix after immersion in chloride solution for 28 and 120 days is shown in Figure 20.

The incorporation of FA leads to a drop in *CPD*, indicating that chloride durability of concrete increases with FA addition. As already explained in Section 3.3.1, FA improves the distribution of particle sizes in the matrix of HSC. The decrease in pore size slows the movement of the chloride-bearing medium into the concrete. Moreover, alumina silicate particles of FA have chloride binding capacity. The minimum *CPD* was shown by HSC containing 25% FA. The relationship between FA (%) and *CPD* of HSC is shown in Figure 21. The *CPD* value of HSC kept decreasing until 25% FA, while a small increase in *CPD* was observed at 35% FA. This can be explained by a decline in the microstructural growth of the binder matrix at a high volume of FA addition. However, still, all FA mixes showed notably lower *CPD* values than the reference mix.

Contrary to *RCP* test results, *CPD* test results show a small effect of WSF on the chloride permeability of concrete; see Figure 22 because the high conductivity of WSF-reinforced concrete does not affect the penetration of chloride ions in natural conditions. *CPD* was increased only by 2–7% at 0.5–1% addition of WSF. The small increase in porosity due to WSF addition is responsible for a slight rise in the *CPD*. A study has shown that chloride diffusion of concrete is not significantly affected by the electrical conductivity of the material [68]. Therefore, steel fiber addition did not increase the chloride diffusion in the concrete. HSC mixes made with the combined FA and WSF addition show *CPD* values significantly lower than the reference mix. A small increase in *CPD* caused by WSF is substantially suppressed by FA addition.

3.3.3. Relationship between CPD and RCP. The relationship between *CPD* and *RCP* values of all HSC mixes is shown in Figure 23. Since *RCP* is significantly influenced by electrical conductivity, it does not find a strong correlation with *CPD*, as *CPD* is not affected by the conductivity of the material. For plain mixes (made with or without FA), it is possible to find a strong correlation between *CPD* and *RCP* values, but for WSF-reinforced mixes, it is difficult to correlate these two parameters without considering the effect of fiber.

Figure 24 shows the relationship between *CPD*, *RCP*, and WSF content of HSC at each level of FA. The relationship is derived in the format of equation (1), where *CPD* is calculated as a function of *RCP* and volume of WSF (V_{WSF}). A and B are constants of the linear equation. *RCP* is taken as an independent variable because it is determined quickly compared to *CPD*. Therefore, *CPD* can be estimated from
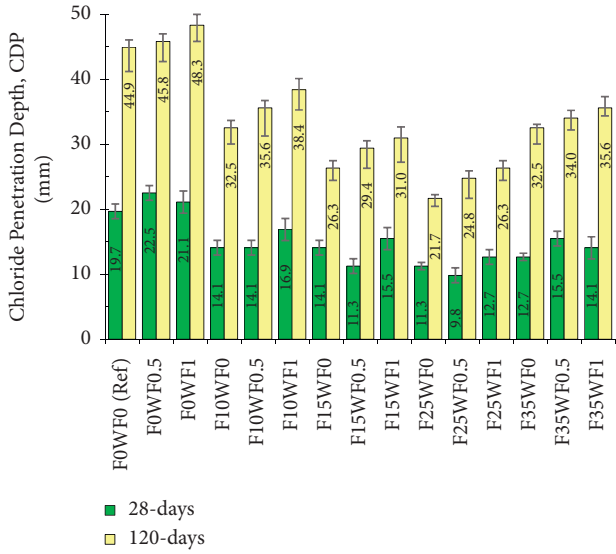
FIGURE 20: *CPD* of each HSC mix with different incorporation levels of FA and WSF.
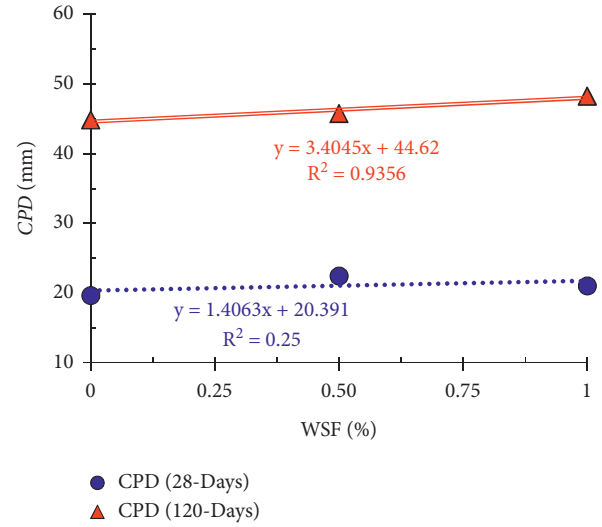

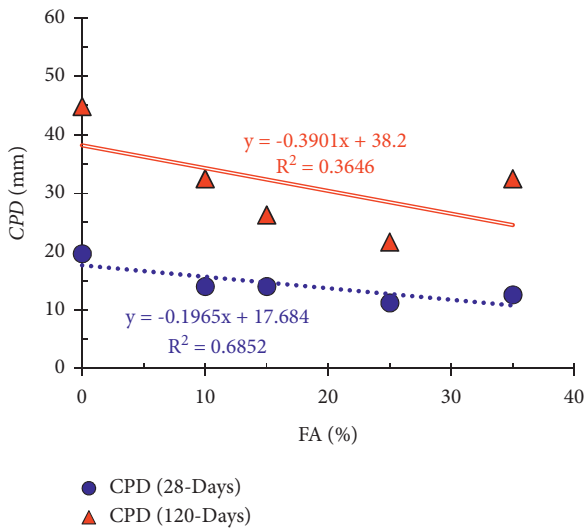FIGURE 22: Relationship between WSF content and corresponding *CPD* values of HSC.

FIGURE 21: Relationship between FA content in the binder and corresponding *CPD* values of HSC.
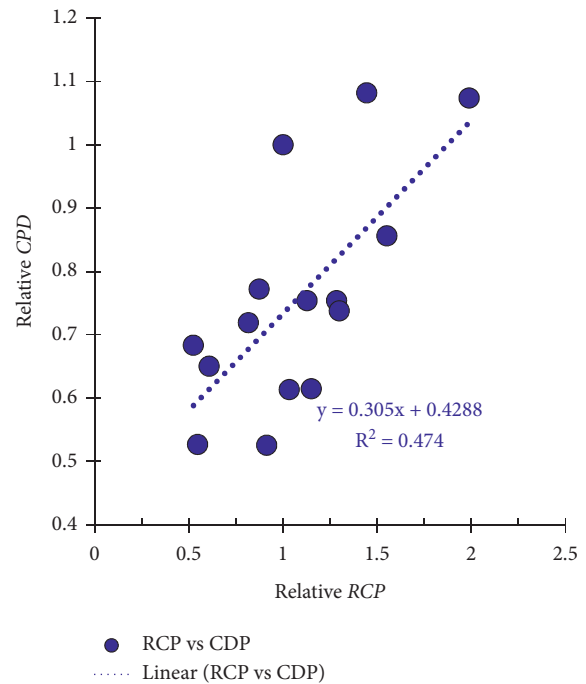

FIGURE 23: Relationship between *CPD* and *RCP*.

RCP for WSF-reinforced concretes. As shown in Figure 24, *CPD* and *RCP* can be correlated strongly if V_{WSF} is considered. These relationships have important implications for applications of steel fiber-reinforced concretes, as *CPD* values, which are found after a long time, can be accurately estimated from *RCP* as a function of V_{WSF}:

$$CPD = RCP \times (A \times V_{WSF} + B). \quad (1)$$

3.4. Sulfuric Acid Attack Resistance (AAR). Cementitious concretes often experience acidic environments in their application. In most cases, acidic solution dissolves both hydrated and unhydrated cementitious compounds, leading to the deterioration of the mechanical performance of

concrete. If calcareous aggregates are used, they are also dissolved by acidic action. Therefore, the measurement of *AAR* becomes a related durability parameter. In this study, the durability of HSC mixes was measured in an artificial acidic medium created by a 5% solution of sulfuric acid in tap water. The results of all HSC mixtures are shown in Figure 25.

The plain HSC or reference mix showed the maximum loss in mass compared to all other HSC mixtures at both ages of testing. The *AAR* of HSC substantially increased due to the addition of both FA and WSF. As FA content increased in
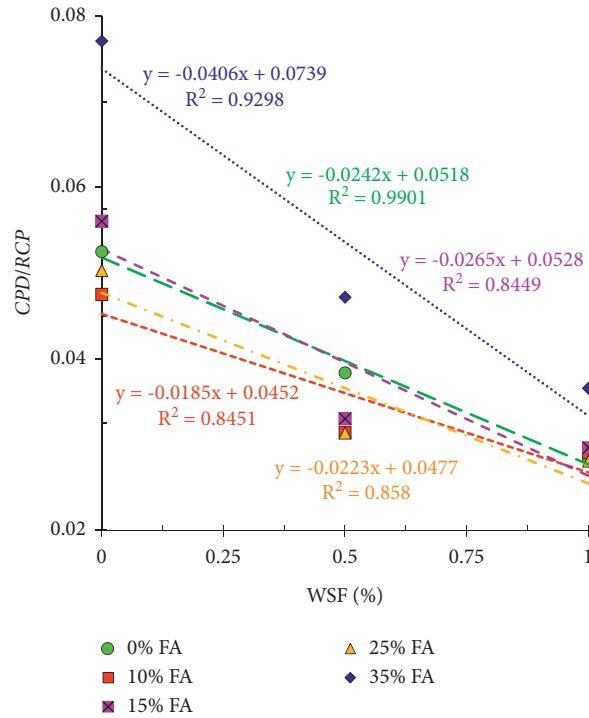
FIGURE 24: Relationship between CPD, RCP, and WSF content of WSF for each level of FA.
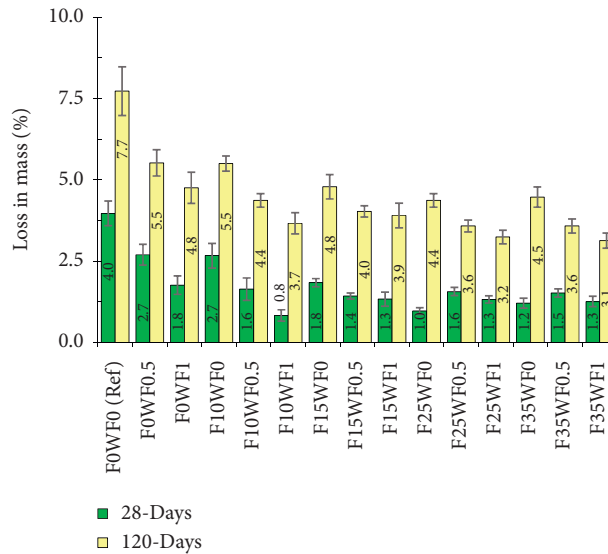

FIGURE 25: Loss in mass of each HSC mix with different incorporation levels of FA and WSF as a result of acid attack.

the concrete, the total alumina-silica content of the binder increased. The rise in FA causes a reduction in the calcium oxide content of the binder. The reduction in calcium hydrates and unhydrates makes the HSC resistant to acid attack. Similar observations were observed due to the addition of rice husk ash into the binder [68]. The increase in silica content and decline in lime content is the major reason responsible for the high durability of HSC in the acid attack. Another reason is that the low permeability of FA mixtures slows the movement of acidic solution into the matrix of the concrete.

The relationship between FA, WSF contents, and relative loss in mass (*LIM*) under acid attack are shown in Figure 26. This relationship shows that high *AAR* or low *LIM* under acid attack is achieved with high-level incorporation of WSF and FA. WSF increases *AAR* by its capability to hold crack propagation. Sulfate attack is accompanied by the formation of expansive salts and water. It exerts the pressure inside the binder matrix to disintegrate the microstructure of concrete and finally deteriorate the mechanical strength of HSC. WSF controls such disintegration and degradation of mechanical strength; as a result, low *LIM* was observed in mixes with fibers.
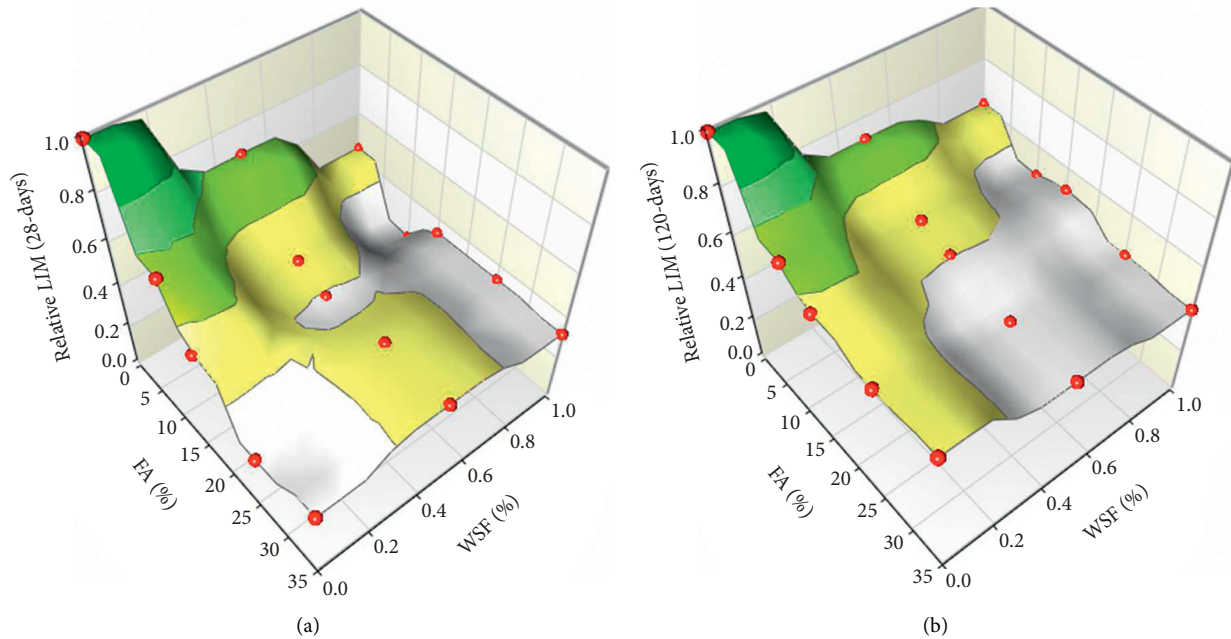
Figure 26: Relationship between FA, WSF, and relative loss in mass-*LIM* values of HSC: (a) 28 days and (b) 120 days.

Improvement in the AAR of concretes with industrial steel and glass fibers has been reported in previous studies due to their crack-bridging effects [9, 58, 69]. Mixes made with 10–35% FA and 0.5–1% WSF showed almost half disintegration under acid attack compared to the reference mixture. WSF also improved the residual strength of HSC exposed to an acidic solution.

4. Conclusions

In the present study, the combined effect of fly ash (FA) and waste tire steel fiber (WSF) was investigated on the durability and mechanical performance of high-strength concrete (HSC). The main theme of this research is the advancement in knowledge about ecofriendly and ductile cementitious composites. The following are the key findings of the present research:

(1) HSC made with low-to-medium levels of FA (10–15%) and WSF (0.5%) showed optimum f_{CM}. High-level incorporation of FA lessened the efficacy of WSF on f_{CM}. For all incorporation levels of FA, the optimum dosage of WSF is 1%. E_{CM} of HSC did not change considerably due to WSF. Lessening in E_{CM} was observed with the rising FA and WSF contents in HSC. HSC made with 0.5% WSF and 10% FA showed higher E_{CM} than the reference mix.

(2) f_{CTM} of HSC was considerably sensitive to WSF addition. The HSC made with 10% FA and 1% WSF showed maximum f_{CTM}, about 50% higher than the reference HSC mix. The splitting-tensile efficiency of WSF decreased with the rising FA percentage in the binder. Similar to f_{CTM}, f_{CRM} was also sensitive to WSF addition. Maximum f_{CRM} was shown by HSC incorporating 10% FA and 1% WSF, which was 83% higher than the reference mix.

(3) The *RCP* of HSC was increased drastically with WSF addition. 1% WSF addition caused about a 100% increase in the *RCP* of HSC mainly because of the high electrical conductivity. FA caused a decrease in *RCP* with each rising level. FA minimized the negative effect of WSF on *RCP*. However, *RCP* should not be taken as a good measure of chloride permeability capacity of steel fiber-reinforced concretes. On the contrary, *CPD* test results gave realistic values of chloride permeability capability of WSF-reinforced concretes.

(4) The *CPD* results are not affected by the electrical conductivity. Therefore, WSF addition did not show a drastic increase in *CPD*. All WSF-reinforced mixes incorporating FA showed lower *CPD* than the reference HSC mix. HSC made with 25% FA and 0.5% WSF showed 50% lower *CPD* than the reference mix. A strong mathematical correlation between *CPD* and *RCP* can be derived if the volume of WSF is considered.

(5) Both FA and WSF were extremely useful in *AAR*. Increased integrity of concrete due to the fibers and decline in calcium content of the binder is accountable for excellent acid attack durability of HSC incorporating FA and WSF.

Data Availability

Data will be provided upon request.

Conflicts of Interest

The authors declare that they have no conflicts of interest.

Acknowledgments

References

[1] D.-Y. Oh, T. Noguchi, R. Kitagaki, and W.-J. Park, "CO2 emission reduction by reuse of building material waste in the Japanese cement industry," *Renewable and Sustainable Energy Reviews*, vol. 38, pp. 796–810, 2014.

[2] E. Benhelal, G. Zahedi, E. Shamsaei, and A. Bahadori, "Global strategies and potentials to curb CO2 emissions in cement industry," *Journal of Cleaner Production*, vol. 51, pp. 142–161, 2013.

[3] N. Mahasenan, S. Smith, and K. Humphreys, "The cement industry and global climate changecurrent and potential future cement industry CO_2 emissions," in *Proceedings of the Greenhouse Gas Control Technologies-6th International Conference*, pp. 995–1000, Elsevier, Pergamon, Turkey, 2003.

[4] M. A. Nisbet, M. G. VanGeem, J. Gajda, and M. Marceau, "Environmental life cycle inventory of portland cement concrete," *PCA R&D Serial*, vol. 28, 2000.

[5] R. Kurda, J. de Brito, and J. Silvestre, "Combined economic and mechanical performance optimization of recycled aggregate concrete with high volume of fly ash," *Applied Sciences*, vol. 8, no. 7, p. 1189, 2018.

[6] M. A. Nawaz, L. A. Qureshi, B. Ali, and A. Raza, "Mechanical, durability and economic performance of concrete incorporating fly ash and recycled aggregates," *SN Applied Sciences*, vol. 2, no. 2, p. 162, 2020.

[7] R. Kurad, J. D. Silvestre, J. de Brito, and H. Ahmed, "Effect of incorporation of high volume of recycled concrete aggregates and fly ash on the strength and global warming potential of concrete," *Journal of Cleaner Production*, vol. 166, pp. 485–502, 2017.

[8] Astm-C618, *Standard Specification for Coal Fly Ash and Raw or Calcined Natural Pozzolan for Use in Concrete*ASTM International, West Conshohocken, PA, 2017, http://www.astm.org.

[9] B. Ali, S. S. Raza, R. Kurda, and R. Alyousef, "Synergistic effects of fly ash and hooked steel fibers on strength and durability properties of high strength recycled aggregate concrete," *Resources, Conservation and Recycling*, vol. 168, Article ID 105444, 2021.

[10] R. Kurda, J. D. Silvestre, J. de Brito, and H. Ahmed, "Optimizing recycled concrete containing high volume of fly ash in terms of the embodied energy and chloride ion resistance," *Journal of Cleaner Production*, vol. 194, pp. 735–750, 2018.

[11] R. Kurda, J. de Brito, and J. D. Silvestre, "Combined influence of recycled concrete aggregates and high contents of fly ash on concrete properties," *Construction and Building Materials*, vol. 157, pp. 554–572, 2017.

[12] A. R. Boğa and I. B. Topçu, "Influence of fly ash on corrosion resistance and chloride ion permeability of concrete," *Construction and Building Materials*, vol. 31, pp. 258–264, 2012.

[13] Y. Hefni, Y. A. E. Zaher, and M. A. Wahab, "Influence of activation of fly ash on the mechanical properties of concrete," *Construction and Building Materials*, vol. 172, pp. 728–734, 2018.

[14] B. B. Das and S. P. Pandey, "Influence of fineness of fly ash on the carbonation and electrical conductivity of concrete," *Journal of Materials in Civil Engineering*, vol. 23, no. 9, pp. 1365–1368, 2011.

[15] P. Chindaprasirt, C. Chotithanorm, H. T. Cao, and V. Sirivivatnanon, "Influence of fly ash fineness on the chloride penetration of concrete," *Construction and Building Materials*, vol. 21, no. 2, pp. 356–361, 2007.

[16] D. F. Velandia, C. J. Lynsdale, J. L. Provis, F. Ramirez, and A. C. Gomez, "Evaluation of activated high volume fly ash systems using Na 2 SO 4 , lime and quicklime in mortars with high loss on ignition fly ashes," *Construction and Building Materials*, vol. 128, pp. 248–255, 2016.

[17] S. H. Gebler and P. Klieger, "Effect of fly ash on physical properties of concrete," *Special Publication*, vol. 91, pp. 1–50, 1986.

[18] H. Rolander, *Potential Applications for High-Strength Concrete in Cast In-Situ Structures*, Aalto University, Espoo, Finland, 2019.

[19] M. F. M. Zain, H. B. Mahmud, A. Ilham, and M. Faizal, "Prediction of splitting tensile strength of high-performance concrete," *Cement and Concrete Research*, vol. 32, no. 8, pp. 1251–1258, 2002.

[20] E. Lubloy, "How does concrete strength affect the fire resistance?" *Journal of Structural Fire Engineering*, vol. 11, no. 3, 2020.

[21] V. Afroughsabet, L. Biolzi, and P. J. M. Monteiro, "The effect of steel and polypropylene fibers on the chloride diffusivity and drying shrinkage of high-strength concrete," *Composites Part B: Engineering*, vol. 139, pp. 84–96, 2018.

[22] S. Teng, V. Afroughsabet, and C. P. Ostertag, "Flexural behavior and durability properties of high performance hybrid-fiber-reinforced concrete," *Construction and Building Materials*, vol. 182, pp. 504–515, 2018.

[23] A. B. Kizilkanat, N. Kabay, V. Akyüncü, S. Chowdhury, and A. H. Akça, "Mechanical properties and fracture behavior of basalt and glass fiber reinforced concrete: an experimental study," *Construction and Building Materials*, vol. 100, pp. 218–224, 2015.

[24] A. Akbar and K. M. Liew, "Multicriteria performance evaluation of fiber-reinforced cement composites: an environmental perspective," *Composites Part B: Engineering*, vol. 218, Article ID 108937, 2021.

[25] A. Al-Tikrite and M. N. S. Hadi, "Mechanical properties of reactive powder concrete containing industrial and waste steel fibres at different ratios under compression," *Construction and Building Materials*, vol. 154, pp. 1024–1034, 2017.

[26] M. A. Aiello, F. Leuzzi, G. Centonze, and A. Maffezzoli, "Use of steel fibres recovered from waste tyres as reinforcement in concrete: pull-out behaviour, compressive and flexural strength," *Waste Management*, vol. 29, no. 6, pp. 1960–1970, 2009.

[27] M. Mastali and A. Dalvand, "Use of silica fume and recycled steel fibers in self-compacting concrete (SCC)," *Construction and Building Materials*, vol. 125, pp. 196–209, 2016.

[28] K. M. Liew and A. Akbar, "The recent progress of recycled steel fiber reinforced concrete," *Construction and Building Materials*, vol. 232, Article ID 117232, 2020.

[29] G. Centonze, M. Leone, and M. A. Aiello, "Steel fibers from waste tires as reinforcement in concrete: a mechanical characterization," *Construction and Building Materials*, vol. 36, pp. 46–57, 2012.

[30] C. C. Santos and J. P. C. Rodrigues, "Compressive strength at high temperatures of a concrete made with recycled tire textile and steel fibers," in *Proceedings of the MATEC Web of Conferences*, p. 7004, October 2013.

[31] M. Leone, G. Centonze, D. Colonna, F. Micelli, and M. A. Aiello, "Fiber-reinforced concrete with low content of recycled steel fiber: shear behaviour," *Construction and Building Materials*, vol. 161, pp. 141–155, 2018.

[32] K. Aghaee, M. A. Yazdi, and K. D. Tsavdaridis, "Investigation into the mechanical properties of structural lightweight concrete reinforced with waste steel wires," *Magazine of Concrete Research*, vol. 67, no. 4, pp. 197–205, 2015.

[33] O. Sengul, "Mechanical properties of slurry infiltrated fiber concrete produced with waste steel fibers," *Construction and Building Materials*, vol. 186, pp. 1082–1091, 2018.

[34] G. F. Peng, X. J. Niu, and Q. Q. Long, "Experimental study of strengthening and toughening for recycled steel fiber reinforced ultra-high performance concrete," *Key Engineering Materials, Trans Tech Publ*, vol. 629-630, pp. 104–111, 2015.

[35] A. H. Farhan, A. R. Dawson, and N. H. Thom, "Damage propagation rate and mechanical properties of recycled steel fiber-reinforced and cement-bound granular materials used in pavement structure," *Construction and Building Materials*, vol. 172, pp. 112–124, 2018.

[36] Y. Wang, H. C. Wu, and V. C. Li, "Concrete reinforcement with recycled fibers," *Journal of Materials in Civil Engineering*, vol. 12, no. 4, pp. 314–319, 2000.

[37] M. Ahmadi, S. Farzin, A. Hassani, and M. Motamedi, "Mechanical properties of the concrete containing recycled fibers and aggregates," *Construction and Building Materials*, vol. 144, pp. 392–398, 2017.

[38] M. Nili and V. Afroughsabet, "Combined effect of silica fume and steel fibers on the impact resistance and mechanical properties of concrete," *International Journal of Impact Engineering*, vol. 37, no. 8, pp. 879–886, 2010.

[39] J.-K. Kim, J.-S. Kim, G. J. Ha, and Y. Y. Kim, "Tensile and fiber dispersion performance of ECC (engineered cementitious composites) produced with ground granulated blast furnace slag," *Cement and Concrete Research*, vol. 37, no. 7, pp. 1096–1105, 2007.

[40] Y. Ling, K. Wang, W. Li, G. Shi, and P. Lu, "Effect of slag on the mechanical properties and bond strength of fly ash-based engineered geopolymer composites," *Composites Part B: Engineering*, vol. 164, pp. 747–757, 2019.

[41] Z. Wu, C. Shi, and K. H. Khayat, "Influence of silica fume content on microstructure development and bond to steel fiber in ultra-high strength cement-based materials (UHSC)," *Cement and Concrete Composites*, vol. 71, pp. 97–109, 2016.

[42] İ. B. Topçu and M. Canbaz, "Effect of different fibers on the mechanical properties of concrete containing fly ash," *Construction and Building Materials*, vol. 21, no. 7, pp. 1486–1491, 2007.

[43] V. Afroughsabet, L. Biolzi, and T. Ozbakkaloglu, "Influence of double hooked-end steel fibers and slag on mechanical and durability properties of high performance recycled aggregate concrete," *Composite Structures*, vol. 181, pp. 273–284, 2017.

[44] C. D. Atiş and O. Karahan, "Properties of steel fiber reinforced fly ash concrete," *Construction and Building Materials*, vol. 23, pp. 392–399, 2009.

[45] O. Karahan and C. D. Atiş, "The durability properties of polypropylene fiber reinforced fly ash concrete," *Materials & Design*, vol. 32, no. 2, pp. 1044–1049, 2011.

[46] S. S. Raza, L. A. Qureshi, and B. Ali, "Residual mechanical strength of glass fiber reinforced reactive powder concrete exposed to elevated temperatures," *SN Applied Sciences*, vol. 2, no. 9, 2020.

[47] E. Nazarimofrad, F. U. A. Shaikh, and M. Nili, "Effects of steel fibre and silica fume on impact behaviour of recycled aggregate concrete," *Journal of Sustainable Cement-Based Materials*, vol. 6, no. 1, pp. 54–68, 2017.

[48] M. Papachristoforou, E. K. Anastasiou, and I. Papayianni, "Durability of steel fiber reinforced concrete with coarse steel slag aggregates including performance at elevated temperatures," *Construction and Building Materials*, vol. 262, Article ID 120569, 2020.

[49] Astm-C150, *Standard Specification for Portland Cement*, ASTM International, West Conshohocken, PA, USA, 2018.

[50] Astm-C33, *Standard Specification for Concrete Aggregates*ASTM International, West Conshohocken, PA, USA, 2018.

[51] Astm-C39, *Standard Test Method for Compressive Strength of Cylindrical Concrete Specimens*, ASTM International, West Conshohocken, PA, USA, 2015, http://www.astm.org.

[52] Astm-C469, *Standard Test Method for Static Modulus of Elasticity and Poisson's Ratio of Concrete in Compression*, ASTM International, West Conshohocken, PA, USA, 2014, http://www.astm.org.

[53] Astm-C496, *Standard Test Method for Splitting Tensile Strength of Cylindrical Concrete Specimens*ASTM International, West Conshohocken, PA, 2017, http://www.astm.org.

[54] Astm-C1609, *Standard Test Method for Flexural Performance of Fiber-Reinforced Concrete (Using Beam with Third-Point Loading)*, ASTM International, West Conshohocken, PA, 2019, http://www.astm.org.

[55] Astm-C1202, *Standard Test Method for Electrical Indication of Concrete's Ability to Resist Chloride Ion Penetration*ASTM International, West Conshohocken, PA, 2017, http://www.astm.org.

[56] B. Ali, R. Kurda, B. Herki et al., "Effect of varying steel fiber content on strength and permeability characteristics of high strength concrete with micro silica," *Materials*, vol. 13, no. 24, p. 5739, 2020.

[57] V. Afroughsabet and T. Ozbakkaloglu, "Mechanical and durability properties of high-strength concrete containing steel and polypropylene fibers," *Construction and Building Materials*, vol. 94, pp. 73–82, 2015.

[58] B. Ali, L. A. Qureshi, S. H. A. Shah, S. U. Rehman, I. Hussain, and M. Iqbal, "A step towards durable, ductile and sustainable concrete: simultaneous incorporation of recycled aggregates, glass fiber and fly ash," *Construction and Building Materials*, vol. 251, Article ID 118980, 2020.

[59] A. F. Hashmi, M. Shariq, and A. Baqi, "An investigation into age-dependent strength, elastic modulus and deflection of low calcium fly ash concrete for sustainable construction," *Construction and Building Materials*, vol. 283, Article ID 122772, 2021.

[60] J. Xie, L. Huang, Y. Guo et al., "Experimental study on the compressive and flexural behaviour of recycled aggregate concrete modified with silica fume and fibres," *Construction and Building Materials*, vol. 178, pp. 612–623, 2018.

[61] M. N. Isa, K. Pilakoutas, M. Guadagnini, and H. Angelakopoulos, "Mechanical performance of affordable and eco-efficient ultra-high performance concrete (UHPC) containing recycled tyre steel fibres," *Construction and Building Materials*, vol. 255, Article ID 119272, 2020.

[62] H. U. Ahmed, R. H. Faraj, N. Hilal, A. A. Mohammed, and A. F. H. Sherwani, "Use of recycled fibers in concrete composites: a systematic comprehensive review," *Composites Part B: Engineering*, vol. 215, Article ID 108769, 2021.

[63] O. Onuaguluchi and N. Banthia, "Scrap tire steel fiber as a substitute for commercial steel fiber in cement mortar: engineering properties and cost-benefit analyses," *Resources, Conservation and Recycling*, vol. 134, pp. 248–256, 2018.

[64] M. Khan and M. Ali, "Improvement in concrete behavior with fly ash, silica-fume and coconut fibres," *Construction and Building Materials*, vol. 203, pp. 174–187, 2019.

[65] N. Bouzoubaâ, M. H. Zhang, and V. M. Malhotra, "Mechanical properties and durability of concrete made with high-volume fly ash blended cements using a coarse fly ash," *Cement and Concrete Research*, vol. 31, no. 10, pp. 1393–1402, 2001.

[66] D. B. McDonald, "The rapid chloride permeability test and its correlation to the 90-day chloride ponding test," *PCI Journal*, vol. 39, no. 1, pp. 38–47, 1994.

[67] O. A. Mohamed and W. Al Hawat, "Influence of fly ash and basalt fibers on strength and chloride penetration resistance of self-consolidating concrete," *Materials Science Forum*, vol. 866, pp. 3–8, 2016.

[68] M. Koushkbaghi, M. J. Kazemi, H. Mosavi, and E. Mohseni, "Acid resistance and durability properties of steel fiber-reinforced concrete incorporating rice husk ash and recycled aggregate," *Construction and Building Materials*, vol. 202, pp. 266–275, 2019.

[69] V. Marcos-Meson, G. Fischer, C. Edvardsen, T. L. Skovhus, and A. Michel, "Durability of steel fibre reinforced concrete (SFRC) exposed to acid attack - a literature review," *Construction and Building Materials*, vol. 200, pp. 490–501, 2019.